technische universität
dortmund

Dissertation

Exciton Polariton Interactions in Tailored Optical Potential Landscapes in Semiconductor Microcavities

submitted in partial fulfillment of the
requirements for the degree of

Dr. rer. nat.

to the Faculty of Physics at the
TU Dortmund University, Germany

by

Daniel Schmidt

Dortmund, February 2019

Accepted by the Faculty of Physics of the TU Dortmund University, Germany.

Day of the oral examination: 3rd May 2019

Examination board:
Jun.-Prof. Dr. Marc Aßmann
Prof. Dr. Mirko Cinchetti
Prof. Dr. Shaukat Khan
Dr. Bärbel Siegmann

Contents

1 Introduction **1**

I Physical Background **3**

2 Theory **5**
2.1 Excitons in Semiconductors 5
2.2 Quantum Well Excitons 8
2.3 Semiconductor Microcavities 9
2.4 Exciton Polaritons in Microcavities 13
2.5 Condensation of Microcavity Polaritons 19
2.5.1 The Ideal Bose Gas 20
2.5.2 Relaxation Dynamics 22

3 Experimental Methods **27**
3.1 Light Creation and Manipulation 28
3.2 Polariton Creation and Detection 33

II Results **39**

4 Optical Spin Hall Effect **41**
4.1 Origin of the Effective Magnetic Field 42
4.2 Experimental Details 47
4.2.1 Crosshatching 50
4.3 Pseudospin Dynamics and the Optical Spin Hall Effect 51
4.4 Conclusion 55

5 Perturbation of Polaritons in an Annular Optical Potential Trap **57**
5.1 Experimental Details 58
5.2 Results 60

5.3 Conclusion 67

6 Tracking Dark Excitons Optically Using Polariton Bistability 69
6.1 Optical Bistability of Microcavity Polaritons 70
6.1.1 Experimental Details 72
6.1.2 Generation of Optical Bistability 72
6.2 Tracking Dark Excitons with Bistable Polaritons 77
6.2.1 Experimental Details 77
6.2.2 Transition from Strong to Weak Coupling 78
6.3 Adding the Dark Reservoir 81
6.4 The Origin of the Dark Reservoir 83
6.5 Conclusion 87

7 Summary 89

A List of Abbrevations 91

Bibliography 93

Chapter 1

Introduction

In 2000, the Clay Mathematics Institute published a list of 7 problems which at the time were considered to be the most important problems in mathematics still to be solved. One of the more recent problems, called N=NP, was formulated by computer scientist and mathematician Stephen Cook in 1971 and first arose in the area of computer complexity theory [1]. This problem deals with the question whether a solution of a task or problem can be verified in polynomial time can it also be solved in polynomial time. Polynomial time refers to the polynomial increase of the computing time with the number of input parameters for a certain task, as opposed to an exponential increase of the computing time. For example, problems of combinatorial optimization, where the minimum of a function has to be found as a function of many parameters, belong to a subgroup of P and NP problems. Interestingly, there is a deep connection between such problems and problems in physics in which the behavior of a physical system with many degrees of freedom is investigated [2]. Among these systems are spin models, such as the Ising model, which have proved to be extremely useful in describing a wide range of phenomena in condensed matter [3]. Due to this connection it is possible to simulate complex problems with the help of physical systems in terms of an analogue Hamilton simulator [4]. This was demonstrated, for example, in spin glasses [5], with ultracold atoms in an optical lattice [6–10], with square lattices of superconducting q-bits [11], trapped ions [12, 13], or on networks of degenerate optical parametric oscillators [14, 15].

Recently it could be shown that exciton polariton condensates [16–19] in semiconductor microcavities are also suitable as analogue Hamilton simulators for classical systems [20–23]. Exciton polaritons arise due to the strong coupling between excitons and cavity photons within a microcavity, are easy to control by optical methods, and can be used for the construction of an analogue Hamilton simulator. The construction of the analogue Hamilton simulator

requires both the elements of the simulator and the interactions between the elements to be mapped to the Hamiltonian of the system to be simulated. However, in order to draw correct conclusions from the simulations using exciton polariton condensates, it is necessary to have detailed knowledge of the system. Some of the basic properties of exciton polaritons are investigated in the course of this thesis.

The thesis is divided into two parts. The first part offers a comprehensive introduction to the theoretical background of exciton polaritons. First the concept of bulk excitons is presented, then the properties of excitons in two-dimensional quantum well structures are discussed. To enhance light-matter interaction, the quantum wells may be placed inside an optical resonator, which is also discussed in detail. For a sufficiently large coupling strength, exciton polaritons may be formed whose properties are discussed in detail subsequently. The first part of this thesis concludes with a comprehensive analysis of the applied experimental methods.

In the second part of this thesis, the different experiments that have been carried out within the framework of this thesis are presented in order to investigate some basic properties of excitons polaritons. These include the dynamics of the spin polarization of propagating exciton polaritons presented in chapter 4, the condensation behavior of exciton polaritons for non-resonant excitation and the interaction of exciton polaritons with a reservoir of background carriers presented in chapter 5, as well as the lifetime of this reservoir presented in chapter 6. In the last chapter of the second part of this thesis, the major results of the experiments are finally summarized in a concise form.

Part I

Physical Background

Chapter 2

Theory

This chapter provides a theoretical introduction to the physical concepts that allow the description of quasiparticles in semiconductor structures. The quasiparticle of central interest in this thesis is the exciton polariton, which will be referred to as polariton for the sake of simplicity. Polaritons result from the strong coupling between excitons and photons in semiconductor structures. Accordingly, the discussion in this chapter begins with the introduction of the concept of excitons in semiconductors in general. After the initial introduction of excitonic properties in bulk material (based on [24]), the discussion will focus on their properties in lower-dimensional structures, which confine the excitons laterally. The lateral confinement strikingly changes the band-structure of the valence band, which modifies the selection rules for optical transitions. Subsequently, the concept of microcavities is presented in Sec. 2.3. Microcavities enable the strong coupling between quantum well excitons and cavity photons, which ultimately leads to the formation of polaritons. The specific properties of polaritons in microcavities are then discussed in Sec. 2.4. The last section of this chapter discusses one of the most intriguing properties of polaritons in microcavities, which, in analogy to Bose-Einstein condensation of atomic gases, is called polariton condensation. In particular, the relaxation mechanisms that lead to polariton condensation are discussed.

2.1 Excitons in Semiconductors

In solid-state physics, the permitted energy states of electrons in semiconductors are determined by band-structures. In a very simplified model, the band-structure consists of a valence band and a conduction band. An electron in the valence band can be transferred to the conduction band by absorbing a photon. During this process an electron hole is left behind in the valence

band creating an effective positive charge. Due to Coulomb interaction, the negatively charged electron in the conduction band and the positively charged hole in the valence band may form a new (quasi-)particle called exciton.

There are two kinds of excitons depending on their binding energy and therefore controlling their Bohr radius. In organic semiconductor crystals, usually the electrons and holes are strongly bound and located within the same unit cell. These so-called Frenkel excitons are therefore strongly localized and have a large binding energy. The other kind of excitons can be found in most non-organic semiconductors, which have a larger dielectric constant than organic semiconductors. Electrical field screening might lead to a reduction of the Coulomb interaction between the electron and the hole. As a result, only weakly bound electron-hole pairs are formed with a radius extending over a number of unit cells. These so-called Mott-Wannier excitons shall be considered for the remainder of this thesis.

In a semiconductor with a direct band gap and parabolic bands at the energy minimum in momentum space at $k = 0$, an electron in the conduction band and a hole in the valence band may form a hydrogen-like exciton state. The center-of-mass motion of the electrons and holes can be separated, resulting in a dispersion that depends quadratically on the center-of-mass momentum $\hbar\boldsymbol{K} = \hbar(\boldsymbol{k}_e + \boldsymbol{k}_h)$

$$E = \frac{\hbar^2 \boldsymbol{K}^2}{2M}, \tag{2.1}$$

with the total mass $M = m_e + m_h (m_e > 0,\, m_h < 0)$. The binding energies of the exciton series E_X^n for principal quantum numbers $n \geq 1$ are as follows

$$E_X^n = -\frac{m_r^*}{m_0}\frac{1}{\epsilon_r^2}\frac{m_0 e^4}{2(4\pi\epsilon_0\hbar)^2}\frac{1}{n^2}. \tag{2.2}$$

$(m_r^*)^{-1} = (m_e^*)^{-1} + (m_h^*)^{-1}$ denotes the reduced effective mass, m_0 is the electron mass, ϵ_0 the dielectric constant, and ϵ_r the dielectric constant of the considered material. The third term in Eq. (2.2) represents the atomic Rydberg energy (13.6 eV). In order to take into account the different masses and a different Coulomb screening of the excitons, the exciton series scales with $(m_r^*/m_0)\epsilon_r^{-2} \approx 10^{-3}$. This results in typical binding energies of about 4.1 meV for GaAs [25]. Taking into account the exciton series E_X^n, the band gap energy E_g and the dispersion (Eq. (2.1)), the total dispersion of bulk

excitons is thus given by

$$E_n(\boldsymbol{K}) = E_g - E_X^n + \frac{\hbar^2 \boldsymbol{K}^2}{2M}. \tag{2.3}$$

The exciton dispersion for different principal quantum numbers n is shown in Fig. 2.1. It should be noted that the oscillator strength of the excitons decreases with n^{-3}, which is why excitons for n>1 can, in most cases, be neglected safely.

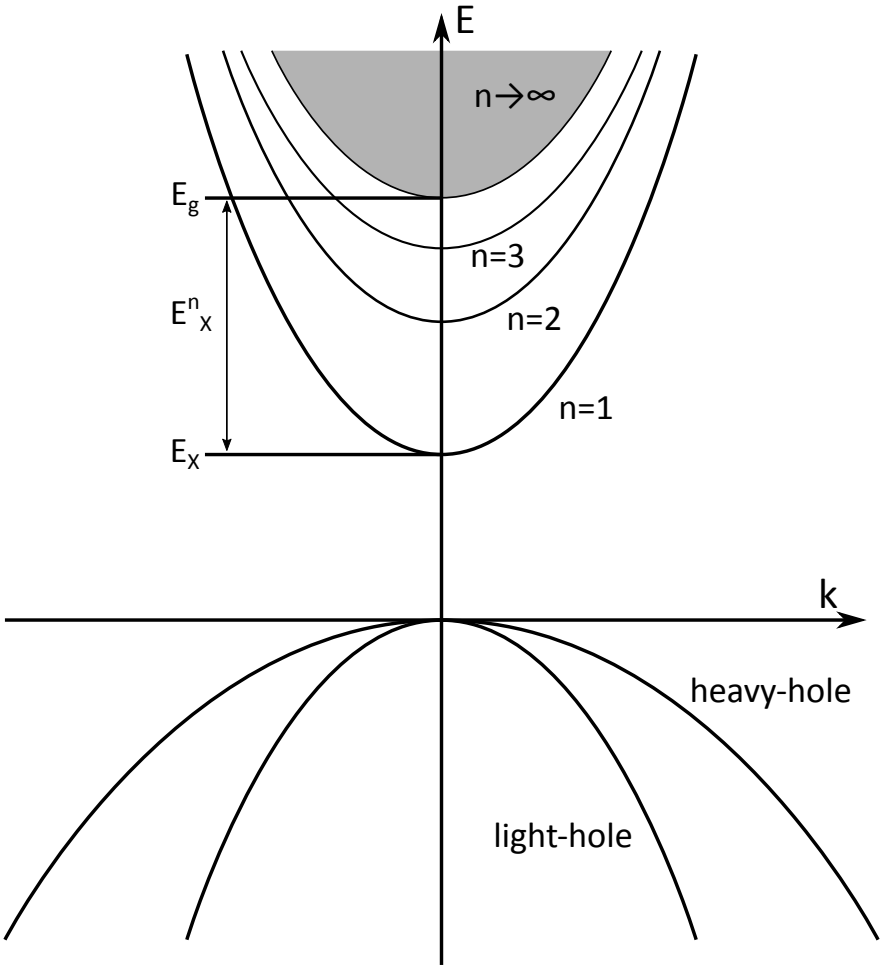

Figure 2.1: Schematic representation of the dispersion of bulk excitons for different principal quantum numbers n. The continuum of free electron and holes is indicated for principal quantum numbers $n \to \infty$. The split-off subband is omitted for simplicity. Adapted from Ref. [24].

The radius of the exciton r_X^n can be described in terms of the atomic Bohr radius of the hydrogen atom $a_B = 0.052\,\mathrm{nm}$ as:

$$r_X^n = n^2 \frac{m_e}{m_r^*} \epsilon_r a_B. \tag{2.4}$$

For the lowest energy state (n=1), the exciton radius for GaAs calculates to $r_1 = 14.5\,\mathrm{nm}$ [25]. Extending therefore over several atomic lattice constants ($a_{\mathrm{GaAs}} = 5.65\,\mathring{A}$ [26]), the description of excitons in terms of Mott-Wannier excitons is reasonably valid in GaAs. Furthermore, this radius lies in the same range as typical thicknesses of semiconductor quantum wells (QW), which will be introduced in the following section.

2.2 Quantum Well Excitons

In order to increase the binding energy of weakly bound Mott-Wannier excitons, the material system can be chosen accordingly. If the thickness of the semiconductor material is on the order of the exciton Bohr radius and sandwiched between two layers with a larger band gap energy, the properties of the excitons are changed drastically compared to excitons in bulk material. Because of the lateral confinement of the excitons, the Bohr radius is reduced, which leads to an increase of the binding energy and therefore an increase of the oscillator strength.

Also due to strain, induced by the lateral confinement, a modification of the band-structure arises. Especially for semiconductor materials with a zinc-blende crystal structure, such as GaAs, GaSb, GaN, GaP, AlAs, and so forth, the degeneracy at $k = 0$ between the light-hole and heavy-hole (see. Fig. 2.1) subbands is lifted [25]. Since the 1S-heavy-hole represents the energetically most favorable state for the formation of excitons, these will be considered throughout this thesis.

Because electrons and holes are fermions that have half-integer spins, the total angular Momentum J_z of the resulting exciton depends on the symmetry of both valence and conduction band, respectively. An electron in the conduction band with S-symmetry has a total angular momentum of $J_e = \pm 1/2$. The total angular momentum of the holes J_h in the valence band is composed by the spin S_h of the hole and its mechanical momentum M_h: $J_h = S_h + M_h = \pm 1/2, \pm 3/2$. Accordingly, optical transitions, referred to as bright transitions, can only

occur between states that have a total spin value of ± 1. All other transitions are considered as dark transitions. Consequently, these excitons are called dark excitons, because they can only decay non-radiatively. In Chapter 6 the discussion will focus on these kind of transitions.

A further consequence of the broken symmetry due to the lateral confinement is that the three-dimensional momentum of the excitons no longer represents a good quantum number. Accordingly, the conservation of momentum during optical excitation applies only along the in-plane directions of the quantum well. For this reason, the coupling of the excitons within the quantum wells only occurs to a light field with the same in plane wave vector $k_{\parallel}$ and an arbitrary wave vector $k_{\perp}$ perpendicular to the plane.

The coupling of excitons to a light field is necessary for the formation of polaritons. However, the reduced layer thickness of the quantum wells leads only to a small overlap with the light field. In order to reach strong coupling of excitons to the light field, the latter has to be amplified many times. One way to amplify the light field within quantum wells is to embed quantum wells within optical microcavities. Here, the quantum wells are placed in the anti-nodes of the confined cavity field, which greatly increases the coupling between excitons and the light field and therefore may give rise to the formation of polaritons. This kind of structure is introduced in the following section.

2.3 Semiconductor Microcavities

Planar semiconductor microcavities yield very interesting possibilities to investigate light and matter interactions, where both constituents are confined along the same direction. Moreover, they, by design, enhance the light field at a certain position inside the structure. This is caused by the reduction of the number of possible modes that can enter the microcavity, which therefore reduces the effective mode volume of the cavity. The discussion on microcavities is, unless further noticed, mainly based on Ref. [27].

In Figure 2.2, a microcavity that consists of a planar Fabry-Perot $n\lambda_c/2$ cavity, sandwiched in between two stacks of distributed Bragg reflectors (DBR) is shown. A DBR is a structure with alternating layer pairs of materials with nearly similar lattice constants but different refractive indices n_1 and n_2 ($n_1 < n_2$). The optical thickness of each layer is $\lambda/4$, which gives rise to a stop band for the transmission of light that is reflected at each interface, due to

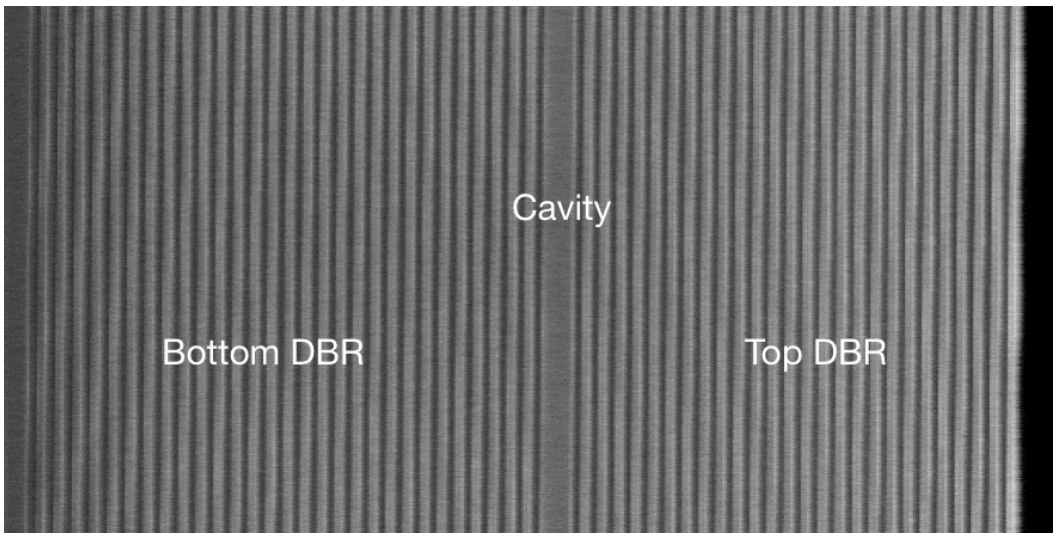

Figure 2.2: STM image of the sample C1575. The substrate can be seen on the left side, followed by the GaAs/AlAs bottom DBR layer pairs. The cavity is placed in between the bottom and top DBR. This is image is kindly provided by the University of Würzburg.

destructive interference. The DBR structure thus acts as a high reflective mirror with a reflectivity R close to unity for wavelengths within the stop band. The reflection R of a DBR is given by [28]:

$$R = 1 - 4\frac{n_{\text{ext}}}{n_c}\left(\frac{n_1}{n_2}\right)^{2N}, \tag{2.5}$$

with n_{ext} and n_c being the refractive indices of the exterior material - both substrate and air (vacuum), depending on the propagation direction of the light traveling through the sample - and of the cavity material, respectively. N represents the number of layer pairs.

If a layer with an optical thickness of integer multiples of $\lambda_c/2$ is placed between two layers of the highly reflective DBR structures, a sharp resonance is formed at λ_c. Due to the embedded cavity, the entire structure is called a 1D photonic crystal with a central defect (cavity), which is the reason for the sharp peak within the stop band at λ_c. In Fig. 2.3, a typical stop band of a microcavity is shown.

An important property of a microcavity is the quality factor (Q-factor). The Q-factor of a $\lambda/2$-cavity is a measure for the number of round trips a photon undergoes inside the cavity. It is also defined as the ratio between the cavity

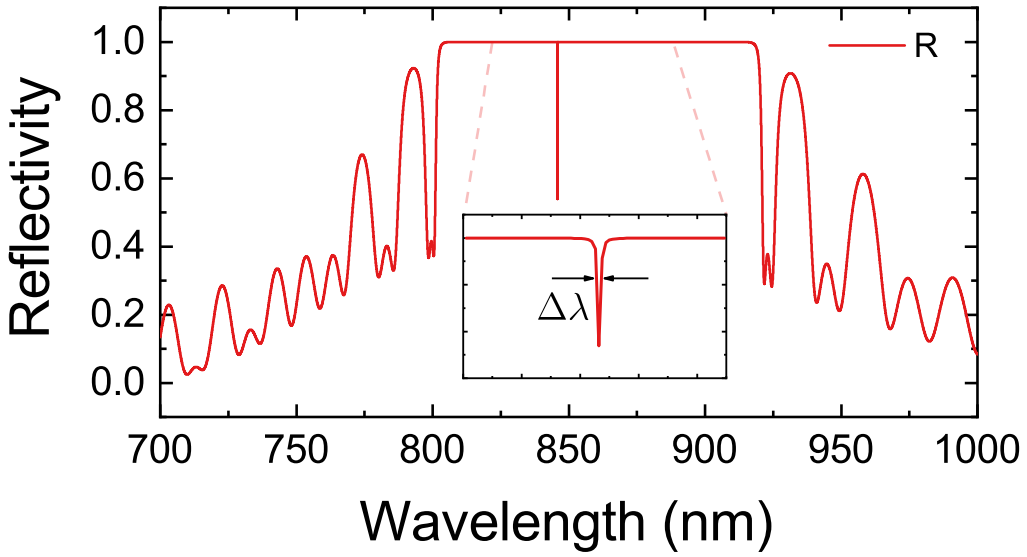

Figure 2.3: Reflectivity spectrum using the transfer matrix method simulation. The calculation is based on the layer thicknesses from the sample in Fig. 2.2, showing the stop band as well as the design wavelength λ_c. The inset displays a closeup of the design wavelength with the linewidth $\Delta\lambda_c$.

resonance wavelength λ_c and the full width at half maximum (FWHM) of its broadening $\Delta\lambda_c$:

$$Q = \frac{\lambda_c}{\Delta\lambda_c} \approx \frac{\pi(R_1 R_2)^{1/4}}{1-(R_1 R_2)^{1/2}}. \tag{2.6}$$

Here R_1 and R_2 represent the reflectivity of the individual DBR structure. The broadening $\Delta\lambda_c$ of the resonance frequency is caused due to the finite thickness of the DBR structure. Since the cavity layer in between both DBR layers is considered to be seen as an impurity or photonic defect of the structure, it allows light at a specific wavelength λ_c to enter or pass through the structure. The existence of this specific mode ultimately results in energy loss within the cavity itself, due to absorption, scattering or leaking through the imperfect mirrors. This energy loss leads to a finite lifetime of cavity photons within the structure of τ that is given by:

$$\tau = \frac{Q}{\omega_c}. \tag{2.7}$$

In contrast to metallic microcavities, where light in the visible region of the spectrum has almost no penetration depth and the Q-factors of metallic

microcavities only have values of less then Q < 500 [25], the situation changes drastically for DBRs. In DBRs the light field can penetrate much further into the structure. This is caused by the low reflection coefficient of the single DBR layers. The effective cavity length $L_{\text{eff}} = L_c + L_{\text{DBR}}$ is therefore enhanced by the effective penetration length

$$L_{\text{DBR}} = \frac{\lambda_c}{2n_c}\frac{n_1 n_2}{|n_1 - n_2|}. \tag{2.8}$$

The light field is confined along the growth axis of the cavity which is considered to be the z-axis, but can propagate freely along the planar directions (x- and y-directions). This implies a dependence of the in-plane wave number $k_\parallel$ on the angle of incidence Θ of the incoming light field:

$$k_\parallel \approx \frac{2\pi}{\lambda_c}\Theta, \tag{2.9}$$

for $\mathrm{k}_\parallel \ll \mathrm{k}_\perp = n_c(2\pi/\lambda_c)$. The resulting parabolic energy dispersion $E_{\text{cav}}(k_\parallel)$ of the cavity in the same region $k_\parallel \ll k_\perp$ has the following form:

$$E_{\text{cav}} \approx \frac{\hbar c}{n_c}k_\perp\left(1 + \frac{k_\parallel^2}{2k_\perp^2}\right) = E_{\text{cav}}(k_\parallel = 0) + \frac{\hbar^2 k_\parallel^2}{2m_{\text{cav}}}. \tag{2.10}$$

Here, m_{cav} denotes the effective mass of the cavity photon:

$$m_{\text{cav}} = \frac{E_{\text{cav}}(k_\parallel = 0)}{c^2/n_{\text{c}}^2}, \tag{2.11}$$

which is on the order of $10^{-5}m_e$, with m_e being the bare exciton mass. Due to different refractive indices for the transversal electric (TE) and the transversal magnetic (TM) polarization of the incident light, the effective mass of the cavity photons can differ depending on the polarization. This is expressed by a TE-TM splitting, which increases with the size of the wave vector and disappears for $k = 0$ [29]. In Chapter 4 of this thesis, the TE-TM splitting is described in more detail.

The maximum of the light field is strongly localized at the position of the cavity. Consequently, quantum wells are ideally placed at the position of the antinodes of the enhanced intracavity field, to enhance the light-matter interaction inside the microcavity. As will be described in the following section, this enhanced light-matter interaction gives rise to the new normal modes of this system, namely polaritons.

2.4 Exciton Polaritons in Microcavities

The properties of elementary excitations in solids such as excitons, are determined by the properties of their environment. Excitons are created by the coupling of electron and hole to each other and thus represent a polarization of the solid. Photons moving through a solid may often be treated as decoupled from the elementary excitations of the solid. This decoupling becomes invalid, if the energy of the photon corresponds to the energy of the elementary excitations. In this case, the photons resonant with the transition or excitation are absorbed by the solid. If one assumes that the electromagnetic field within the solid can be treated as a dielectric background, then the absorption of a photon represents a polarization of the dielectric field, whereby the polarization can again be regarded as the source of the photon [30].

The cycle of photon absorption (exciton generation) and photon emission (exciton recombination) can be represented as a coupled oscillation between excitons and an electromagnetic field. In addition, if this cycle takes place within a material in which photons have a relatively long effective lifetime (see Eq. (2.7)), strong coupling between the excitons and photons might occurs. This strong coupling gives rise to the formation of polaritons. In the following, we initially consider polaritons as coupled excitons and photons without decay processes taking place.

This coupled system is described by a linear Hamilton operator in second quantization and reads, under consideration of the rotating wave approximation, which neglects antiresonant contributions $\hat{a}^\dagger_{k_\parallel}\hat{b}^\dagger_{k_\parallel}$ $(\hat{a}_{k_\parallel}\hat{b}_{k_\parallel})$ of simultaneous creation (annihilation) of an exciton and a photon:

$$\begin{aligned}\hat{H}_{\mathrm{pol}} &= \hat{H}_{\mathrm{exc}} + \hat{H}_{\mathrm{cav}} + \hat{H}_{\mathrm{I}} \\ &= \sum E_{\mathrm{cav}}(k_\parallel, k_c)\hat{a}^\dagger_{k_\parallel}\hat{a}_{k_\parallel} + \sum E_{\mathrm{exc}}(k_\parallel)\hat{b}^\dagger_{k_\parallel}\hat{b}_{k_\parallel} \\ &\quad + \sum \hbar\Omega(k_\parallel)(\hat{a}^\dagger_{k_\parallel}\hat{b}_{k_\parallel} + \hat{a}_{k_\parallel}\hat{b}^\dagger_{k_\parallel}).\end{aligned} \tag{2.12}$$

Here $\hat{a}^\dagger_{k_\parallel}(\hat{a}_{k_\parallel})$ and $\hat{b}^\dagger_{k_\parallel}(\hat{b}_{k_\parallel})$ are the bosonic generation (annihilation) operators for photons and excitons with the wave vector $k_\parallel$ within the plane, respectively. The energy of the photons E_{cav} has an additional dependence, which is given by the longitudinal wave vector $k_c = \boldsymbol{k}\hat{z}$. The coupling strength $g_0 = \hbar\Omega$ between excitons and photons is represented by the Rabi energy, where Ω represents the Rabi frequency [31]. This frequency represents the exchange

rate between the generation of an exciton and the emission of a photon. It is only nonzero for excitons and photons that have the same wave vector $k_\parallel$.

The matrix representation of the Hamilton operator in the exciton and photon base illustrates the coupling between the eigenmodes

$$\hat{H}_{\mathrm{pol}} = \begin{pmatrix} E_{\mathrm{cav}}(k_\parallel) & \frac{\hbar\Omega}{2} \\ \frac{\hbar\Omega}{2} & E_{\mathrm{exc}}(k_\parallel) \end{pmatrix}. \tag{2.13}$$

By changing to the base of the new polariton eigenmodes, i.e. upper (UP) and lower (LP) polariton states, it is possible to diagonalize this matrix. The base change is performed by a transformation known as Hopfield-Bogoliubov transformation [32]

$$\hat{P}_{k_\parallel} = X_{k_\parallel}\hat{b}_{k_\parallel} + C_{k_\parallel}\hat{a}_{k_\parallel}, \tag{2.14}$$

$$\hat{Q}_{k_\parallel} = -C_{k_\parallel}\hat{b}_{k_\parallel} + X_{k_\parallel}\hat{a}_{k_\parallel}. \tag{2.15}$$

Within this basis, the resulting Hamilton operator is given by

$$\hat{H}_{\mathrm{pol}} = \sum E_{\mathrm{LP}}(k_\parallel)\hat{P}^\dagger_{k_\parallel}\hat{P}_{k_\parallel} + \sum E_{\mathrm{UP}}(k_\parallel)\hat{Q}^\dagger_{k_\parallel}\hat{Q}_{k_\parallel}. \tag{2.16}$$

The operators $\hat{P}_{k_\parallel}$ ($\hat{P}^\dagger_{k_\parallel}$) and $\hat{Q}_{k_\parallel}$ ($\hat{Q}^\dagger_{k_\parallel}$) are the annihilation (creation) operators of the new quasiparticle eigenmodes of the LP ($\hat{P}$) and the UP ($\hat{Q}$), respectively. The designation of lower and upper polaritons is based on their separation into states with different energy. Polaritons can be understood as a linear superposition between excitons and photons and since both are bosonic in nature, polaritons are also considered as bosons. The factors X and C are known as the Hopfield coefficients for which the following relationship applies

$$|X_{k_\parallel}|^2 + |C_{k_\parallel}|^2 = 1. \tag{2.17}$$

The square of the mean value of the Hopfield coefficients $|X_{k_\parallel}|^2$ and $|C_{k_\parallel}|^2$ determines the excitonic and photonic fraction within the upper and lower polariton branch (LPB). When taking the energy detuning $\Delta E(k_\parallel) = E_{\mathrm{exc}}(k_\parallel) - E_{\mathrm{cav}}(k_\parallel, k_c)$ between the bare exciton and cavity mode into account, the square

of the mean values of the Hopfield coefficients can be expressed as

$$|X_{k_\parallel}|^2 = \frac{1}{2}\left(1 + \frac{\Delta E(k_\parallel)}{\sqrt{\Delta E(k_\parallel)^2 + 4g_0^2}}\right), \tag{2.18}$$

$$|C_{k_\parallel}|^2 = \frac{1}{2}\left(1 - \frac{\Delta E(k_\parallel)}{\sqrt{\Delta E(k_\parallel)^2 + 4g_0^2}}\right). \tag{2.19}$$

From these equations follow that for $\Delta E(k_\parallel) = 0$ between the excitonic and the photonic mode, both coefficients are equal and the polaritons consist of equal parts of photons and excitons, i.e. $|X|^2 = |C|^2 = 0.5$.

The diagonalization of the Hamilton operator $\hat{H}_{\mathrm{pol}}$ in the base of the polaritons (2.16) yields the eigenenergies of the lower and upper polaritons

$$E_{\mathrm{LP,UP}}(k_\parallel) = \frac{1}{2}\left(E_{\mathrm{exc}} + E_{\mathrm{cav}} \pm \sqrt{4g_0^2 + (E_{\mathrm{exc}} - E_{\mathrm{cav}})^2}\right). \tag{2.20}$$

This equation provides an explanation for the energy separation. By introducing the detuning δ

$$\delta \equiv E_{\mathrm{cav}}(k_\parallel = 0) - E_{\mathrm{exc}}(k_\parallel = 0) \tag{2.21}$$

between the exciton and photon mode at $k_\parallel = 0$, it is possible to illustrate how the two modes develop for different detunings. This illustration is shown in Fig. 2.4

At a detuning of $\delta = 0$ at $k_\parallel = 0$, the energies of the bare excitonic and photonic resonances are equal. A look at the development of the energies of the two polariton branches for different detunings reveals an anti-crossing behavior at $\delta = 0$. The repulsion of the two modes is a clear signature for strong coupling between these modes. The strength of this coupling is determined by the minimum energy distance $2g_0$ and is called normal mode splitting in analogy to the Rabi splitting of single atom cavities.

The analysis of the Hopfield coefficients of the lower polariton also shows how the composition of the fraction of excitons and photons changes for various detunings. For negative detunings, the lower polariton becomes very photonic, which is expressed by an asymptotic approach towards the cavity resonance. Conversely, the lower polariton becomes more and more excitonic for positive

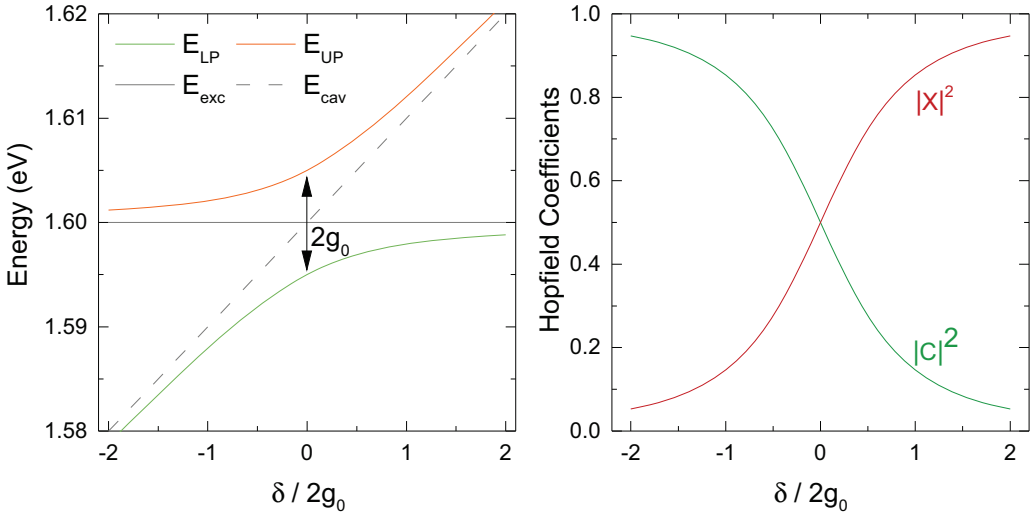

Figure 2.4: Left: Development of the energies of the lower and upper polaritons as a function of the detuning at $k_{\parallel} = 0$. A typical feature of the strong coupling between two states is the anti-crossing of the states for a detuning of $\delta = 0$. The strength of the coupling is given by the factor $2g_0$. Right: Development of the Hopfield coefficients of the lower polariton branch for different detunings δ at $k_{\parallel} = 0$.

detunings. Accordingly, the Hopfield coefficients $|X|^2$ and $|C|^2$ also develop as a function of the detuning.

The consideration of the dependence of the polariton energies on the wave vector reveals the dispersion of the polaritons. A dependence of the energy of the exciton on the wave vector is excluded for the size of the considered wave vectors. The energy of the exciton is therefore assumed to be constant. The dependence of the cavity energy on the wave vector is achieved by inserting Eq. (2.10) into the energies of the upper and lower polaritons in Eq. (2.20). The dispersion of the polaritons and the corresponding Hopfield coefficients are shown in Fig. 2.5 for various detunings. For large wave vectors, the upper (lower) polariton branch approaches the photonic (excitonic) mode and thus becomes indistinguishable from these modes, regardless of the detuning. As an example, this is shown for the lower polariton mode in the lower part of Fig. 2.5, where the Hopfield coefficients for the photonic and excitonic fraction of the lower polariton are shown as a function of the wave vector. For large wave vectors, the value for $|X|^2$ approaches unity, which well illustrates the indistinguishability of the lower polariton from the exciton. However, the situation differs drastically for small wave vectors around $k_{\parallel} = 0$, where

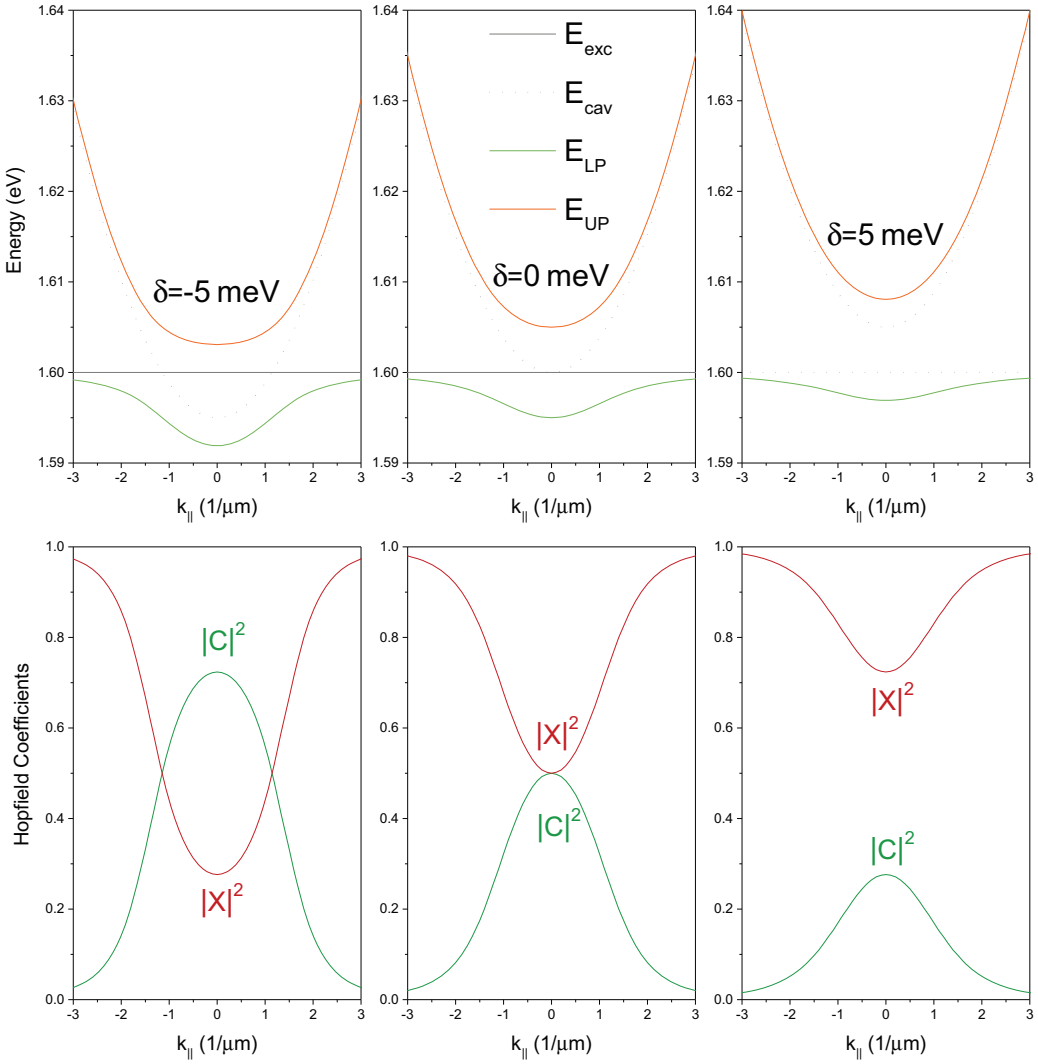

Figure 2.5: Upper set: Exemplary representation of the polariton dispersion for different detunings to illustrate the dependence of the polariton energies on the wave vector. Lower set: Representation of the Hopfield coefficients of lower polaritons for selected detunings as a function of the wave vector.

significant differences of the polariton modes occur compared to the uncoupled modes of the cavity and the exciton.

For a negative detuning, the lower polariton is characterized by a clearly visible curvature of the dispersion around $k_{\parallel} = 0$. In the region $\hbar^2 k_{\parallel}^2/(2m_{\mathrm{cav}}) \ll 2g_0$,

the dispersion of the lower polariton can be considered approximately as parabolic. Accordingly, Eq. (2.20) becomes

$$E_{\mathrm{LP,UP}}(k_\parallel) \approx E_{\mathrm{LP,UP}}(0) + \frac{\hbar^2 k_\parallel^2}{2m_{\mathrm{LP,UP}}}. \tag{2.22}$$

The effective masses of the upper and lower polaritons can be expressed by using the Hopfield coefficients as well as the effective masses of the exciton m_{exc} and cavity-photon m_{cav}

$$\frac{1}{m_{\mathrm{LP}}} = \frac{|X|^2}{m_{\mathrm{exc}}} + \frac{|C|^2}{m_{\mathrm{cav}}}, \tag{2.23}$$

$$\frac{1}{m_{\mathrm{cav}}} = \frac{|C|^2}{m_{\mathrm{exc}}} + \frac{|X|^2}{m_{\mathrm{cav}}}. \tag{2.24}$$

As already mentioned in the previous section, the cavity photons have a much smaller effective mass than the excitons ($m_{\mathrm{cav}} \sim 10^{-5} m_{\mathrm{exc}}$). For a small region around $k_\parallel = 0$, the effective masses for both species of polaritons can thus be estimated by

$$m_{\mathrm{LP}}(k_\parallel \approx 0) \simeq m_{\mathrm{cav}}/|C|^2 \sim 10^{-4} m_{\mathrm{exc}}, \tag{2.25}$$

$$m_{\mathrm{UP}}(k_\parallel \approx 0) \simeq m_{\mathrm{cav}}/|X|^2. \tag{2.26}$$

As a result, lower polaritons with a large photonic fraction $|C|^2$ have a very small effective mass close to $k_\parallel = 0$, which, however, for increasingly larger wave vectors approach the effective mass of the bare exciton. Consequently, the effective mass of the lower polaritons increases by four orders of magnitude, with increasing $k_\parallel$. The strong dependence of the effective polariton mass on the wave vector is relevant for relaxation dynamics, which are discussed in Sec. 2.5.

A more realistic description of polaritons in quantum wells includes the consideration of the finite lifetime of the two constituents, i.e. the cavity photons and the excitons. By introducing the decay rates for excitons γ_{exc} and cavity photons γ_{cav} it is also possible to define a further criterion for the existence of the strong coupling. The equation

$$g_0 \gg \hbar(\gamma_{\mathrm{cav}} - \gamma_{\mathrm{exc}})/2 \tag{2.27}$$

shows that the system is within the strong coupling regime, insofar as the energy exchange between the photons and excitons is faster than the lifetime

of the particles. If Eq. (2.27) is not fulfilled, the system is within the weak coupling regime and can be described by the initial eigenmodes of bare excitons and cavity photons. The lifetime of the polaritons can be determined by the Hopfield coefficients and the lifetime of the uncoupled exciton τ_{exc} and cavity photon τ_{cav}

$$\gamma_{\mathrm{LP}} = \frac{1}{\tau_{\mathrm{LP}}} = \frac{|X|^2}{\tau_{\mathrm{exc}}} + \frac{|C|^2}{\tau_{\mathrm{cav}}}, \tag{2.28}$$

$$\gamma_{\mathrm{UP}} = \frac{1}{\tau_{\mathrm{UP}}} = \frac{|C|^2}{\tau_{\mathrm{exc}}} + \frac{|X|^2}{\tau_{\mathrm{cav}}}. \tag{2.29}$$

The introduction of finite lifetimes also leads to a new definition of the polariton eigenenergies from Eq. (2.20), which therefore read as follows

$$\begin{aligned} E_{\mathrm{LP,UP}}(k_{\parallel}) = \frac{1}{2}\{[E_{\mathrm{exc}} + E_{\mathrm{cav}} + i\hbar(\gamma_{\mathrm{cav}} + \gamma_{\mathrm{exc}}) \\ \pm\sqrt{4g_0^2 + [E_{\mathrm{exc}} - E_{\mathrm{cav}} + i\hbar(\gamma_{\mathrm{cav}} - \gamma_{\mathrm{exc}})]^2}\}. \end{aligned} \tag{2.30}$$

In modern microcavities, the lifetime of polaritons is essentially determined by the lifetime of cavity photons $\tau_{\mathrm{cav}} \approx 1 - 10\,\mathrm{ps}$, whereby $\tau_{\mathrm{exc}} \gg \tau_{\mathrm{cav}} \gg g_0/\hbar$ is fulfilled and the energy of polaritons presented in Eq. (2.20) represent a good approximation of the polariton energy. The decay of the polariton results in the emission of a photon that conserves both the wave vector $k_{\parallel}$ and the energy of the polariton. The resulting one-to-one correlation between the polariton and the photon is based on the fact that the emitted photons are part of the wave function of the polariton [33]. This allows for an easy experimental approach to study the properties of the polaritons.

One of the most important properties of polaritons is the possibility to achieve macroscopic occupation of a coherent ground state, which, in analogy to the Bose-Einstein condensation of atomic gases, is called polariton condensation. However, since polaritons have a finite lifetime, polariton condensation takes place outside of thermal equilibrium. The following section gives a brief overview of the condensation of polaritons in microcavities.

2.5 Condensation of Microcavity Polaritons

Since polaritons are formed due to the strong coupling between quantum well excitons and cavity photons, which are bosonic in nature, polaritons

can also be regarded as bosons in the low-density limit. Bosons have the interesting property that they may accumulate up to huge numbers in a degenerate state. Accordingly, polaritons are also expected to pass through bosonic phase transitions such as Bose-Einstein Condensation (BEC). In principle, phase transitions like the BEC are possible whenever the average distance of the bosons becomes comparable to their de Broglie wavelength. The thermodynamic description of an ideal Bose gas, proposed by Albert Einstein, can be used to determine a dependence of the de Broglie wavelength on the critical temperature T_c for the BEC phase transition of the bosonic gas. In the following, this dependence will be derived, whereby the derivation mainly originates from Ref. [34].

2.5.1 The Ideal Bose Gas

A system consisting of non-relativistic and non-interacting bosons with mass m is considered. The energy E_p of the single-particle states depends quadratically on the momentum p of the states and is given by

$$E_p = \frac{p^2}{2m}. \tag{2.31}$$

The Bose-Einstein distribution describes the mean occupation number of bosons $\bar{n}_p$ in a single-particle state. It is given by

$$\bar{n}_p = \frac{1}{\exp[\beta(E_p - \mu(T))] - 1}, \tag{2.32}$$

with $\beta = 1/k_B T$ and the chemical potential $\mu(T)$ introducing the temperature dependence of the system. From Eq. 2.32 it follows immediately that $\mu \leq 0$, since a positive value of μ would lead to a negative mean occupation number. Furthermore, $\mu = E_p$ leads to a divergence of $\bar{n}_p$. After the occupation $\bar{n}_0$ of the ground state for $E_p = 0$ has been separated from the total number of particles N associated with the Bose-Einstein distribution, N reads

$$N = \bar{n}_0 + \sum_{p, p \neq 0} \bar{n}_p \tag{2.33}$$

In the thermodynamic limit, i.e. for systems where the size of the system and the number of particles increase indefinitely, the sum of Eq. (2.33) can be

replaced by an integral:

$$N = \bar{n}_0 + \frac{V}{(2\pi\hbar)^3} \int d^3p \ \bar{n}_p. \tag{2.34}$$

The calculation of the integral yields

$$N = \bar{n}_0 + \frac{V}{\lambda_T^3} g_{3/2}(z), \tag{2.35}$$

with the thermal de Broglie wavelength

$$\lambda_T = \frac{2\pi\hbar}{\sqrt{2\pi m k_B T}} \tag{2.36}$$

and the polylogarithm $g_{3/2}(z)$ with $z = \exp(\beta\mu)$. Since $\mu \leq 0$ Eq. (2.35) has a maximum value if the chemical potential μ amounts to 0. This is the case if the temperature falls below the critical temperature T_c. Below this temperature, a massive occupation of the ground state occurs. The critical temperature T_c can be calculated from Eq. (2.35) for $\mu = 0$ and one obtains

$$T_c = \frac{2\pi\hbar^2}{m k_b} \left(\frac{n}{\zeta(3/2)} \right)^{2/3}. \tag{2.37}$$

$n = N/V$ is the particle density and $g_{3/2}(1) = \zeta(3/2) \approx 2.6124$ is the Riemann zeta function.

Equation (2.37) shows that the critical temperature T_c for a phase transition of an ideal Bose gas into a BEC is inversely proportional to the mass of the bosons involved, which illustrates the great interest in polariton systems. Polaritons, which have a very low mass compared to atoms, allow polariton condensation even at room temperature. This is especially true for wide bandgap semiconductors where the exciton binding energy of excitons is particularly enhanced [35] or for organic semiconductors where the strong coupling regime with Rabi splittings of >150 meV could be achieved [36]. Polaritonic systems offer a much easier access to study the properties of condensation mechanisms than conventional atomic gases whose phase transition takes place only at very low critical temperatures. The phase transition of an atomic gas consisting of sodium atoms into a BEC, for example, takes place at critical temperatures of a few μ-Kelvin [37].

In principle, the condensation of polaritons takes place because large densities of polaritons can be generated, resulting in a massive occupation of the ground state, stimulated by various scattering processes. The most important scattering processes are presented in the following subsection.

2.5.2 Relaxation Dynamics

The previous discussion has shown that the phase transition into a condensed state can be achieved for polaritons at significantly higher temperatures as compared to atomic gases. This opens up the possibility to fabricate new devices from semiconductor microcavities that emit coherent light. The idea to use a polariton condensate as a new kind of coherent light source (polariton laser) was proposed in 1996 by Imamoglu et al. [38].

A key milestone in the direction of a polariton laser, was the experimental observation of the condensation of polaritons in CdTe [16]. The condensation took place after non-resonant optical excitation above a certain power threshold (THR). The main difference to experiments with resonant excitation, i.e. experiments in which the energy of the incident light corresponds to the energy of lower polaritons, is the emergence of a coherent ground state from an incoherent exciton reservoir. The relaxation mechanisms that ultimately lead from a populated exciton reservoir to polariton condensation are introduced hereafter.

In Fig. 2.6, a relaxation for relaxation of a hot electron-hole plasma into a polariton condensate is shown. The electron-hole plasma is generated by non-resonant excitation, where electrons and holes bind to excitons by emitting optical and acoustic phonons. This process is illustrated by the arrow pointing from the plasma to the excitonic resonance. Due to exciton-exciton and exciton-phonon scattering, the exciton bath further thermalizes to lower momentum states where it will ultimately couple to the light field and thus form highly excitonic polaritons. Above a critical polariton density, polariton-polariton scattering becomes effective and stimulated final-state scattering occurs into the ground state around $k_{\parallel} = 0$. From this state, polaritons spontaneously emit coherent monochromatic light, which has the advantage that no direct population inversion is required for this type of light source. The spontaneous emission of light out of the cavity arises due to the finite lifetime of the photons within the cavity. For this reason, the polariton condensate is called a non-equilibrium condensate, as the losses from the cavity mean that new carriers constantly have to be added to the system to achieve a steady state.

A quantitative analysis of the relaxation can be performed using semi-classical Boltzmann kinetics. Rate equations for the time dependent particle populations

of the excited states n_k(t) and the ground state n_0(t) at $k_\parallel = 0$ are given by

$$\frac{\partial n_0}{\partial t} = -\frac{n_0}{\tau_0} + \frac{\partial n_0}{\partial t}\Big|_{\text{LP-LP}} + \frac{\partial n_0}{\partial t}\Big|_{\text{LP-Ph}}, \tag{2.38}$$

$$\frac{\partial n_k}{\partial t} = P_k(t) - \frac{n_k}{\tau_k} + \frac{\partial n_k}{\partial t}\Big|_{\text{LP-LP}} + \frac{\partial n_k}{\partial t}\Big|_{\text{LP-Ph}}. \tag{2.39}$$

With the incoherent pumping rate $P_k(t)$, the lifetime of the excited state τ_k, and ground state τ_0. For LPs with a large wave vector, the lifetime is approximately given by Eq. (2.28) with $\tau_k = \tau_{\text{exc}}/|X|^2$, since the polaritons are highly excitonic. However, for decreasing wave vectors ($k_\parallel \to 0$), the polaritons become more and more photonic, significantly reducing their lifetime which can be approximated with $\tau_k = \tau_{\text{cav}}/|C|^2$. Furthermore, the populations n_0 and n_k depend on the respective rates of change given by polariton-phonon (LP-Ph) and polariton-polariton (LP-LP) scattering. Which rate dominates depends on the existing polariton density, which in turn depends on the optical pumping power.

First, the relaxation process is considered for low pumping powers for which LP-Ph scattering dominates. It is given by

$$\frac{\partial n_k}{\partial t}\Big|_{\text{LP-Ph}} = -\sum_{k'} \left(W^{\text{LP-Ph}}_{k\to k'} n_k (1 + n_{k'}) - W^{\text{LP-Ph}}_{k'\to k} (1 + n_k) n_{k'} \right), \tag{2.40}$$

with the transition rate $W^{\text{LP-Ph}}_{k'\to k}$. In Fig. 2.6, this process is shown on the large momentum part of the dispersion for polaritons with a huge excitonic fraction. The size of the red dots corresponds to the occupation number. In this region, the relaxation of polaritons mainly takes place via LP-Ph scattering, where polaritons release their energy via the emission of acoustic phonons, which is a process that conserves both energy and momentum. Since the cavity is not translationally invariant with respect to its growth axis z, the conservation of momentum is no longer valid and the emitted phonons can thus possess an arbitrary component in k_z. This circumstance enables dissipative processes, which may lead to polariton scattering directly into the ground state at $k_\parallel = 0$. However, the thickness of the quantum layer limits the component that an emitted phonon possesses in k_z, whereby the probability of the emission of a phonon for $k_z > 2\pi/L_{\text{QW}}$ decreases exponentially. This limits the energy loss of a polariton to about 2 meV per relaxation process, preventing immediate polariton relaxation towards the ground state [39].

To lose a large part of their energy, polaritons must therefore emit many acoustic phonons in order to reach the ground state. However, the probability of the emission of a phonon also depends on the excitonic fraction $|X|^2$ of the polariton, which decreases with each relaxation process. In the same way, the lifetime of polaritons decreases with increasing photonic component $|C|^2$. In the limit of low pumping powers, this leads to the fact that a large part of the polaritons only reach the so-called bottleneck region of the dispersion before they decay radiatively. This region at k_{Bot} is indicated by the largest red ball in Fig. 2.6.

For wave vectors below k_{bot}, the polariton-polariton scattering, which takes place within a few ps, is the dominating relaxation process. The scattering rate for polariton-polariton scattering is given by

$$\begin{aligned}\frac{\partial n_k}{\partial t}\Big|_{\text{LP-LP}} = -\sum_{k',k_1,k_2} W^{\text{LP-LP}}_{k,k',k_1,k_2}[n_k n_{k'}(1+n_{k_1})(1+n_{k_2}) \\ - n_{k_1} n_{k_2}(1+n_k)(1+n_{k'})],\end{aligned} \tag{2.41}$$

with the transition rate $W^{\text{LP-LP}}_{k,k',k_1,k_2}$ and the two scattered states $k_1 = k+q$ and $k_2 = k'-q$, as indicated in Fig. 2.6. This scattering process is momentum preserving, therefore, the total energy of the polariton gas does not decrease. An elastic scattering process is shown schematically in Fig. 2.6 for two polaritons with the same momentum $k = k'$. One polariton is scattered into the ground state, while the other polariton picks up the momentum and the energy of the first polariton. The presence of n_0 polaritons in the ground state (final-state) increases the scattering rate Eq. (2.41) by a factor of $(1+n_0)$. This mechanism, known as stimulated final-state scattering, is essentially responsible for the generation of polariton condensates.

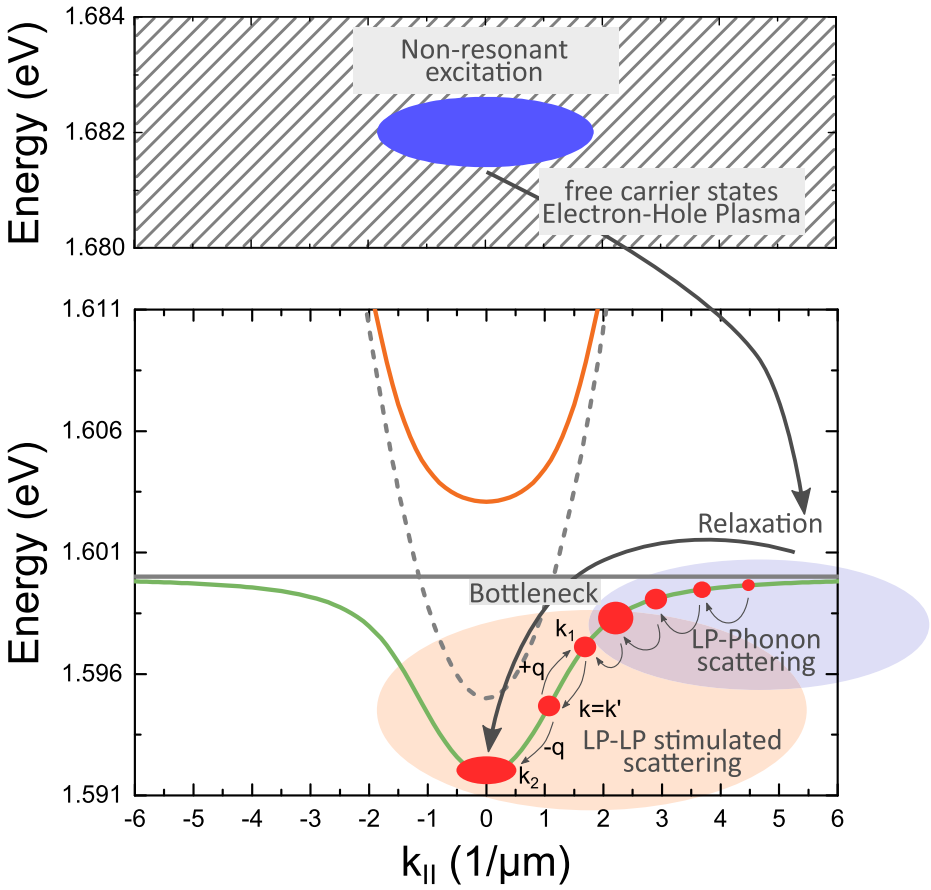

Figure 2.6: Schematic representation of the relaxation process after non-resonant excitation of a hot electron hole plasma. By emitting acoustic and optical phonons electrons and holes thermalize and finally form bound exciton states at large wave vectors. Through further scattering processes, the excitons lose momentum and form polaritons within the light cone. Final-state stimulated scattering finally causes the massive occupation of the polariton ground state above a critical polariton density.

Chapter 3

Experimental Methods

Figure 3.1: Basic requirements to create and detect exciton polaritons.

This chapter provides a detailed introduction to the experimental prerequisites for the generation and detection of polaritons. A setup that meets the basic requirements for the generation and detection of polaritons consists of three basic building blocks. However, this chapter is divided into two different sections in which the sample and signal detection part are combined. Within these sections, the respective parts of the experiment are discussed in detail. The sequence of the sections is based on the natural path of light through the optical setup.

Figure 3.1 shows a very basic concept of an optical setup design to create and detect polaritons. Starting with the generation of light from different laser sources and its manipulation by various optics (I), through the generation of polaritons within the sample (II), to the detection of the light emanating from the sample with the help of various detectors (III).

This chapter also serves the purpose of describing only the basic building blocks necessary to provide a fundamental understanding of the experimental

approach. This is possible, because the individual experiments share some similarities, hence a large part of the equipment and optics is reused in all experiments. Devices that are used specifically for an experiment will be introduced in detail in the respective chapter of the second part of this thesis.

In the first Section 3.1, the laser light generation and its manipulation on the way towards the sample will be discussed. For this purpose, the two laser systems used are introduced first. Initially, the pulsed laser is introduced briefly, in which the differences in the pulse durations used are discussed. Subsequently, the continuous wave laser used in the experiments and its special features are introduced. In the following, the possibilities of manipulating the laser light are briefly discussed. A more detailed description of the devices and optics used in particular is given in the respective sections in the second part of this thesis.

In addition to the laser light, low temperatures are required in order to cool down lattice vibrations of the investigated samples so that the formation of polaritons is possible. The cryostat that will be used throughout the measurements, provides the required temperatures and offers the possibility to attach the investigated samples. In addition, the cryostat offers the possibility to optically excite the samples in both reflection and transmission geometry. It will be presented in Section 3.2.

This section also introduces the various detectors used to study polariton emission. The requirements for the detectors include the ability to resolve the emitted light of the polaritons both temporally and spectrally. Since some polariton interactions are based on non-linear processes, it is also important to be able to investigate the intensity of the signal. Detectors that are able to meet all of these requirements will be presented one after the other.

3.1 Light Creation and Manipulation

The creation of polaritons in quantum wells is based on the possibility of using light to generate elementary excitations within the quantum wells, by absorbing a photon with an energy higher than the band gap energy of the material under consideration. In principle, this is also possible by electrical pumping, but is not discussed further in this thesis. However, the light must meet certain requirements in order to be absorbed and thus be able to create polaritons.

Using a laser (light amplification by stimulated emission of radiation) as a light source is very common, because lasers offer well-defined and controllable properties such as coherence, polarization, and high power densities. For the different experiments, we use two different basic concepts of lasers to study various polaritonic properties. The fundamental difference between these two concepts is the way the laser light is emitted, where distinction is made between pulsed lasers and lasers with a continuous wave (CW) emission.

The pulsed lasers that will be discussed here are basically divided into two different subgroups, depending on the duration of the emitted pulses. For simplicity's sake, the different pulse modes used in the experiments are designated by the pulse duration, namely picosecond (ps) or femtosecond (fs) pulses. The actual duration of the pulses is a ≈ 2 picoseconds for the ps pulses and ≈ 100 femtoseconds for the fs pulses. The duration of the pulses also affects the spectral width of the pulses due to the Fourier limit, i.e. the time-energy uncertainty. While the ps pulses with a spectral width of only 1 nm are spectrally moderately narrow, fs pulses have a spectral width of a few nm up to 20-30 nm depending on the actual pulse duration.

The Mira900 laser, developed by the company Coherent, offers the possibility to choose between ps and fs pulses. The heart of the Mira900 is a Titanium Sapphire (Ti:Sa) crystal which is optically pumped by a 10 W Verdi V10 CW laser. The wavelength of the Verdi V10 is 532 nm and the result of frequency doubling inside of the laser head which is pumped by a 50 W diode laser at 1064 nm. The Verdi laser is used to excite the gain medium of the Ti:Sa crystal over a broad range of wavelengths that can be filtered with an intracavity birefringent filter (BRF).

Since the BRF only acts as a rough filter, further modelocking of the longitudinal cavity modes is realized through exploitation of the optical Kerr effect. The optical Kerr effect takes place, when high intensity electrical fields propagate trough a medium. High intensive light fields cause a local perturbation within the gain medium which results in a spatially varying of the refractive index. A change of the refractive index changes the group velocity of the light field that passes through, resulting in the so-called Kerr-lensing effect. Only the modelocked light pulses are of sufficiently high intensity to form this Kerr lens.

The beam now consists of different modes at different transversal positions of the beam, in which the desired modelocked pulse modes are in the center of

the beam. A slit is positioned inside the cavity in order to spatially filter only the modelocked pulses. Since only the modelocked pulses are guided back into the cavity after they have been partially reflected at the output coupler, only these pulses are amplified by stimulated emission inside of the Ti:Sa crystal.

Depending on the desired pulse duration, two different cavity geometries can be selected. For fs pulses, a geometry is selected which employs two prisms to compensate for the group velocity dispersion. To generate ps pulses, a different geometry is selected in which a Gires-Tournois interferometer (GTI) compensates for the dispersion. Regardless of the selected geometry, both cavities generate a pulse repetition rate of 75.4 MHz, which means a pulse separation of 13.3 ns.

Pulsed laser systems are extremely well suited for studying the dynamics of polaritons. However, if the dynamics of polaritons are not the main focus, but high spectral resolution becomes important, continuous wave lasers can be used to provide information about the behavior of polaritons. These CW lasers are also extremely useful for studying the bistability of polaritons, as the CW laser provides a constant illumination of the sample and thus a constant generation of polaritons.

For this purpose, a high power stabilized single-mode ring CW laser with a very small linewidth of < 50 kHz is used. Similar to the pulsed laser system already presented, a Ti:Sa crystal is optically pumped by a 10 W Verdi CW pump laser source. The M-Squared SolsTiS laser system used in our studies, provides up to 2 W of laser power with stabilized single-mode CW emission.

As already mentioned, a laser has well defined properties which can be manipulated by different methods. The polarization of the light, the laser intensity, the separation between laser pulses, or the phase and thus the shape of the wavefront can be changed. In the following, different methods are introduced, with the help of which it is possible to modify these properties.

Typically, the polarization of the laser is changed by retardation plates, also called wave plates. Due to their crystal structure they are birefringent, which means that they have different refractive indices for light fields aligned along different crystal orientations. The different refractive indices influence the velocity of the different components of the light field as they pass through the crystal. In the crystal itself, a distinction is made between the slow and the fast axis. The different propagation velocities lead to a phase shift of the light field components aligned along the different axes. Ultimately, the

relative phase shift leads to a rotation of the polarization. In our experiments we mainly use $\lambda/2$ and $\lambda/4$ wave plates to manipulate linear, elliptical, and circularly polarized light.

In the following, further methods are briefly introduced with the help of which it is possible to change further properties of the laser light. On the one hand, a method is presented which makes it possible to tailor the number of pulses. On the other hand, it is also possible to change the spatial phase distribution of the laser. These experimental methods are discussed in more detail in the respective chapters of the second part of this thesis.

The pulsed laser provides a huge number of consecutive pulses. The pulse separation of 13.3 ns is usually sufficient for observing polariton related processes, since the lifetime of polaritons is three orders of magnitude shorter than this period. However, if this time is no longer sufficient for polariton related processes if they persist significantly longer, it is helpful to change the repetition rate of the pulsed laser. In the simplest case, this is achieved by installing a fast rotating chopper that cuts out individual pulse trains from the constant train of consecutive pulses. If, however, the effects of only a few pulses within a train of pulses have to the polariton system are of interest, the chopper is not fast enough to cut out pulse trains in this time regime. A device that is fast enough and, moreover, offers the possibility to filter out the number of pulses down to single pulses, is realized by an electro-optical modulator (EOM).

The EOM is based on the Pockels effect, which leads to a change or generation of birefringence in a medium due to an applied electric field. Ultimately, the polarization of the passing light is rotated. Additional Glan-Thompson prisms in front and behind the Pockels cell act as a polarization dependent filter. A high voltage supply, coupled to a function generator, applies a voltage gate to the Pockels cell which creates a time-dependent rotation of the polarization. The length of the voltage gates, which are generated by the function generator, can be adjusted arbitrarily, whereby the generation of pulse trains consisting of only single pulses is possible. This method is used in Chapter 6 of the second part of this thesis.

Usually, the spatial intensity distribution of the laser spots used corresponds to a two-dimensional Gaussian distribution. This spatial intensity distribution is used to generate a rotationally symmetric distribution of carriers within the sample. Two-dimensional Gaussian distributions can easily be treated in

theory, especially for the theoretical prediction of the condensation behavior of polaritons in quantum wells. However, Gaussian distributions are not suitable for investigating the condensation behavior, which takes place decoupled from the location of the optical pump. For this purpose, the two-dimensional intensity distribution is changed into the shape of a ring, which serves as an optical trap. For optical pumping above the condensation threshold, a polariton condensate forms within the trap, which cannot escape from the trap due to the annular potential of background charge carriers surrounding it.

A purely optical solution for the generation of annular intensity distributions, which serve as optical traps, is made possible by axicon lenses. However, these lenses have the disadvantage that they can only be used to generate annular optical potentials of a certain size. A possibility to generate optical potentials of any shape and size is realized by a spatial light modulator (SLM).

There are different types of SLMs, depending on whether the amplitude, the polarization, or the phase of the light is modulated. The PLUTO-2 phase only SLM presented below is based on the liquid crystal on silicon (LCOS) technology and is manufactured by HOLOEYE. The LCOS micro display consists of a 1920x1080 full HD chip with a pixel size of $8\,\mu$m and a filling factor of 93 %. The liquid crystals are arranged on a silicon layer, where each pixel is set to a gray level with 8 bit color depth via the graphics card of a PC. The 256 gray values correspond to an applied voltage that changes the spatial orientation of the liquid crystals. Due to the optical anisotropy of the liquid crystals, their refractive index changes as a function of the applied voltage, leading to a change in the optical path length within the liquid crystals. Thus, the applied gray levels correspond to a conversion into a phase shift, allowing for a phase shift of 2π.

With this technique it is possible to imprint any phase map on a light beam that initially has a flat wavefront. The supplied software generates the corresponding phase pattern from the desired intensity pattern. Ultimately, all that is needed is another optical system, such as a microscope objective, to convert the phase pattern into an intensity pattern. This works due to the property of a lens to perform a spatial Fourier transformation of the incident light. This property will be discussed in detail in the next section along with other detection methods.

3.2 Polariton Creation and Detection

The creation and manipulation of light fields are the first important prerequisites for the creation of polaritons. In the next step, the cryostat is presented. In the following, the different excitation methods, which differ in the geometry of the optical setup, as well as with the choice of the laser type and energy are presented. Subsequently, the various detectors used in the different experiments are introduced. Here, the preparation of the signal coming from the sample will be discussed. The preparation of the signal includes some of the methods already discussed in the previous section such as filtering the polarization of the signal. In addition to that, a method to image the Fourier space of the sample emission will be introduced. The discussion of the cryostat and the detectors concludes this chapter and therefore this part of the thesis.

Since polaritons are the result of the strong coupling between excitons and photons, a stable formation of excitons has to be achieved. In order to achieve a stable formation of excitons, the kinetic energy of free particles must be reduced below the binding energy of the excitons ($E_b^{GaAS} = 4\,\mathrm{meV}$ [25]). On the basis of the kinetic theory of gases, the kinetic energy of a free particle in an ideal gas is given by

$$E = \frac{3}{2} k_B T, \tag{3.1}$$

with the Boltzmann constant k_B and the temperature T of the ideal gas [40]. For temperatures below 32 K, a stable formation of excitons and thus a possible formation of polaritons can be achieved. Typically, cryostats are used to achieve those very low temperatures.

Throughout all experiments, a continuous helium flow cryostat is used. The sample is attached to the cold finger of the cryostat. The position of the cryostat and thus the position on the sample can be adjusted in x-, y- and z-direction via translation stage. Inside the cryostat, two cernox resistors ensure that the temperature is constantly monitored. In addition to the permanently installed cernox on the heat exchanger, another cernox is used to monitor the temperature in the immediate vicinity of the sample directly on the cold finger. These resistors serve on the one hand as a means to control the temperature, but also as a feedback for a temperature controller. This controller regulates the internal heating coil of the cryostat and thus keeps the temperature of the sample constant. At high flow rates of helium it is possible to maintain constant temperatures down to 6K. However, since such low temperatures are

not necessarily required, the temperatures during the experiments are typically between 10 K and 15 K. These temperatures are still way below the thermal dissipation temperature of the excitons, as calculated in the last paragraph.

Since the same cryostat is used for all of the experiments, the only differences between the experiments are the type and geometry of excitation and the sample being studied. Also, the choice of the detector used changes depending on the properties of interest of the polaritons being studied. In the following, the different methods for the creation of polaritons are presented. The description of the examined samples takes place in the respective chapters in the second part of this thesis.

Basically, polaritons can be excited by both pulsed and CW lasers, which have already been discussed in the previous section. Depending on the choice of the energy of the laser, a distinction is made between resonant, quasi-resonant, and non-resonant excitation. However, for all of the relevant excitation methods the excitation light has to be filtered out, since the intensity of the excitation laser is many times higher than the signal from the sample. There are different ways to filter out the excitation light. For experiments with resonant excitation and in transmission geometry, the sample itself can be used as a filter, since the stop band of the DBR structure acts as highly efficient mirror, through which only a small spectral region of the light can be transmitted. For experiments in reflection geometry, longpass filters can be used to separate the excitation light from the polariton signal. Both geometries will be presented in the following.

In order to filter out the excitation light using the sample, an optical setup in transmission geometry is chosen. The sample is attached to the cold finger of the cryostat. The light is guided from the backside of the cryostat onto the sample through a recess of 6 mm x 2 mm inside of the cold finger and collected by a microscope objective in the direction of propagation. In order to generate excitation spots as small as possible, the light is focused on the sample by using suitable lenses. The respective details for both experiments in which the transmission geometry is applied, are discussed in depth in section 5.1 and 6.1.1 in the second part of this thesis.

In principle, the configuration in transmission geometry can also be used for non-resonant excitation. However, if the sample design does not allow for excitation through the substrate of the sample, the optical alignment is changed to a confocal setup in reflection geometry. A typical confocal setup

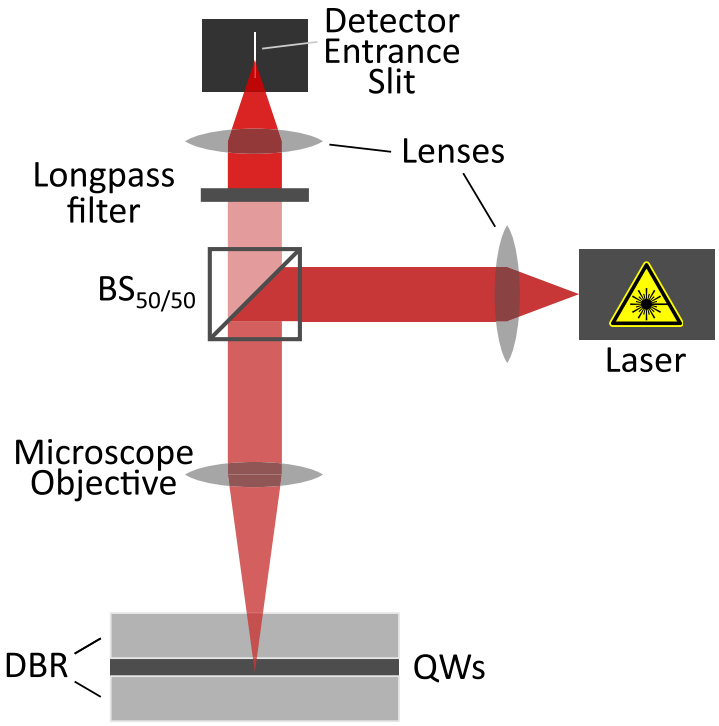

Figure 3.2: Basic principle of an optical confocal setup. $BS_{50/50}$: beamsplitter with 50% reflection and 50% transmission. The incident transmitted beam is omitted for simplicity. The spectrally filtered signal is focused through a lens onto the entrance slit of a detector of choice.

is displayed in Fig. 3.2. Using a 50/50 beamsplitter, the excitation laser is guided to a microscope objective where it gets focused down to spot sizes in the micrometer regime. The same microscope objective gathers and collimates the light coming from the sample and guides it back through the beamsplitter in transmission direction. Since, the light still contains both the signal as well as the reflected excitation laser itself, a longpass is used to filter the light. The longpass filter separates the reflected excitation laser from the signal of the polaritons. Since the beam then only contains the information of interest, this information can be examined by various detectors.

Depending on the nature of the experiment, the signal of the polaritons contains a huge variety of information. By the use of specific detectors, it is possible to investigate the relevant properties of the polaritons. This includes the polarization, the lifetime, the coherence, the spatial and angular distribution of the emission, the spin, or the spectral information of the polaritons. Similar

to the already introduced longpass filter, it is necessary to make use of specific components and experimental techniques to acquire only the relevant properties of the polaritons. These properties can then be specifically analyzed by the respective detectors, wherein a distinction is made between time-integrated and time-resolved measurements. In the following, the components and techniques as well as the different detectors are presented.

The first step is to ensure that the sample lies in the focus of the microscope objective. A flip mirror located on the central beam axis is used to image the sample surface with a f=400 mm lens on a CMOS chip. The obtained intermediate image offers the advantage of a very fast feedback during the experiment.

One method to perform time-integrated measurements is to measure the spectral characteristics of the signal which is done by using a 500 mm monochromator. The signal is diffracted through a 1200 lines/mm grating into its spectral components and recorded by a liquid nitrogen cooled CCD camera with 1340x400 pixels. The spectral resolution of this configuration is about 40 μeV/pixel. If the grating is set to zero order no diffraction of the light takes place and the monochromator can be used to record the real space image of the sample emission.

If instead of the spectral information, the light intensity of the signal is to be measured, photodiodes (PD) can be used. Photodiodes in general are operated in two different modes, namely photoconductive and photovoltaic mode. For time-integrated measurements, a multimeter is used to record and read the built-up voltage in photovoltaic mode of the photodiode. This is used specifically to investigate the non-linear behavior of polaritons in the bistable regime, presented in Chapter 6.

For the investigation of time-varying light sources, photodiodes are operated in photoconductive mode. Here, the temporal behavior of the source can be investigated with an oscilloscope, depending on the bandwidth of the photodiode, since the bandwidth is a measure for the time response t_{R} of the photodiode, following roughly:

$$t_{\mathrm{R}} = \frac{0.35}{f_{\mathrm{BW}}}. \tag{3.2}$$

Within the relevant experiments in Chapter 6, a InGaAs photodiode with a bandwidth of $f_{\mathrm{BW}} = 400\,\mathrm{MHz}$ is used. This results in a time response of approximately $t_{\mathrm{R}} = 1\,\mathrm{ns}$.

Fast photodiodes are also used to create a trigger signal for different devices such as oscilloscopes, the delay generator, or the streak camera. The latter has a very high temporal resolution of approximately 2 ps and is therefore able to resolve the very short lifetime of polaritons inside microcavities. In the following, the functional principle of the streak camera will be discussed briefly.

The Hamamatsu streak camera with the fast synchroscan unit can resolve the photoluminescence (PL) of constituents with a very short lifetime in the range of tens of ps. The signal falls onto a photocathode through a fine slit in the input optics of the streak camera, where the incoming photons are converted into photoelectrons. The number of photoelectrons corresponds to the intensity of the incoming light. In the case of very weak intensities, the number of electrons can be multiplied using the micro channel plate (MCP). Here, a single electron can be multiplied into 10^4 electrons. A high-speed sweep of a high frequency sine wave is applied to deflection electrodes to deflect the electrons vertically, depending on the time of arrival. The frequency of the applied high-speed sweep is synchronized to the pulsed laser system, using a fast photodiode. The electrons hit a phosphor screen where they, depending on their time of arrival, accumulate along the vertical, hence temporal, axis . A CCD camera with a CMOS chip with 640x480 pixels is used to image the phosphor screen. For the fastest sweep time, a temporal resolution of about 2-3 ps is achieved. The time-resolution per pixel is higher, but the signal has a finite size of a few pixels. Therefore, the size of the signal has to be minimized before starting time-dependent measurements.

The entrance slit of the streak camera is aligned horizontally and thus allows only one spatial dimension (x) and the temporal dimension (t) to be recorded. To record the second spatial dimension, an automated moving lens is installed in front of the streak camera, which focuses the signal on the entrance slit. The resulting sectional images along the y-direction can be rearranged during data evaluation. With this technique it is possible to record videos of the two-dimensional image plane, with a high temporal resolution. This technique is used in Chapter 4 to record the angular distribution of the polariton emission in Fourier space. In Chapter 5, this technique is used to record the 2D real space image of the evolution of optically perturbed polaritons trapped in an annular optical potential.

The Fourier space, also called reciprocal or simply k-space, represents the space of spatial frequencies. A lens, that images the rear focal plane of the

microscope objective, provides access to the k-space. In Fig. 3.3 the basic property of a lens to perform a Fourier transformation of the incident light is shown. The maximum angle that can be captured by a lens depends on the numerical aperture (NA) of the lens. The 20x microscope objective used has a NA of 0.4 which corresponds to an angle of 23.6° relative to the direction of normal incidence.

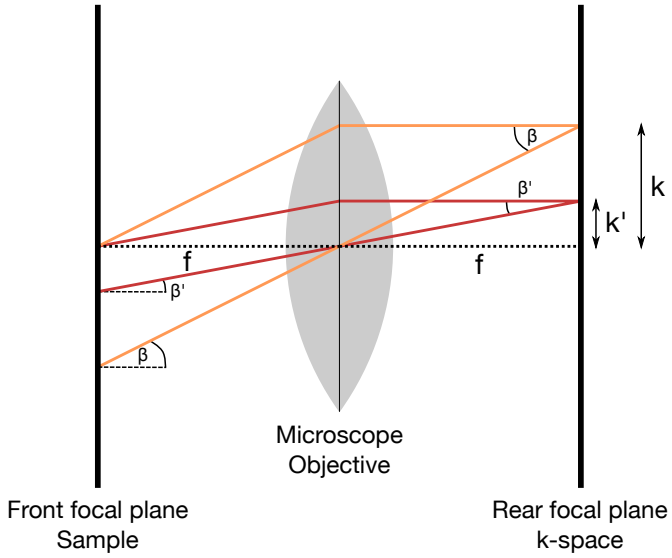

Figure 3.3: Schematic drawing of how a lens performs a Fourier transform of light that is emitted under different angles. Light emitted under the same angle is imaged onto the same position in k-space. Adapted from [41].

In the different experiments, a combination of lenses is used to record the emitted light from polaritons in k-space with the streak camera or the monochromator. Since there is a one-to-one correlation between the emission angle and the polariton wave vector, it is possible to make the dispersion of the lower polariton branch visible using the monochromator. If the vertical k-space is scanned using a lens mounted to the automated translation stage on the streak camera, it is also possible to record videos of the k-space evolution. This method is discussed in detail in Chapter 4.

The introduction of Fourier space concludes the experimental methods chapter, since all requirements for the experiment to investigate the various properties of polaritons are fulfilled. The results of these investigations are presented and discussed in detail in the second part of this thesis.

Part II

Results

Chapter 4

Optical Spin Hall Effect

Following the first theoretical description of the Hall effect of light by Onoda et al. [42], the optical spin Hall effect (OSHE) for polaritons was introduced theoretically by Kavokin et al. [43] in 2005. It has been observed experimentally two years later by Leyder et al. [44]. It describes the connection between the spin Hall effect (SHE) that has been proposed by D'yakonov and Perel' in 1971 [45] and the polarization dependent Rayleigh scattering of polaritons in semiconductor microcavities. The connection between the SHE and the OSHE is the separation in real- and momentum space after elastic scattering of polaritons on static disorder potentials inside the quantum well took place. The SHE describes the spin-dependent separation perpendicular to the current of charged carriers with half integer spins such as electrons.

The description of the SHE distinguishes between intrinsic and extrinsic SHE. The intrinsic SHE is caused by the spin-splitting in the conduction band caused by the spin-orbit interaction. The extrinsic SHE describes the spin-flip scattering of charge carriers on crystal impurities. An analogy to the extrinsic SHE exists in the form of elastic Rayleigh scattering of moving polaritons in quantum wells embedded in microcavities.

A flow of polaritons can be generated by resonant excitation of the LPB at a non-zero angle with respect to the normal vector of the microcavity. The correspondence between the energy and the emission angle of polaritons allows easy access to inject polaritons with non-zero momentum ($\boldsymbol{k}_{\parallel} \neq 0$) using this method. If the flow of polaritons is specifically directed towards a crystal impurity, elastic Rayleigh scattering of the polaritons leads to a redistribution of the polariton wave vectors. Elastic Rayleigh scattering conserves both momentum and the initial polarization which ultimately leads to the formation of a scattering ring in k-space with a radius defined by the absolute value of the initial $|\boldsymbol{k}_{\parallel}|$. The experimental details for the generation of resonant

Rayleigh scattering of polaritons at sample defects are explained in section 4.2.

Due to an effective magnetic field $\boldsymbol{\Omega}_{\vec{k}}$ that arises because of the longitudinal-transverse splitting of polaritons within microcavities, the spin polarization of the scattered polaritons differs depending on the flow direction after the scattering process. The spin polarization of polaritons as well as the dynamics can be described within the framework of the pseudospin model [46]. Both, the origin of the effective magnetic field, as well as the coupling of the polariton pseudospin to the effective magnetic field are introduced and discussed in detail in Sec. 4.1. The coupling of the polariton pseudospin to the effective magnetic field is referred to as self-induced Larmor precession which ultimately leads to spin relaxation of the polaritons.

The dynamic of this relaxation process is investigated experimentally in Sec. 4.3, where a special focus is placed on the degree of circular polarization ρ_c of the polaritons. Here, the model presented in Ref. [43], for the description of the effective magnetic field, is extended by further contributions which reproduce the experimental results.

The results presented in this chapter have been published in similar form in Refs. [47, 48]. Also, some of the results presented in this chapter are presented in similar form in the Master thesis of B. Berger [49], which the author of this thesis has supervised.

4.1 Origin of the Effective Magnetic Field

The investigation of the spin relaxation process of polaritons in quantum wells embedded in semiconductor microcavities presented here, follows mainly the theoretical description of spin dynamics given in Refs. [43, 46]. Since polaritons are composite bosons made up of strongly coupled cavity photons and excitons, the spin relaxation processes they are undergoing will be described in the framework of the pseudospin [46, 50]. The pseudospin describes a coherent superposition of the optically active exciton spin doublet state, that can be either spin up (+1) or spin down (-1). In addition, the pseudospin reflects the polarization state of the polaritons, whereas the polarization states ± 1 represent right- (σ^+) and left-handed (σ^-) circular polarizations of polaritons, respectively. In this context, the pseudospin $\boldsymbol{S}_{\boldsymbol{k}}$ corresponds to the conventional Stokes vector $\boldsymbol{S}_{\boldsymbol{k}} = (S_x, S_y, S_z)$. The pointing direction of $\boldsymbol{S}_{\boldsymbol{k}}$ on the surface

of a given Poincaré sphere corresponds directly to the polarization state of the polaritons (see Fig. 4.1).

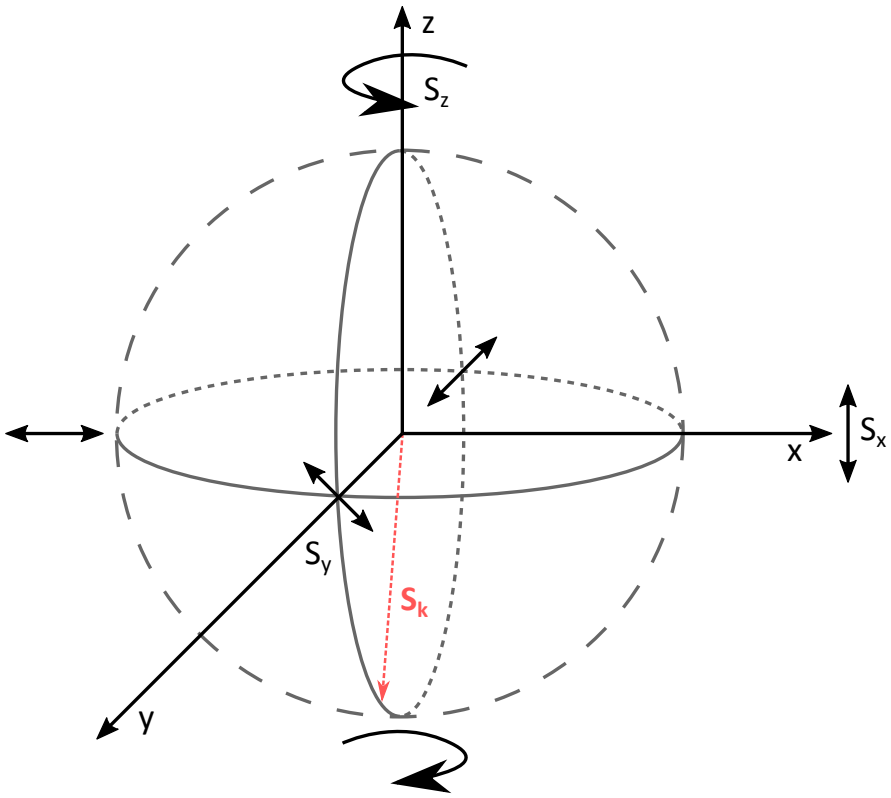

Figure 4.1: Poincaré sphere with the projection of the pseudospin vector $\boldsymbol{S_k}$ shown in light red. The black arrows represent the orientation of the polarization of polaritons. The equatorial plane corresponds to all possible linear polarizations. The polarization at the poles corresponds to circular polarizations. All other polarizations correspond to an elliptical polarization. Adapted from [46].

The temporal evolution of the pseudospin and the associated spin relaxation of polaritons is mainly governed by an effective magnetic field $\boldsymbol{\Omega_k}$ inside the microcavity, causing a precession of the pseudospin [46, 51, 52]. The precession equation therefore describes the temporal evolution of the polariton pseudospin in the scattered state $\boldsymbol{S_k}(t)$ which is given by [43, 44, 53]

$$\frac{\partial \boldsymbol{S_k}}{\partial t} = \boldsymbol{S_k} \times \boldsymbol{\Omega_k} + \boldsymbol{f}(t) - \frac{\boldsymbol{S_k}}{\tau}. \tag{4.1}$$

The population of the scattered state N_k is given by the rate equation [47]

$$\frac{\partial N_{\boldsymbol{k}}}{\partial t} = f(t) - \frac{\partial N_{\boldsymbol{k}}}{\tau}. \tag{4.2}$$

Here, the inflow of polaritons from the initial pseudospin state $\boldsymbol{S}_{\boldsymbol{k_0}}$ into the scattered state $\boldsymbol{S}_{\boldsymbol{k}}$ is given by $\boldsymbol{f}(t)$ and [43]

$$\boldsymbol{f}(t) = 2\frac{\boldsymbol{S}_{\boldsymbol{k_0}}}{\tau_1} e^{-t/\tau}. \tag{4.3}$$

τ_1 is the scattering time of the scattering process. The last terms in the Eqs. (4.1) and (4.2) describe the finite lifetime of the polaritons which decay radiatively with the time constant τ.

The first term in Eq. (4.1) describes the aforementioned coupling of the pseudospin $\boldsymbol{S}_{\boldsymbol{k}}$ to the effective magnetic field $\boldsymbol{\Omega}_{\boldsymbol{k}}$. The direction of the effective magnetic field $\boldsymbol{\Omega}_{\boldsymbol{k}} = (\Omega_x, \Omega_y, \Omega_z)$ is determined by the sum of the field vectors representing different origins of the effective magnetic field

$$\boldsymbol{\Omega}_{\boldsymbol{k}} = \boldsymbol{\Omega}_{\boldsymbol{k}}^{\mathrm{LT}} + \boldsymbol{\Omega}_{\boldsymbol{k}}^{\mathrm{an}} + \boldsymbol{\Omega}_{\boldsymbol{k}}^{\mathrm{NL}}. \tag{4.4}$$

In the following, the nature of the different field vectors that constitute $\boldsymbol{\Omega}_{\boldsymbol{k}}$ will be elaborated.

The first term in Eq. (4.4) $\boldsymbol{\Omega}_{\boldsymbol{k}}^{\mathrm{LT}}$ corresponds to the effective magnetic field originating from the longitudinal-transversal (LT) energy splitting Δ_{LT} of the linear polarizations. The LT splitting splits the energy of the polariton mode depending on the angle between the wave vector and the orientation of the linearly polarized excitation and it is caused by two factors. First, because of the TE-TM splitting of the cavity mode that is caused by the mismatch between the central frequency of the stop band ω_s and the resonator frequency ω_c of the cavity. ω_s changes slightly with the angle of incidence θ following $1/\cos\theta$, which leads to a larger splitting for a larger angle of incidence [29]. Second, if the dipole moments of polaritons with nonzero in-plane wave vectors have different energies parallel and perpendicular to the wave vector, the splitting is zero for $\boldsymbol{k} = 0$ and increases following a square root law for large wave vectors. This is referred to as the longitudinal-transverse splitting and is caused by the long-range exchange interaction of the excitons [46, 54].

$\boldsymbol{\Omega}_{\boldsymbol{k}}^{\mathrm{LT}}$ is oriented along the equatorial plane of the Poincaré sphere and the strength of the field depends on the in-plane momentum as well as on the size

of the splitting Δ_{LT}. It is given by

$$\boldsymbol{\Omega}_{\boldsymbol{k}}^{\mathrm{LT}} = [\Delta_{\mathrm{LT}}(k_x^2 - k_y^2), 2\Delta_{\mathrm{LT}} k_x^2 k_y^2, 0]. \tag{4.5}$$

k_x and k_y depict the in-plane momentum and they are given by the respective components of the pseudospin vector $\boldsymbol{S}_{\boldsymbol{k}}$.

The second effective magnetic field component in Eq. (4.4) arises due to the in-plane anisotropy of the sample, that might be introduced during the growth process using molecular beam epitaxy. The in-plane anisotropy is caused by monolayer fluctuations at each interface leading to anisotropic excitonic or photonic disorder. If these fluctuations occur mainly along one particular crystallographic axis, these fluctuations might pin the linear polarization along this axis. The resulting in-plane asymmetry leads to a splitting of the linear polarizations even at $\boldsymbol{k} = 0$ [55]. Another source of linear polarizations splittings in microcavities is the strain induced crosshatch disorder, due to the high number of DBR layer pairs with mismatched lattice constants [56]. A brief overview of the crosshatch pattern observed in the investigated sample is given in Sec. 4.2.1.

To connect the anisotropy of the sample to the effective magnetic field, we assume a uniform field contribution δ_{an} along the x-axis which is given by [47]

$$\boldsymbol{\Omega}_{\boldsymbol{k}}^{\mathrm{an}} = [\delta_{\mathrm{an}}, 0, 0]. \tag{4.6}$$

The first two contributions to the total effective magnetic field $\boldsymbol{\Omega}_{\boldsymbol{k}}$ only point along the in-plane directions. However, due to non-resonant excitation of polaritons, strong nonlinear polariton-polariton interactions are expected. These interactions give rise to the last term of the total effective magnetic field in Eq. (4.4) that points along the growth axis of the microcavity [47]

$$\boldsymbol{\Omega}_{\boldsymbol{k}}^{\mathrm{NL}} = [0, 0, \beta S_z], \tag{4.7}$$

with β as the effective polariton-polariton interaction constant. It also takes into account the different strength of the exchange interactions between polaritons with the same spin and polaritons with opposite spin configurations.

$\boldsymbol{\Omega}_{\boldsymbol{k}}^{\mathrm{NL}}$ arises due to an imbalance of the concentrations of circularly polarized polariton populations [57, 58] and is responsible for the so-called self-induced Larmor precession of the linear component of an elliptically polarized polariton pseudospin [59].

The investigation of the temporal evolution of the pseudospin and therefore the evolution of the polariton polarization is realized by measuring the time-resolved degree of circular polarization (DCP) ρ_c. In Fig. 4.2 a scheme of the DCP distribution in momentum space is shown. Depending on the scattering angle θ_s the pseudospin points into different directions on the Poincaré sphere, which corresponds to a change in the direction of the effective magnetic field. For polaritons propagating along certain in-plane directions, the coupling of the polariton pseudospin to the effective magnetic field leads to different pseudospin polarizations. The DCP reaches maximum (minimum) values of

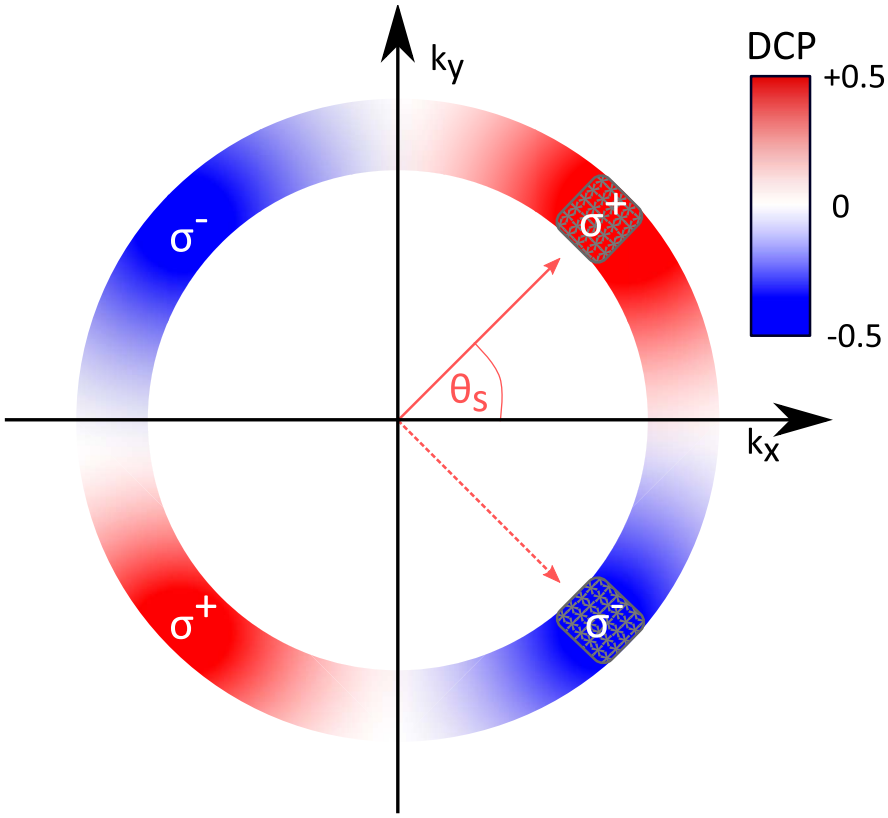

Figure 4.2: Scheme of the scattering ring in momentum space. The degree of circular polarization changes depending on the scattering angle θ_s and therefore the direction of motion of the polaritons. The DCP changes from -0.5 (blue) to 0 (white) to +0.5 (red). The light red arrows indicate scattering angles of $\theta_s = +45°(-45°)$, where the DCP has its maximum (minimum) value, respectively. The shaded areas at $\theta_s = \pm 45°$ indicate the positions of which the time-resolved intensities are extracted in the analysis following Eq. (4.8).

$+0.5(-0.5)$ for scattering angles of $+45°$, $-135°$ ($-45°$, $+135°$) [43]. The DCP can be extracted from time-resolved PL measurements using the PL intensities $I_{\sigma^{+/-}}$ of both maximum (minimum) circular polarization values following

$$\rho_c = \frac{I_{\sigma^+} - I_{\sigma^-}}{I_{\sigma^+} + I_{\sigma^-}}, \tag{4.8}$$

from the corresponding k_y positions for a scattering angle of $\theta_s = +45°(-45°)$.

The exact methodology for extracting the DCP from time-resolved measurements is given in the following section which illustrates the experimental setup.

4.2 Experimental Details

The investigated sample C1575 consists of six 3.3 nm wide $In_{0.1}Ga_{0.9}As$ QWs each separated by a 10 nm GaAs barrier, which yields a Rabi splitting of about 6 meV. The QWs are placed in the antinodes of the cavity mode of the λ-cavity. The cavity is sandwiched by the top and bottom DBR structures which are made out of 26(30) top(bottom) alternating GaAs/AlAs layer pairs. The Q-factor of the cavity has been measured to approximately 6000. Because of the slight wedge of the cavity, it is possible to vary the detuning between the optical resonance with respect to the exciton energy from approximately 20 meV to -10 meV. For this experiment the detuning has been set to fixed value of $\delta = -5.3$ meV.

The DBR structure is grown on a polished GaAs substrate in order to open up the possibility to perform measurements in transmission geometry. The band gap energy of the InGaAs QWs is smaller than the band gap energy of GaAs, resulting in a transparent GaAs substrate for resonant excitation.

A schematic layout of the setup is shown in Fig. 4.3. Resonant optical excitation is performed using the pulsed Titanium-Sapphire laser with a repetition rate of $\nu_{\text{rep}} = 75.4$ MHz and picosecond pulses. The laser is centered at a wavelength of 848.86 nm which corresponds to an energy of about 1.4606 eV. It has a linewidth of about 560 μeV. The excitation scheme is shown in Fig. 4.4. The energy as well as the linear polarization of the laser are set to resonantly excite the TM mode of the LPB under non-normal incidence. In order to control the angle of incidence of the laser, the laser beam is guided through

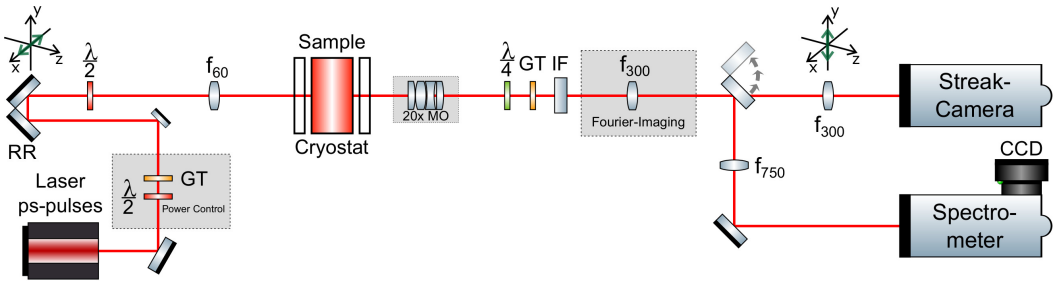

Figure 4.3: Schematic layout of the setup used to investigate the OSHE. GT, Glan-Taylor prism. RR, retro-reflector. MO, microscope objective. IF, interference filter. CCD camera, charged-coupled device camera.

the $f = 60\,\mathrm{mm}$ lens such that it is not centered. To position the laser beam, a retro-reflector is mounted on a one-dimensional translation stage, which adjusts the laser beam perpendicularly to the beam direction. The angle of

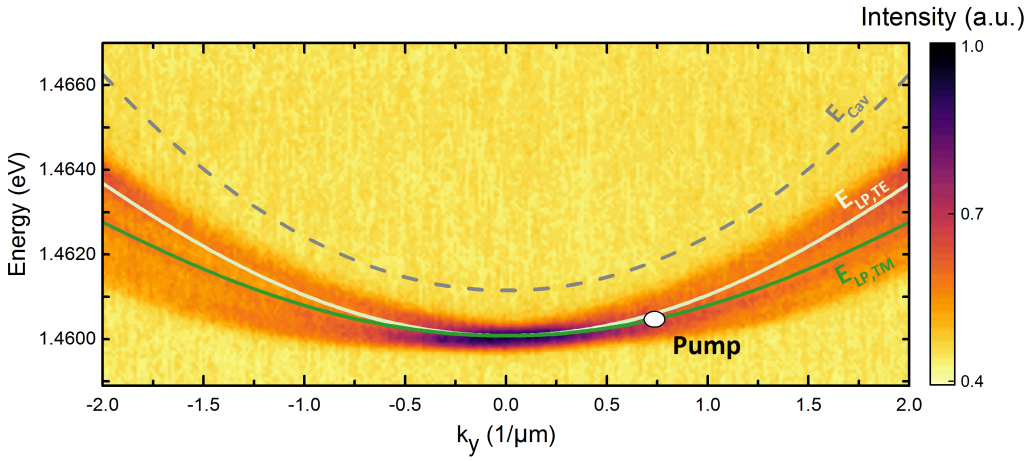

Figure 4.4: Excitation scheme with the energies of the TE/TM modes of the LPB as well as the energy of the cavity. The PL of the LPB has been acquired by non-resonant excitation with low excitation power. The energy, the angle of incidence, and the polarization of the laser are set to 1.4606 eV, $k_{\parallel} = 0.73\,\mu\mathrm{m}^{-1}$, and linear polarization to resonantly excite the TM mode of the LBP, as indicated by the white pump spot. Adapted from Ref. [47].

incidence of the laser is set to excite the sample resonantly with a wave vector of $k_{\parallel} = 0.73\,\mu\mathrm{m}^{-1}$. The spot diameter measures $20\,\mu\mathrm{m}$ and the power has been set to 15 mW throughout the measurements. The sample is mounted on the cold finger of a continuous helium-flow cryostat. The small recess on the sample holder provides optical access to the sample. The temperature

controller ensures that a constant temperature of 15 K is maintained.

The transmission is collected using a 20 x magnification microscope objective that has a NA of 0.4 . A f=300 mm lens is placed behind the microscope objective to image the Fourier plane, i.e. the the rear focal plane of the microscope objective. This technique enables access to the far-field emission of the sample, to access the angular distribution of the polariton transmission signal. A second lens (f=750 mm) images the far-field emission into the entrance slit of the spectrometer, presented in Sec. 3.2, which is connected to a liquid nitrogen cooled CCD camera. The intermediate image from the sample in both near- and far-field can be accessed by using an additional flip mirror.

For time-resolved measurements the streak camera is used in the time-range with the highest temporal resolution of 2-3 ps. The orientation of the entrance slit with respect to the entrance slit of the spectrometer is rotated by 90 degrees. Typically, the streak camera is used in combination with a short focal length lens to the increase energy density of low intensity signals. Since the intensities from resonant excitation are high enough, a lens with a focal length of $f = 300$ mm is used, to increase the spatial resolution of the k_x far-field emission. Additionally, the lens is mounted on an automated stage for vertical translation, which is used to perform scans along the k_y direction.

The horizontal orientation of the input slit serves as a spatial filter, so that for each measurement of the streak camera (k_x-t) the vertical position of the lens is shifted further in order to acquire the full range of k_y-values. The full set of measurements is reassembled in a way that allows one to observe the full dynamics of the entire Fourier space. This opens up the possibility to analyze the DCP of the polariton pseudospin evolution in time and momentum space [60].

To investigate the evolution of the DCP of the polariton pseudospin, the polarization of the transmission is filtered by using a $\lambda/4$ wave-plate in combination with a Glan-Thompson prism. The temporal evolution of the DCP is calculated according to Eq. (4.8) by integrating the PL intensities from the areas of the scattering ring that correspond to scattering angles of $\theta_s = +45^\circ(-45^\circ)$ for σ^+ and (σ^-) polarized light. This can be used to determine the DCP within these areas for any point in time.

4.2.1 Crosshatching

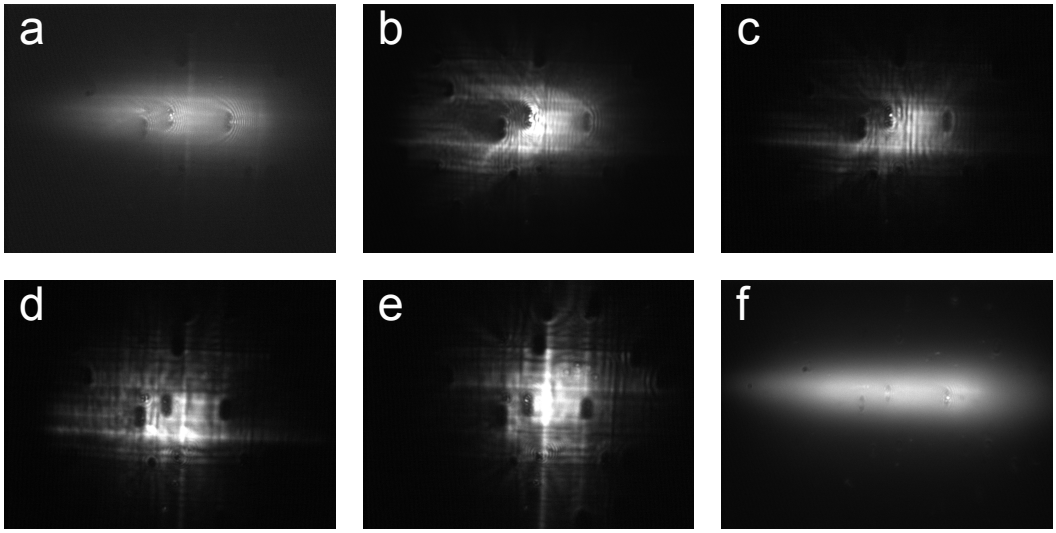

Figure 4.5: Real space image of sample C1575. a)-e): Resonant excitation with decreasing wave vector, starting with the largest wave vector at picture a) and a wave vector close to 0 at picture e). f) same as a), but here at an energy below the LPB, to show so ellipticity of the beam shape.

As an additional source of strain that contributes to the effective magnetic field in terms of an anisotropy, the sample is investigated for signs of crosshatching. Microcavities grown with molecular beam epitaxy with embedded InGaAs QWs might show such a crosshatching as a side effect[61–63]. During the growth process, plastic strain relaxation of the slightly mismatched GaAs/AlAs layers may create an undulating surface morphology. This morphology is characterized by hills and valleys that determine the potential landscape of the polaritons. However, besides causing localization and anisotropy of the sample, crosshatching might also influence the propagation of the polaritons giving rise to resonant Rayleigh scattering [64–66]. Therefore, despite acting as an additional source to the total effective magnetic field, crosshatching can be exploited in order to generate scattering centers for polaritons.

Depending on the wave vector of the resonant excitation, resonant Rayleigh scattering takes place with different magnitudes and hence influences the propagation of the polaritons through the microcavity. A series of measurements of the real space image from the investigated sample for different excitation wave vectors is shown in Fig. 4.5. Starting with the largest wave vector in a),

a wake-like pattern arises behind the strongly localized defects (dark elliptical spots). The polaritons are flowing through the microcavity from the right-hand side and are partially backscattered. This causes self-interference, creating a standing wave pattern. With decreasing wave vector (b) to e)), the polariton luminescence becomes more localized and the wake-like appearance of the polaritons diminishes. The standing wave pattern is also reduced. The wave vector in frame f) is the same as in frame a), but with a slightly detuned energy with respect to the LPB. The excitation energy is below the resonance to show the full ellipticity of the beam spot at the highest possible wave vector.

These findings lead to the conclusion that the sample indeed shows signatures of pronounced crosshatching and also has a large number of strongly localized defect states. In addition, these appear to be extremely well suited for using them in scattering experiments, as a clear influence on the inflow of polaritons can be observed. The surface morphology typical for crosshatching, consisting of hills and valleys, can also be observed for small wave vectors.

4.3 Pseudospin Dynamics and the Optical Spin Hall Effect

In the following, this property of the sample is exploited to generate elastic scattering of polaritons. Since pulsed excitation is applied, the temporal behavior of the polariton DCP of the pseudospin can be examined. In particular, the oscillation of the DCP is investigated. First, the sample is examined for suitable impurities in order to perform resonant Rayleigh scattering of polaritons. Figure 4.6 (a) shows the intermediate image of the real space, where such an impurity can be recognized by the elliptical shadow, close to the center of the image. After polaritons have been injected resonantly under a wave vector of $k_{\parallel} = 0.73\,\mu m^{1}$ at an energy of 1.4606 eV, the typical pattern of a standing wave caused by self-interference appears. It can also be seen, how a part of the polariton flux flows past the defect. An analysis of the far field emission yields information about the momentum distribution of the polaritons.

The intermediate image of the scattering process of the far-field emission is shown in Fig. 4.6 (b). Here, the orange circle highlights the position of the wave vector of the resonant excitation in momentum space. It can be clearly seen how the scattering process redistributes the wave vector along a

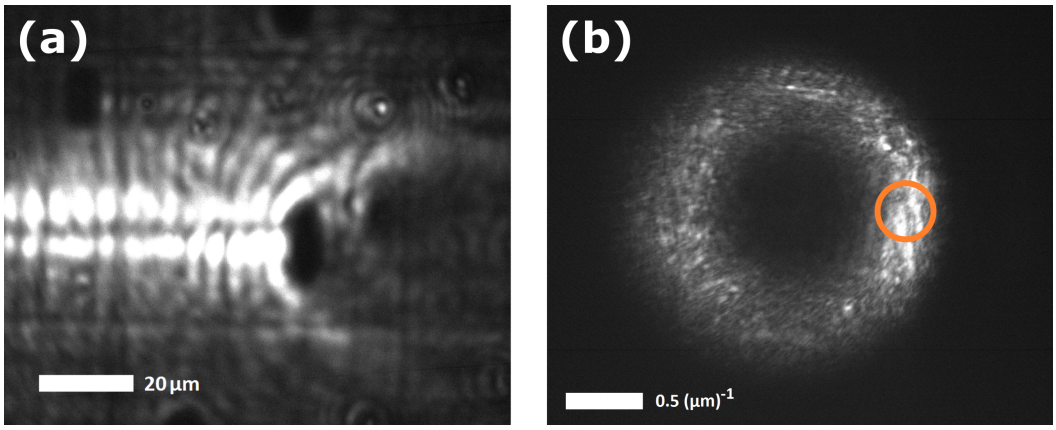

Figure 4.6: Intermediate images of the sample after resonant excitation under non-normal incidence. (a) Real space image of propagating polaritons after resonant excitation with a wave vector of $k_{\parallel} = 0.73\,\mu m^{-1}$. The dark elliptical spot is identified as a localized defect that acts as the center of resonant Rayleigh scattering. b) Far-field image of the sample emission under the same conditions as in a). The orange ring indicates the position of the resonant excitation. Adapted from Ref. [47].

scattering ring. The fact that the absolute value of the wave vector is preserved leads to the conclusion that the scattering process must arise due to resonant Rayleigh scattering. The presence of resonant Rayleigh scattering forms the first important prerequisite in the study of the pseudospin dynamics. In the next step, the entire momentum space is temporally resolved.

Using Eq. (4.8), the momentum-resolved DCP for the time-integrated image in Fig. 4.7(a) is calculated. Here, the typical pattern of the DCP (see Fig. 4.2) for the OSHE can be recognized. Two distinct areas are chosen, in which the DCP is expected to have its maximum (minimum) value for the different circular polarizations σ^+ (σ^-) at scattering angles of $\theta_s = +45°(-45°)$.

The temporal evolution of the DCP within the depicted areas is plotted against time in Fig. 4.7(b). In this figure, three points in time are chosen (t_1-t_3) and plotted in momentum space in order to provide a more accurate picture of the DCP dynamics. These snapshots of the momentum space are shown in Fig. 4.8 and are qualitatively investigated in the following.

The first image at $t_1 = 87\,ps$ shows the moment shortly after the initial excitation. The DCP is mostly negative along the entire scattering ring, which represents the distinct feature of resonant Rayleigh scattering that the polarization of the incoming lightfield is maintained. Although the light

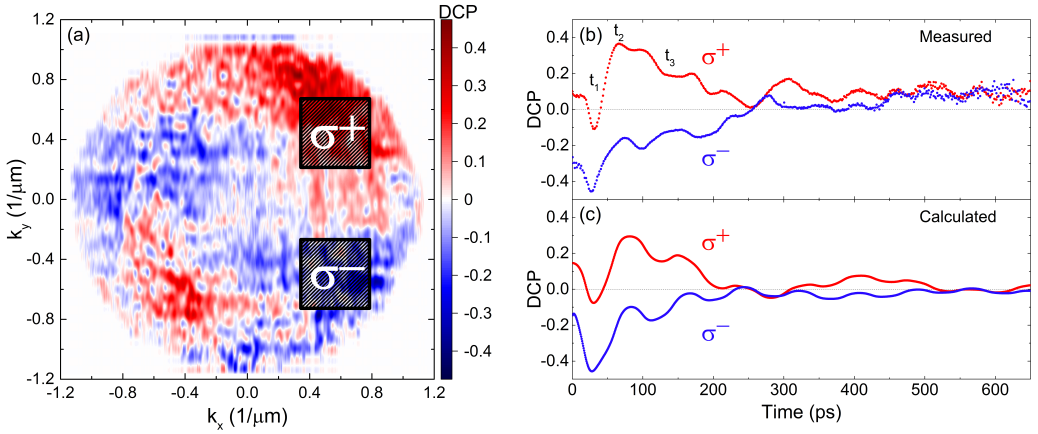

Figure 4.7: Time-resolved measurements of the DCP. a) Far-field image of the time-integrated DCP, after applying Eq. (4.8) to the measured data sets. The areas indicate the positions of which the DCP has been extracted. b) The evolution of the DCP over time acquired from the areas in a) for the different circular polarizations σ^+ and σ^-. DCP at selected times t_i discussed in Fig. 4.8. c) The calculated temporal evolution of DCP using the following parameters for the effective magnetic field: $\hbar\Delta_{\mathrm{LT}} = 18\,\mu\mathrm{eV}$ for the LT-splitting, $\hbar\delta_{\mathrm{an}} = 15\,\mu\mathrm{eV}$ for the anisotropy splitting, and $\hbar\beta = -0.45\,\mathrm{meV}\,\mu\mathrm{m}^2$ for the effective polariton-polariton interaction strength. The polariton lifetime is $\tau = 5\,\mathrm{ps}$ and the scattering time is $\tau_1 = 40\,\mathrm{ps}$ [47].

was nominally linearly polarized, the initial polarization of the light appears to be slightly elliptical. An explanation for this could be the experimental configuration, for example the windows of the cryostat could slightly change the incoming polarization, due to a slight birefringence.

The second snapshot at $t_2 = 129\,\mathrm{ps}$ is deliberately taken at a time when the DCP has reached its maximum positive value. This is characterized by the fact that a large part of the scattering ring is σ^+ polarized and the σ^- polarization falls almost to 0. In addition, it is noticeable that, while the scattering ring is still clearly visible in the first frame, the entire momentum space shows a nonzero DCP. This is mainly caused by the energy loss of the polaritons that is related to continuous scattering processes.

The further temporal evolution is essentially characterized by the fact that the polarizations are slightly mixed by continuous scattering processes over the entire momentum space. However, the standard distribution typical for the OSHE remains more or less unchanged with time, as can be seen in the last figure for $t_3 = 195\,\mathrm{ps}$.

In addition to the pseudospin oscillation predicted in Ref. [43], further oscillations with a higher frequency can be observed. To validate the observed temporal evolution of the DCP, it is calculated using the model from the equations Eq. (4.1) and Eq. (4.2). For a better comparison, the model calculation of the DCP is plotted below the measured temporal evolution of the DCP in Fig. 4.7(c). The parameters for the model are as follows: the LT-splitting is $\hbar\Delta_{\mathrm{LT}} = 18\,\mu\mathrm{eV}$, the anisotropy splitting is $\hbar\delta_{\mathrm{an}} = 15\,\mu\mathrm{eV}$, and the effective polariton-polariton interaction strength is $\hbar\beta = -0.45\,\mathrm{meV}$. The time constants of this process are $\tau = 5\,\mathrm{ps}$ for the polariton lifetime and $\tau_1 = 40\,\mathrm{ps}$ for the scattering time. The slight elliptical polarization of the incoming light is also taken into account for the pseudospin vector with $S_{\boldsymbol{k_0},x}(0) = -0.9$, $S_{\boldsymbol{k_0},y}(0) = (1 - S^2_{\boldsymbol{k_0},x})^{-1/2}$, and $S_{\boldsymbol{k_0},z}(0) = 0$.

The time-resolved measurements and the theoretical model exhibit a high degree of agreement, which can be used to determine the two oscillation frequencies that occur. The slow oscillation with a period of about 300 ps occurs due to the precession of the pseudospin around the effective magnetic field. The period is proportional to the wave vector $\boldsymbol{k}_{\parallel}$. The fast oscillation frequency with a period of about 70-80 ps is caused by a mismatch of the oscillation frequencies between the pumped and the scattered state due to the nonlinear polariton-polariton interaction [47].

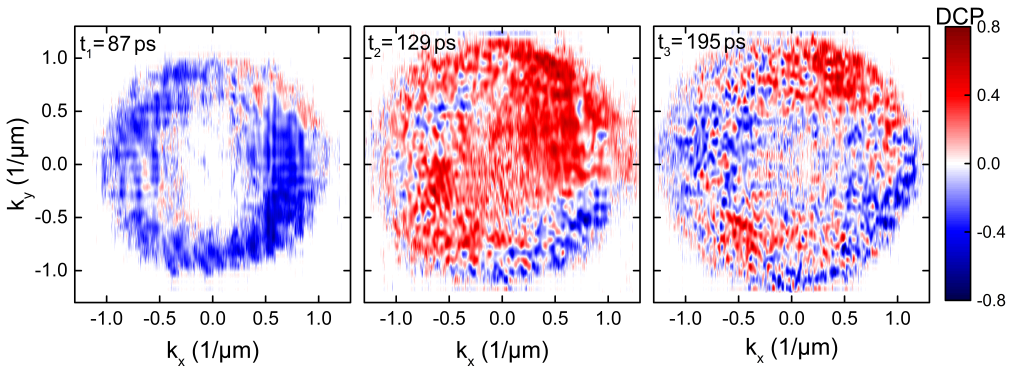

Figure 4.8: Far-field image of the DCP. Snapshots of the DCP for selected points in time corresponding to the time indices t_i in Fig. 4.7(b). Adapted from cite [47]

4.4 Conclusion

It has been shown that a flux of polaritons injected resonantly under a non-zero wave vector may leads to scattering processes with sample defects. In addition, it could be shown that these scattering processes must be resonant Rayleigh scattering, since the scattering process preserves both the energy and the initial polarization. Resonant Rayleigh scattering produces a uniform distribution of the polariton momentum along a ring in the momentum space whose size corresponds to the wave vector of the initial excitation.

Polarization-resolved measurements of the temporal evolution of the DCP show the predicted oscillating behavior, which, however, surprisingly also show the presence of a further oscillation. An extension of the model for the effective magnetic field from Ref. [43], which takes into account the anisotropy of the sample and the nonlinear polariton-polariton interaction seems to be in a good agreement with the experimental data. The nonlinear interactions result in self-induced Larmor precession, meaning that the polariton pseudospin precesses around the resulting effective magnetic field, which might explain the additional oscillation frequency of the DCP.

Chapter 5

Perturbation of Polaritons in an Annular Optical Potential Trap

In this chapter, the influence of a background reservoir on an existing polariton condensate is studied. The polariton condensate is generated by an annular optical potential which also serves as an optical trap. In previous investigations of different groups, it could already be shown that a polariton condensate forms within the trap in a Gaussian mode, insofar as the radius of the annular potential is on the order of the polariton propagation length [67]. In addition, other groups have shown theoretically that polaritons can only undergo a real Bose-like phase transition in the presence of a confining potential [68]. This scenario could be realized experimentally by inducing strain in a sample in order to generate a confining potential by Balili et al. [17]. The properties of a polariton condensate that is confined in a trap of any kind are therefore well understood.

Due to the strong localization of the confined condensate, it is possible to perform experiments that probe the influence of a reservoir of background charge carriers on the condensate by optically injecting a background reservoir directly into the trap using non-resonant excitation. We employ spatially as well as time- and energy-resolved studies to investigate the resulting impact of the reservoir on the condensate. After the arrival of a laser pulse, the observed spectrum shows an additional peak at higher energy, which we attribute to polaritons propagating away ballistically from the non-resonantly induced reservoir. By varying the power of the non-resonant pulsed excitation, the temporal response of the system is investigated.

5.1 Experimental Details

The investigated sample contains a high Q cavity with a Q-factor of approximately Q = 20000. The DBR structure consists of 32 (36) upper (lower) alternating $Al_{0.2}Ga_{0.8}As$/AlAs layers. The cavity contains four QWs placed in the central antinodes of the confined $\lambda/2$ cavity mode with a Rabi splitting of $2g_0 = 9.5\,\text{meV}$. To provide a high mobility of the polaritons, the detuning has been chosen as $\delta = -14\,\text{meV}$. The sample is mounted on the cold finger of a continuous helium flow cryostat. A temperature controller ensures a constant sample temperature of 12 K.

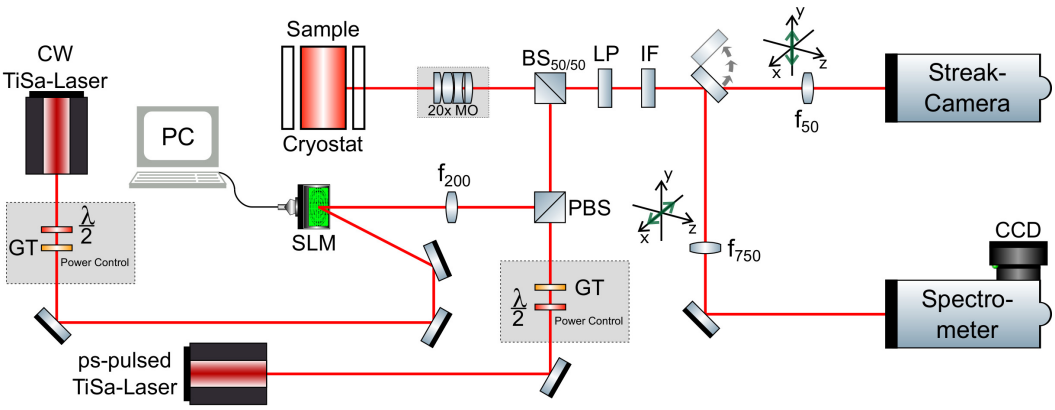

Figure 5.1: Schematic layout of the setup for the investigation of the perturbation of trapped polaritons. GT, Glan-Thompson prism. SLM, spatial light modulator. MO, microscope objective. LP, longpass filter. IF, interference filter. BS/PBS, beam-splitter/polarizing beam-splitter. f_x, lens with focal length of x. CCD camera, charged-coupled device camera.

For non-resonant excitation two different laser systems are used. The schematic representation of the experiment is shown in Fig. 5.1. A CW laser with a wavelength of $\lambda_{CW} = 739.38\,\text{nm}$ creates a steady-state population of polaritons using an annular pattern. The annular pattern is created with a spatial light modulator, that spatially modulates the phase of the incoming Gaussian beam. The in-house software of the company HOLOEYE converts an intensity pattern with the desired excitation pattern into its Fourier transform. The software also offers the possibility of overlaying the phase pattern with that of a Fresnel lens. By adding an additional f=200 mm lens behind the SLM, the size of the beam can be adjusted to fit to the input aperture of the microscope objective. This configuration acts as a telescope with an enlarged and collimated beam that has the desired annular shape in the focal plane. The resulting excitation

pattern is shown in Fig. 5.2. The ring has a diameter of approximately 10 μm.

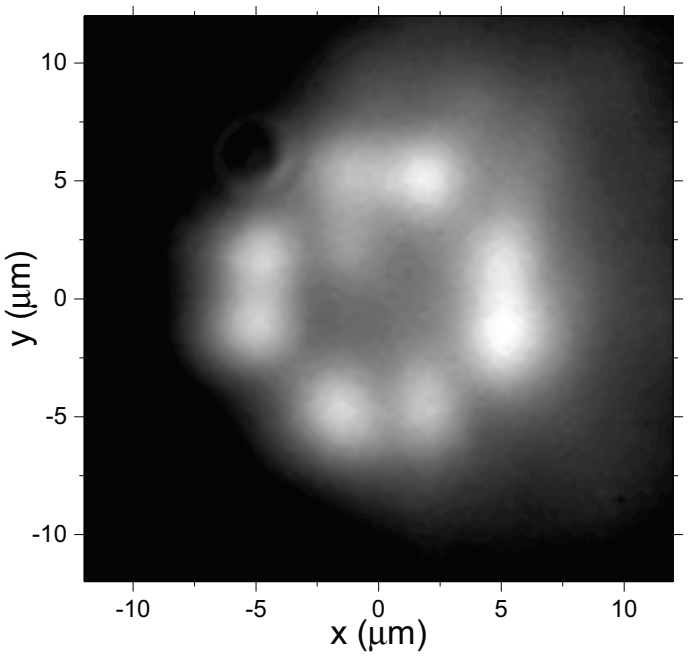

Figure 5.2: Grayscale image of the annular CW excitation pattern in real space. The pattern is created using the SLM.

A polarizing beam splitter merges the CW laser with an additional picosecond pulsed laser for non-resonant pulsed excitation. The pulsed laser with a wavelength of $\lambda_{\text{pulse}} = 737.87\,\text{nm}$ and a repetition rate of $\nu_{\text{pulse}} = 75.4\,\text{MHz}$ is adjusted to excite the region in the center of the annular trap. The diameter of the Gaussian laser spot is approximately 5 μm. The non-resonant pulses create a cloud of excitons that act as a repulsive potential and that may simultaneously act as a gain medium for the condensate.

Both lasers are focused on the sample with a 20x magnification microscope objective that is arranged in confocal geometry. A longpass filter rejects the excitation wavelengths that are reflected by the sample surface. An interference filter of 1 nm width, tuned to the center of the emitted wavelengths of polaritons in the ground state (i.e. at $k_{\parallel} = 0$), is placed behind the longpass filter. Additional lenses complete the setup by focusing the signal into the entrance slits of both detectors presented in Sec. 3.2.

For time-resolved measurements a f = 50 mm lens focuses the signal to the entrance slit of the Hamamatsu streak camera. The focusing lens is mounted on a translation stage to scan vertically along the real space. This enables the possibility to capture the full polariton dynamics in 2D real space on the picosecond time scale.

The signal may also be send to the monochromator for spectrally resolved measurements of the PL. Here, a grating with a resolution of 1200 lines/mm is used. The monochromator can also be used to record the real space image, if the grating is set to zero order. This is useful to localize the emission coming from the sample as well as to control the shape of the CW excitation pattern (see. Fig. 5.2)

5.2 Results

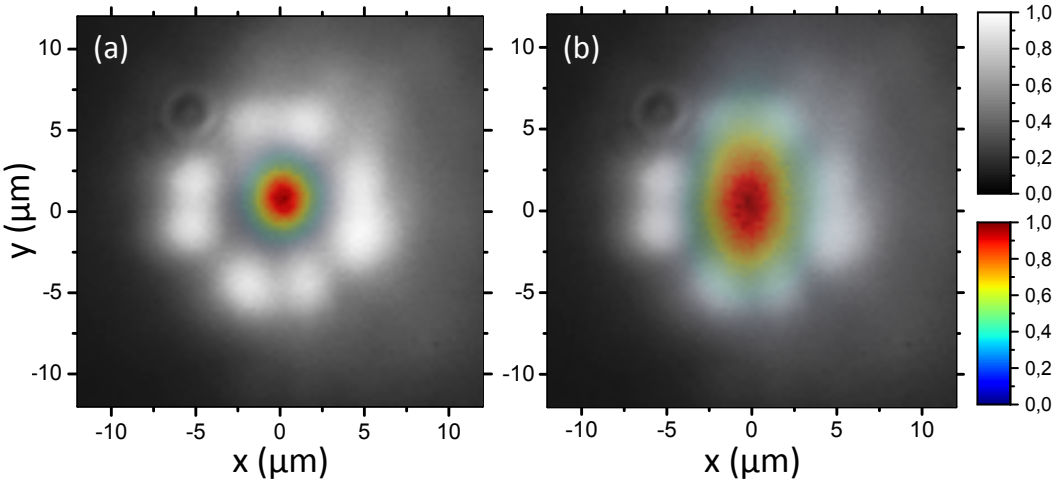

Figure 5.3: Real space images of the emission from the sample. In both pictures, the annular excitation pattern of the CW laser is shown in grayscale. The images using different color scales were recorded separately and placed on top of each other. (a): The polariton condensate, which is formed in the optical trap when the threshold power of the CW laser is exceeded, is shown in color. (b): The excitation spot of the pulsed laser is also shown in color. The spot is placed in the center of the optical trap.

An image of the real space emission for CW excitation above the polariton condensation threshold (see Fig. 5.3(a)) shows the appearance of a polariton condensate in the center of the optical trap. The PL of the sample emission is

spectrally filtered around the energy minimum using an interference filter (see Fig. 5.5). The energy minimum also corresponds to the range of the lowest polariton momenta, which illustrates the efficiency of the trapping mechanism. The position of the Gaussian laser spot of the pulsed excitation is shown in Fig. 5.3(b). This choice of position ensures that the center of the trap matches the laser spot position of the pulsed excitation beam.

For both types of excitation, input-output (IO) measurements are performed to determine the threshold powers at which polariton condensation occurs. The resulting measurements are shown in Fig. 5.4. For pulsed excitation, polariton condensation occurs at a power of $P_{\mathrm{THR,pulse}} = 2.4\,\mathrm{mW}$. For CW excitation using the annular potential, polariton condensation occurs at a power of $P_{\mathrm{THR,CW}} = 10.4\,\mathrm{mW}$. The difference between these powers arises mainly due to the size of the excitation spot, but is partially also caused by the higher peak energy density of the pulsed excitation. In contrast to the IO curve using pulsed excitation, there was no observable saturation behavior for the IO curve using CW excitation. This may also be a consequence of the size of the excitation spot, which results in limited power densities that can be achieved using CW excitation.

For a closer investigation of the interaction between the CW pumped polariton condensate and the reservoir generated by non-resonant pulsed excitation within the trap, the spectrum of the polariton emission originating from in the central region of the trap is recorded. The power of the pulsed excitation is chosen such that it is below the condensation threshold at a power of $P_{\mathrm{pulse}} = 0.9\,P_{\mathrm{THR,pulse}}$. The resulting spectrum is shown in Fig. 5.5.

Pure CW excitation with a power of $P_{\mathrm{CW}} = 1.9\,P_{\mathrm{THR,CW}}$ results in a large peak at an energy of $E = 1.6026\,\mathrm{eV}$, which we define as the ground state. A slightly smaller peak at an energy of $E = 1.6032\,\mathrm{eV}$ might arise due to the part of the condensate that propagates away from the optical excitation potential rather than into the trap.

With additional pulsed excitation, a further peak emerges at an energy of $E = 1.6036\,\mathrm{eV}$, in addition to the peak in the ground state, which in the following is referred to as the high-energy peak. One possible explanation for the occurrence of this high-energy peak is that the polariton dispersion is blueshifted locally after the pulsed excitation due to the repulsive interaction with the induced reservoir. This leads to an increase of the potential within the trap, allowing a part of the CW polariton condensate present to propagate

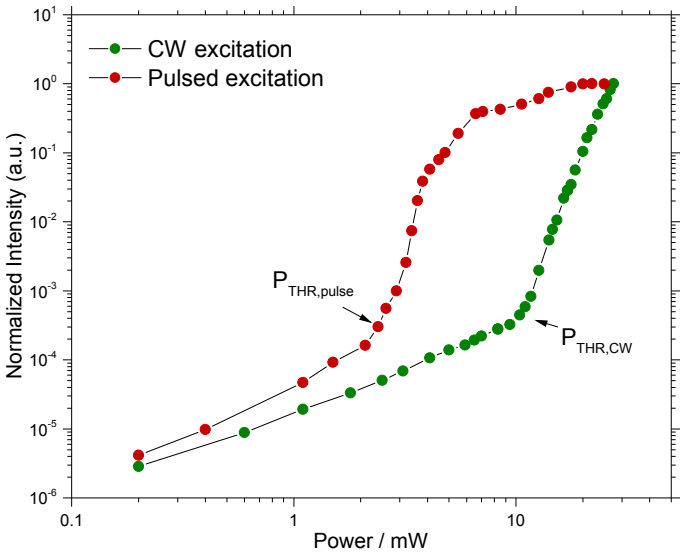

Figure 5.4: Measurements of the polariton condensation threshold power in a double logarithmic graph. The IO curve for the annular excitation pattern used for the CW laser is shown in green. The IO curve of the Gaussian spot used for pulsed excitation is shown in red. The powers of the condensation thresholds are $P_{\mathrm{THR,pulse}} = 2.4\,\mathrm{mW}$ for the pulsed laser and $P_{\mathrm{THR,CW}} = 10.4\,\mathrm{mW}$ for the CW laser.

out of the trap. This process is time-dependent strongly related to the lifetime of the existing reservoir. The formation dynamics of the high-energy peak and the question whether it coexists with the ground state cannot be investigated solely based on this data as the recorded spectrum is integrated over time and a large number of pulses.

For this reason, the spatially resolved dynamics of this process within the trap are examined below using a streak camera. The interference filter is again centered on the energy of the ground state so that the high-energy peak can be filtered out mostly. The emission of the CW pumped polariton condensate is positioned at the center of the entrance slit of the streak camera. The resulting time-resolved measurements for different pulsed excitation powers and at a constant CW power of $P_{\mathrm{CW}} = 2.7\,P_{\mathrm{THR,CW}}$ are shown in Fig. 5.6.

Since the slit of the streak camera is oriented horizontally, the real space image is spatially filtered along the x coordinate. The first thing to notice is that the increase in intensity after the arrival of the pulse at $t = 0$ is slightly shifted towards the negative x-direction. This is a consequence of the fact that the

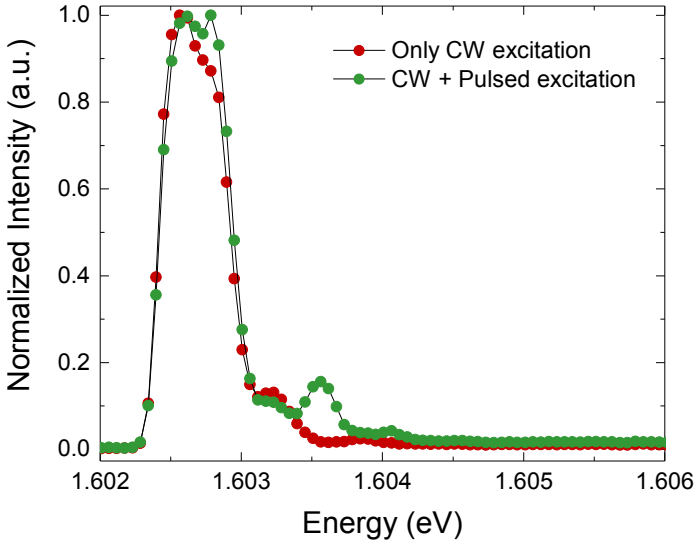

Figure 5.5: Spectrally resolved emission of the polariton condensate when excited only by the CW laser and with additional pulsed excitation. The combined excitation spectrum shows a high-energy mode in the spectrum. The excitation powers are $P_{\mathrm{CW}} = 1.9\,P_{\mathrm{THR,CW}}$ and $P_{\mathrm{pulse}} = 0.9\,P_{\mathrm{THR,pulse}}$, respectively.

laser spot of the pulsed excitation is slightly shifted sideways with respect to the average position of the CW polariton condensate within the trap.

At a low pulsed excitation power of $P_{\mathrm{pulse}} = 0.3\,P_{\mathrm{THR,pulse}}$, the measured intensity increases after the arrival of the pulse. This increase still exists for higher pulsed excitation powers, but the intensity is initially reduced, with the long-lived signal occurring at a later point in time. At a pulsed excitation power close to the condensation threshold for pulsed excitation, this reduction in intensity is particularly noticeable. For pulsed excitation powers above the condensation threshold, there is also a short-lived, but very distinct peak shortly after the arrival of the pulse and of which the intensity grows with the pulsed excitation power. This is probably a consequence of the spectral broadening of the high-energy peak as well as fast scattering of the created carriers to the condensate or possible transition into the weak coupling regime.

A more detailed analysis of the temporal behavior is shown in Fig. 5.7(a). Here, the profiles of the images are extracted from Fig. 5.6 and can thus be subjected to a more precise analysis. The main focus is on the long-lived

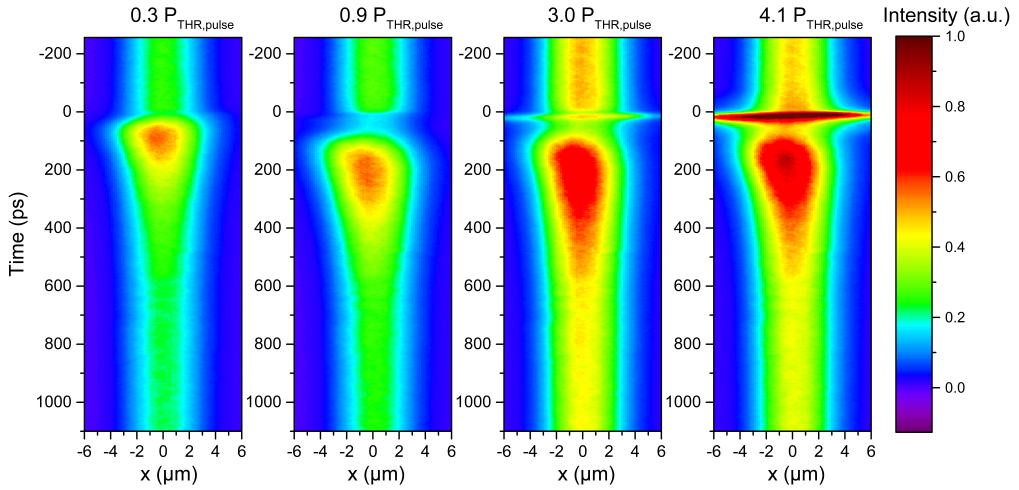

Figure 5.6: Time-resolved images of the center of the trap for pulsed excitation into the trapped polariton condensate, for various pulsed excitation powers and constant CW excitation power. The interference filter is set to the spectral position of the lowest energy mode. After the arrival of the pulse, a long-lived signal is occurs.

process that occurs after pulsed excitation, which, interestingly, exceeds the typical lifetime of polaritons in microcavities of several ps considerably. For a more accurate quantitative assessment of the long-lived signal, the 85% and the 15% decay times of the signal are evaluated. This analysis is performed for a variety of pulsed excitation powers and is shown in Fig. 5.7(b).

Here, it is noticeable that up to the threshold pulsed excitation power, the peak of the long-lived intensity decay gradually shifts to later times. However, regardless of the pulsed excitation power applied, the average lifetime of the long-lived signal of $\Delta t = 283\,\mathrm{ps} \pm 11\,\mathrm{ps}$ remains approximately the same. The lifetime of the condensed polaritons present in this sample, amounts to approximately 10 ps and is thus far shorter than the observed duration of the long-lived signal.

A possible explanation for the long-lived signal is the presence of slow relaxation processes within the reservoir towards states, from which stimulated scattering towards the condensate becomes possible. Accordingly, this experiment could be used to investigate the condensation process under non-resonant CW excitation in more detail. However, the exact microscopic mechanism leading to the formation of this long-lived signal is still unclear.

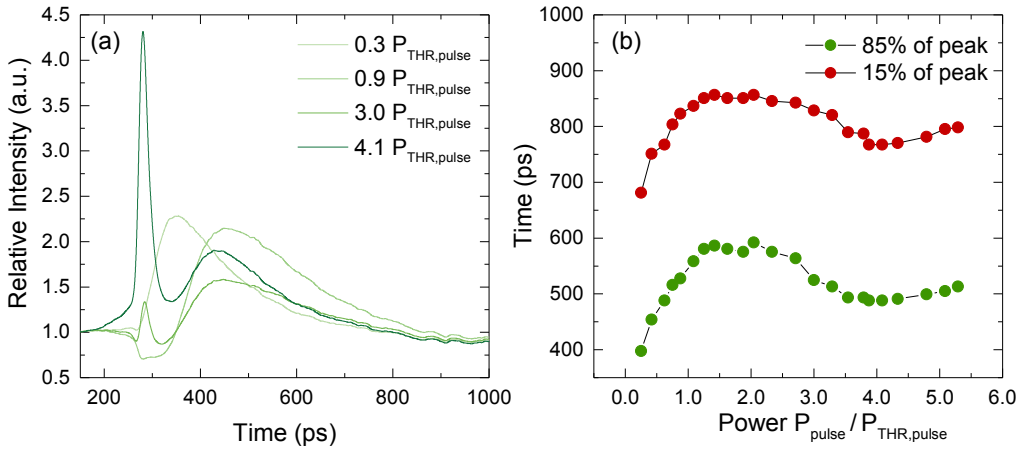

Figure 5.7: Analysis of the long-lived signal. (a): Profiles extracted from the streak camera measurements of the power series in Fig. 5.6. The relative intensity shown here, is the intensity of the emission normalized to the intensity of the CW signal present in the absence of pulsed excitation. (b): Decay time of the long-lived signal for different pulsed excitation powers. Shown here are the points in time at which the intensity of the long-lived signal has reached 85% and 15% of the maximum intensity respectively.

The investigation of the spatially resolved temporal behavior of this process offers another possibility to analyze the relaxation mechanism qualitatively. The same method as presented in chapter 4 is applied and a lens, mounted on a translation stage, is used to record the temporal development of the emission along the vertical spatial direction. Here, however, the real space and not the Fourier space is mapped.

In Fig. 5.8(a), the resulting temporal profile extracted from the streak camera measurement with a pulsed excitation power of $P_{\mathrm{pulse}} = 1.1 P_{\mathrm{THR,pulse}}$ just above the condensation threshold is shown. The center of the polariton condensate emission is adjusted centrally to the slit of the streak camera. The interference filter is still adjusted to the energy of the ground state. The initial decrease of the signal after the arrival of the pulse is again present. Subsequently, the signal rises again and the long-lived process becomes observable.

To illustrate the temporal evolution of this process in real space, three significant points in time along the signal are highlighted in Fig. 5.8(a) and correspond to the real space images shown in Fig. 5.9. The time-integrated image of the polariton condensate excited by the CW laser before the arrival of the pulse is shown in Fig. 5.8(b). The normalized intensity from this graph

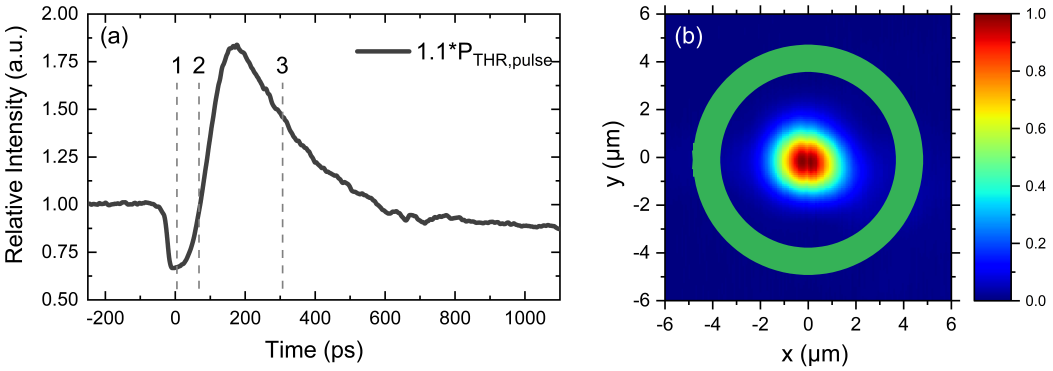

Figure 5.8: (a): Profile extracted from the streak camera measurement at an applied pulsed excitation power of $P_{\text{pulse}} = 1.1P_{\text{THR,pulse}}$ at vertical position of y = 0. Different points in time are highlighted which correspond to the spatial images in Fig. 5.9. (b): Time-integrated emission of the polariton condensate for CW excitation, spectrally filtered at the lowest energy. The annular potential is symbolically shown in green.

is used as a reference for the three graphs in Fig. 5.9, i.e. the normalized intensity is subtracted from the respective intensities of the graphs in Fig. 5.9 and thus results in the relative intensity difference ΔI.

At time frame 1, 5 ps after the pulsed excitation, the minimum relative intensity of the temporal signal in Fig. 5.8(a) is reached. Graph 1 in Fig. 5.9 clearly shows that the relative intensity difference at the location of the polariton condensate is completely negative. This is a consequence of the fact that the background charge carrier reservoir, injected by pulsed excitation, exerts a repulsive interaction on the condensate. Furthermore, this observation also agrees with the assumption that the reservoir locally causes a blueshift of the potential and that the trap mechanism becomes ineffective. As a consequence of the spatial redistribution of the polaritons, the nonlinear process of the stimulated scattering of the polaritons into the condensate no longer takes place.

At time frame 2, 70 ps after the pulsed excitation, the intensity of the signal is approximately back to the initial level (see Fig. 5.8(a)). In real space, this is represented by a roughly equal portion of positive and negative intensity differences ΔI. Here, it can also be seen how the trap is replenished from the negative x-direction. This agrees with the assumption that the laser spot of the pulsed excitation is not positioned exactly at the center of the trap.

At time frame 3, 310 ps after pulsed excitation, the relative intensity difference ΔI is entirely positive. The signal is located completely on the inside of the trap and has the original shape of the spatial intensity distribution from Fig. 5.8(b). Accordingly, it can be assumed that the reservoir has decayed at least to the extent that the potential of the trap is no longer exceeded and the mechanism of the trap is thus effective again, giving rise to stimulated polariton scattering towards the polariton condensate.

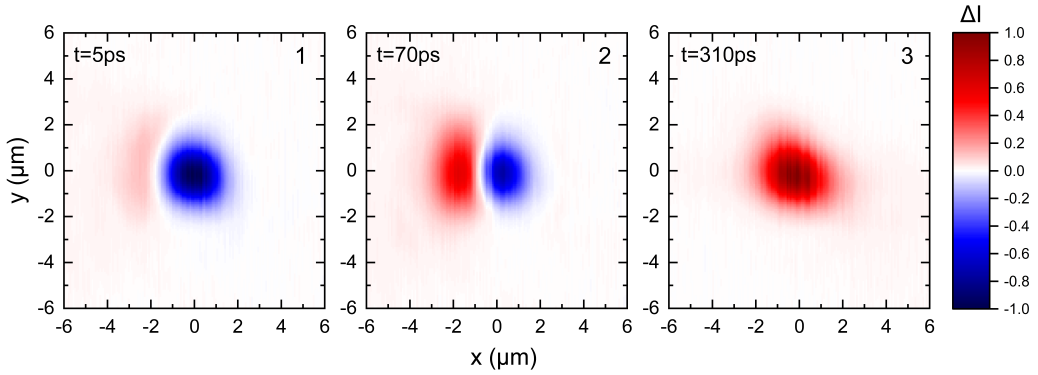

Figure 5.9: The change of the relative intensity difference ΔI in real space following the pulsed excitation, corresponding to the different times highlighted in Fig. 5.8. Blue corresponds to a negative and red to a positive change of the relative intensity difference.

5.3 Conclusion

In conclusion, it could be shown that the annular optical excitation potential is suitable to generate a polariton condensate and to localize it within the trap. This has already been successfully demonstrated in Ref. [67] and allows the formation of a polariton condensate spatially separated from the excitation spot.

By adding pulsed excitation located within the trap potential, it could also be shown that a reservoir injected into the trap inhibits the trap mechanism and spatially redistributes the polariton condensate. Since the condensation of polaritons is a nonlinear process that strongly depends on polariton density, the spatial redistribution of polaritons leads to a less effective stimulated scattering. With the decay of the reservoir, the trap mechanism becomes efficient again and a CW pumped polariton condensate forms within the trap.

By temporally resolving this process, a long-lived signal of $\Delta t = 283\,\mathrm{ps} \pm 11\,\mathrm{ps}$ is observable, which shows a lifetime independent of the power of the pulsed excitation.

This experiment only allows insights into the repulsive nature of the interaction between the polariton condensate and the non-resonantly pumped reservoir of background charge carriers. The assumption that this interaction is repulsive is consistent with the results for the real space images in Fig. 5.9. However, no final statement can be made about the microscopic dynamics of the reservoir.

Chapter 6

Tracking Dark Excitons Optically Using Polariton Bistability

In the past few decades, optical spectroscopy has been used as a powerful tool to gain insights into the fundamental properties of polaritons in semiconductors. Specifically, it has been used to discover effects such as Bose-Einstein condensation [16, 17, 69], superfluidity [70–72], or quantized vortices[73], only to name a few. However, these effects rely on optical transitions that are bright, i.e. optical transitions that are allowed by selection rules. Elementary excitations within semiconductors also include dark states, which are largely inaccessible with the use of conventional optical spectroscopy. These excitations include states with an exciton spin projection of $J_z = \pm 2$, which are forbidden by selection rules. Also, nominally bright excitons ($J_z = \pm 1$), with a wave vector that exceeds that of the light in the medium, cannot couple to the light field and are therefore optically dark. A deeper understanding of the properties of dark excitons, particularly in microcavities, might open up the possibility of their targeted use in future experiments due to their mutual interaction with polaritons.

In this chapter, an optical technique is presented that opens up the possibility to measure the lifetime of dark excitons utilizing microcavity polaritons in the bistable regime. After introducing the concept of optical bistability in the first part of this chapter, a method that characterizes the optical bistability of microcavity polaritons is presented. Here, the transmission is measured in dependence of the input power of the energetically ultra-narrow CW laser, presented in Sec. 3.1, for various detunings between the CW laser energy and the ground state energy of the LPB.

In the second part of this chapter, the technique used to modify the transmission curve is presented. A train of a few non-resonant fs pulses generates charge carriers at the position where the population of bistable polaritons is located.

This introduces a certain time dependence, since the charge carriers generate a time-varying blueshift of the LPB. The time-resolved change in the transmission is measured and yields access to processes that take place on the ns time scale. In order to reveal the nature of these long-lived processes, power-dependent measurements are carried out to investigate the influence of the exciton density on the temporal behavior of the dark reservoir.

Unless otherwise stated, the results and arguments presented in this chapter are based on the publication of Schmidt et al. in Ref. [74].

6.1 Optical Bistability of Microcavity Polaritons

Optical bistability is a fundamental property of microcavity polaritons occurring in resonant excitation experiments and is one of the processes relying on nonlinear interactions between polaritons. Nonlinear processes originate from the excitonic component of polaritons which may cause polaritons to scatter off of each other. A classical example of such a scattering process is stimulated parametric scattering towards signal and idler states along the polariton dispersion. It has been shown that stimulated parametric scattering allows 100-fold amplification of a resonant probe pulse at normal incidence when the dispersion is additionally pumped resonantly at an angle [75].

Resonant excitation provides a massive occupation of polariton states, which may yield a renormalization of the polariton dispersion. The renormalization takes place in the form of a blueshift of the dispersion. The blueshift strongly depends on the interaction strength of the polaritons which can be quantified by α_1 and α_2 for polaritons with the same or opposite spin, respectively. The absolute value of α_1 is positive, resulting in a repulsive interaction of polaritons with the same spin, causing a blueshift of the polariton energy. For the interaction of polaritons with opposite spin, the interaction is usually attractive which results in a redshift of the polariton energy. This attractive interaction corresponds to a negative value of α_2 [76]. However, the magnitude of both interaction strengths differs significantly, where $\alpha_1 > \alpha_2$, which makes an overall blueshift of the polariton energy more favorable [77].

The finite linewidth of the lower polariton branch in combination with the density dependent blueshift allows polaritons to be generated quasi-resonantly. Here, the CW laser introduced in Sec. 3.1 is used and the energy of the laser is set slightly above the energy of the ground state of the LPB. The small

overlap between the two modes allows the injection of polaritons under normal incidence. The power of the laser is continuously increased which leads to a slight increase of the measured relative transmission. The relative transmission increases because of the growing overlap between both modes, due to the increasing blueshift of the LBP. At a certain threshold power a drastic increase of transmission occurs after the system switches to the so-called on state. If the pumping power is reduced again, the system remains in the on state even after it has fallen below the threshold power required to switch on the system. The shape of the transmission curve corresponds to a hysteresis loop that separates the two stable states from each other and is accordingly referred to as the bistable region.

This forms the basis of optically driven bistability, since there is a certain range of powers for which two stable states of the system exist. A typical polariton bistability curve is shown in Fig. 6.1. Inside of the hysteresis loop the dashed line indicates the region of instability [78].

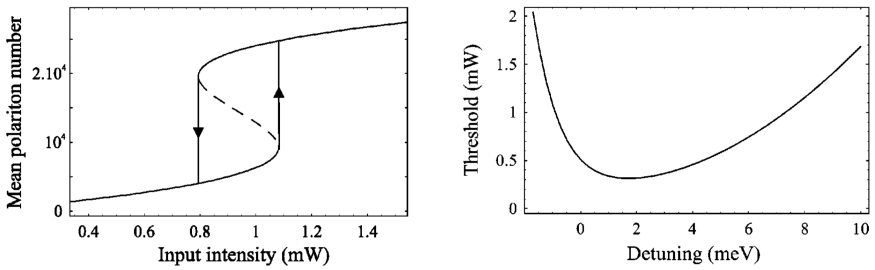

Figure 6.1: Left: Bistability curve observed in the intensity of a given polariton field amplitude against the input power. The arrows show the cycle of the hysteresis loop, where the dashed line indicates the region of instability. Right: The upper threshold power of the pump laser for different exciton and cavity photon detunings [78].

The frequency detuning

$$\delta_p = \omega_p - \frac{E_{\mathrm{LP}}(k_\parallel = 0)}{\hbar} \tag{6.1}$$

between the CW laser frequency ω_p and the polariton resonance E_{LP} at $\vec{k}_\parallel = 0$ needs to exceed a certain threshold in order to obtain optical bistability. This threshold strongly depends on the linewidth Γ_p of the polariton resonance [78]:

$$\delta_p < -\sqrt{3}\Gamma_p \tag{6.2}$$

and therefore on the properties of the investigated sample.

6.1.1 Experimental Details

The sample investigated corresponds to the sample for transmission measurements presented in Chapter 4.2. However, for this experiment, a detuning between the exciton and the cavity mode of 1.8 meV is chosen. This leads to a slightly more excitonic composition of the polaritons, making them more massive and thus more localized inside the quantum well.

The experimental setup used to detect optical bistabiltiy follows the basic concept of the configuration shown in Fig. 4.3. Instead of using a pulsed laser, the transmission experiment is performed using the ultra-narrow CW laser presented in Sec. 3.1. A f=100 mm lens focuses the beam to a spot diameter of about 40 μm, but has a very narrow distribution in k-space. This is important since a broad distribution in k-space would results in a constant overlap of the laser and LPB mode and thus in permanent resonant excitation.

Since no temporal resolution is required to measure the presence of bistability, the streak camera is replaced by a photodiode that measures the intensity of transmission through the sample. To estimate the polariton linewidth Fourier imaging techniques are used to measure the far field emission of the non-resonantly excited polariton dispersion below the condensation threshold using the Acton spectrometer, presented in Sec. 3.1. The full scheme of the setup is shown in Sec. 6.2.1.

6.1.2 Generation of Optical Bistability

In Fig. 6.2 the dispersion of the LPB is shown as well as the extracted profile of the polariton linewidth at low momentum which yields $\Gamma_p \approx 170\,\mu$eV. The dispersion is obtained by exciting the sample with 8 short non-resonant pulses with a wavelength of 737 nm and a duration of ≈ 100 fs. The power of the non-resonant excitation excitation is 140 μW with a spot size of about 75 μm. Taking Eq. (6.2) and the extracted polariton linewidth Γ_p into account, no optical bistability should be possible below a frequency detuning energy of:

$$\delta_p < 287\,\mu\text{eV}. \tag{6.3}$$

In order to confirm the validity of Eq. (6.2), various bistability measurements

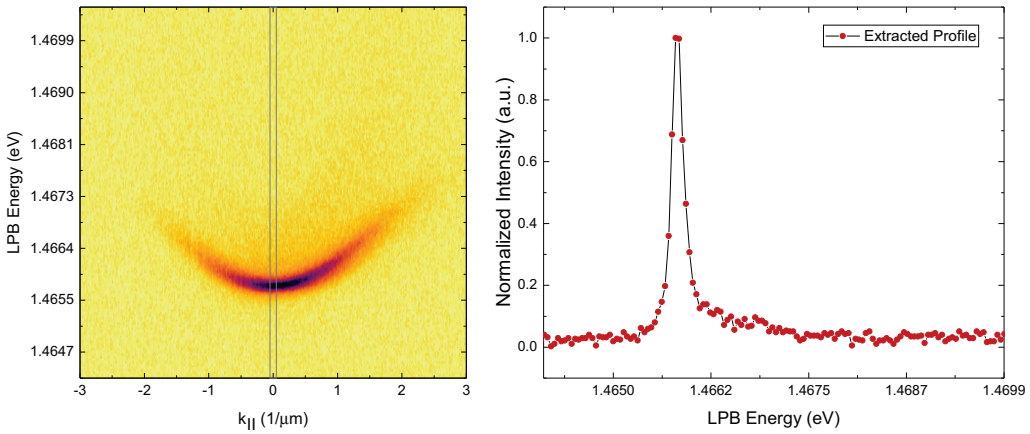

Figure 6.2: Extraction of polariton linewidth Γ_p. Left: Dispersion of the lower polariton branch obtained using non-resonant pulsed excitation. Right: The integrated profile extracted from the vertical area shown in the left figure, used to calculate the polariton linewidth $\Gamma_p \approx 170\,\mu$eV.

for different frequency detunings δ_p are shown in Fig. 6.3. Here, the width of the region of bistability is referred to as hysteresis width ΔP, which is obtained from the difference of both threshold powers, where the state of the system changes

$$\Delta \mathrm{P} = P_{\mathrm{On}} - P_{\mathrm{Off}}. \tag{6.4}$$

The green shaded area indicates the frequency detuning area where no bistability should be obtainable, as given by Eq.(6.3). The hysteresis width of first data point is zero which is in agreement with the prediction of Eq. (6.2). For every further data point, the system shows optical bistability is achieved. For two detunings, we observe a very large hysteresis width of up to $\Delta P = 120\,$mW, indicating more complex interactions between the polariton and pumping mode. However, in between these two very large hysteresis widths, the width never falls below a value of approximately $\Delta P = 40\,$mW.

A typical measurement of the hysteresis loop is shown in the inset of Fig. 6.3. The hysteresis width is $\Delta P = 44\,$mW and the frequency detuning δ_p is about $650\,\mu$eV. The green and red arrows indicate the direction of the measurement loop. The green dots are used for the loop of increasing power and the red dots for the loop of decreasing power, respectively. Starting at low pumping powers, the system stays in the off state up to the first threshold power that appears at approximately $\mathrm{P}_{\mathrm{On}} = 177\,$mW. The system remains stable in the on state

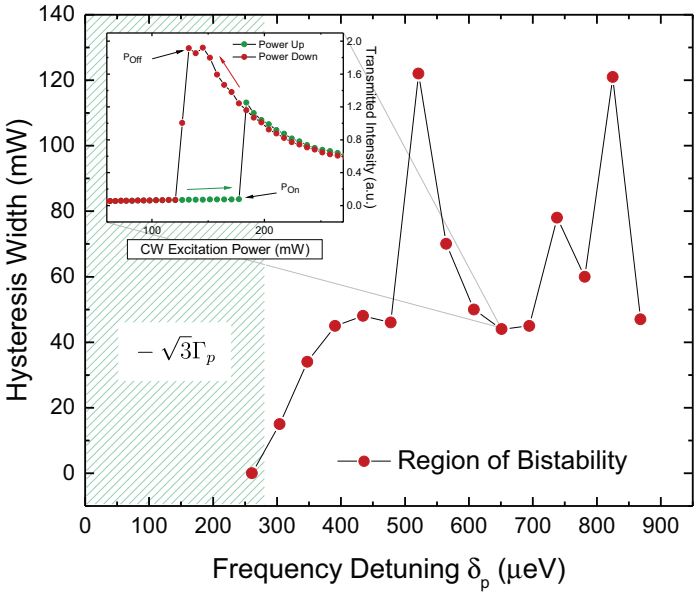

Figure 6.3: Map of hysteresis widths for different detunings δ_p. The green shaded area indicates the region where no bistability should occur. A typical measurement of the pumping power loop is shown in the inset, in which a hysteresis between both stable states of the system is clearly visible.

until the end of the loop of increasing power. The red dots in the inset of Fig. 6.3 indicate the loop of decreasing power, in which the system still remains in the on state. During the reduction of the power, the first threshold power is undercut. While decreasing the power, the relative transmission increases continuously. At a power of $P_{\mathrm{Off}} = 133\,\mathrm{mW}$ the system switches back to the off state. The system remains in this state until the end of the loop.

Compared to similar experiments, this result shows a rather different shape of the transmission curve[79–81]. The cause for this peculiar the shape of the transmission is reproduced using a model of five coupled rate equations in the exciton- photon basis $\chi_{\uparrow,\downarrow}$ and $\Phi_{\uparrow,\downarrow}$, which take into account the different spin

polarizations [82]

$$i\frac{d}{dt}\chi_{\uparrow,\downarrow} = \frac{\Omega_R}{2}\Phi_{\uparrow,\downarrow} + [\Omega_X - \frac{i}{2}(\gamma_X + \beta|\chi_{\uparrow,\downarrow}|^2) + g_R n_R + \alpha_1|\chi_{\uparrow,\downarrow}|^2 + \alpha_2|\chi_{\uparrow,\downarrow}|^2]\chi_{\uparrow,\downarrow}, \tag{6.5}$$

$$i\frac{d}{dt}\Phi_{\uparrow,\downarrow} = \frac{\Omega_R}{2}\chi_{\uparrow,\downarrow} + (\Omega_C - \frac{i}{2}\gamma_C)\Phi_{\uparrow,\downarrow} + \frac{\Omega_{\text{lin}}}{2}\Phi_{\uparrow,\downarrow} + P_{\uparrow,\downarrow}, \tag{6.6}$$

$$\frac{d}{dt}n_R = 2\beta|\chi_\uparrow|^2|\chi_\downarrow|^2 - \gamma_R n_R + P_R. \tag{6.7}$$

Since the polariton-polariton interaction strength strongly depends on the spin polarization, these polarizations are taken into account within the two fields $\Phi_{\uparrow,\downarrow}$ and $\chi_{\uparrow,\downarrow}$ of the photons and excitons, respectively. The strength of the coupling of both fields is given by the Rabi frequency Ω_R. The quasi-resonant CW laser pumps the photonic modes with the rate $P_{\uparrow,\downarrow}$. The energy of the CW laser is used as the reference energy for the energies $\hbar\Omega_C$ and $\hbar\Omega_X$ of the bare cavity and exciton mode, respectively. The decay rates of these two modes are governed by γ_C and γ_X. The occupation number n_R represents a reservoir of dark excitations and has two contributions. First, two excitons with opposite spins form biexcitons with the formation rate β. This process is especially efficient at positive detunings, where the polariton mode is close to the biexcitonic resonance. The CW pumping creates a steady-state characterized by an equilibrium between formation and decay of biexcitons. During non-resonant excitation a cloud of hot electron and hole pairs is created. These pairs relax at a rate P_R and contribute to the reservoir of dark excitations, which decays with a rate of γ_R. It should be mentioned that the last contribution to the reservoir in Eq. (6.7) does not explain the shape of the transmission curve, since it is only relevant for non-resonant excitation. It is mentioned for the sake of completeness, as this case will be discussed later on. The interaction strength of excitons with the reservoir of dark excitations is given by the average over the polariton interaction strength for both polarizations $g_R = (\alpha_1 + \alpha_2)/2$, since the spin degree of freedom of the dark reservoir is not taken into account. Ω_{lin} is introduced to the model as a measure of the linear polarization splitting of the cavity modes. The splitting of the linear polarizations strongly depends on the strain within the sample, which is inevitably caused by the attachment of the sample to the cryostat in transmission geometry, as well as by the usage of materials with mismatched lattice constants during the molecular beam epitaxy growth of the microcavity.

A realistic simulation of the experiment therefore requires all locally varying strain induced linear polarization splittings within the microcavity to be considered. For this purpose, values of up to 250 μeV are assumed for the splitting of the linear polarizations. In Fig. 6.4 the transmission, which is given by the photonic component of the polaritons, is calculated and averaged over several realizations of the strain landscape, for CW excitation with small polarization degree of 0.08. By averaging over all values for Ω_{lin} the abrupt

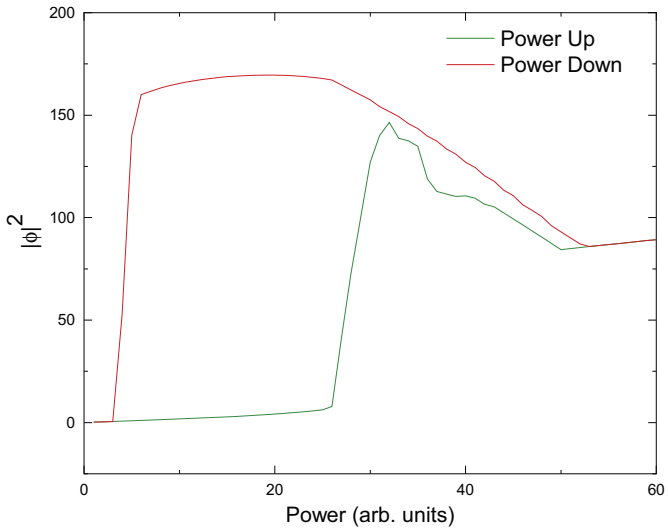

Figure 6.4: Simulation of the photonic component of the polariton wave function. Here, the transmission is averaged over a broad distribution of strain induced linear polarization splittings.

decrease of the relative transmission becomes a rather gentle decrease. This is caused by varying shifts of the upper bistability threshold and by spin multistability, depending on the splitting of linear polarizations [82]. The gentle increase of transmission during the reduction of power is in good agreement with the experimental data from the inset in Fig. 6.3.

The results show a clear bistable behavior of the polaritonic system above the bistability condition given in Eq. (6.2). Moreover, by introducing a complex model that also considers spinor interactions of the polaritons, good agreement with the experimental shape of the transmission curve is found. The decrease in relative transmission as the power is increased, depends on whether both possible spin polarizations of the polaritons have already reached the upper bistability threshold or not [82]. The differences of the upper

bistability threshold are mainly caused by a strain induced splitting of the linear polarization modes of the polaritons.

In the following section, a bistable state is investigated for different powers within the hysteresis. The time-resolved response of the relative transmission to a perturbation introduced by a train of non-resonant pumped pulses is observed.

6.2 Tracking Dark Excitons with Bistable Polaritons

Non-resonant pulses generate a cloud of additional carriers which can occur in all permitted states discussed in Sec. 2.2. All of these carriers will induce a blueshift of the polariton mode [81–83], but instead of creating a steady-state scenario, the pulsed excitation opens up the possibility for time-resolved measurements. Time-resolved measurements of the relative transmission allow us to determine the lifetime of the carriers present, by utilizing their influence on the blueshift of the polariton mode. The blueshift reduces the overlap between CW and polariton mode and thus influences the intensity of the relative transmission. The analysis of the relative transmission reveals a surprisingly long lifetime of a dark reservoir of more than 20 ns. Taking into account the permitted relaxation mechanisms of these carriers, assumptions can be made which might explain the origin of the long-lived reservoir.

6.2.1 Experimental Details

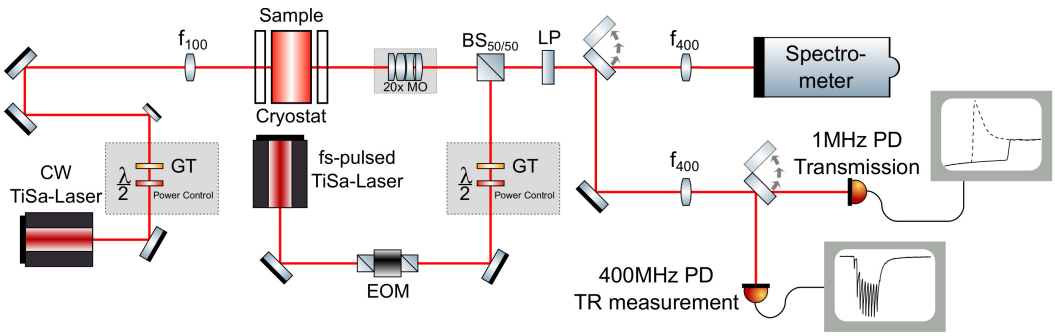

Figure 6.5: Scheme of the experimental setup.

The experimental scheme is shown in Fig. 6.5. We excite the sample using the CW laser in transmission geometry. The power-dependent measurement of the relative transmission is performed with a photodiode that has a bandwidth of 1 MHz. Non-resonant pulsed excitation generates the charge carriers necessary for the time-dependent repulsive potential. The non-resonant wavelength is centered around the fourth Bragg minimum at 737 nm. In order to investigate processes over a very long period of time, the time interval between the respective pulses must be extended. This is done by using the EOM, which is controlled by a delay generator that generates 1 MHz gate pulses. The gate pulses are about 100 ns long, which corresponds to about seven to eight pulses that still have a time separation of 13.3 ns.

In order to adjust the CW and the pulsed laser independently, the pulsed laser is applied to the sample in reflection geometry. In order to pump the central region of the polariton reservoir only, the train of pulses is focused down to about double the spot size of the CW laser which yields a spot diameter of 75 μm using a 20x microscope objective. A $\lambda = 750$ nm longpass filters out the residual light of the non-resonant pulsed laser beam. After the 1 MHz bandwidth photodiode has been used to ensure that the system is in the upper branch of the bistability curve, by measuring the transmission intensity from the sample, the signal is redirected to a very fast 400 MHz bandwidth photodiode by means of a flip mirror. Since this photodiode has a very fast response time of 1 ns, it is suitable for high-resolution, time-resolved measurements.

In order to ensure that the system stays within the strong coupling regime during the non-resonant excitation, the far-field emission is investigated using the spectrometer. A power series clearly shows the transition to the weak coupling regime at very high pumping intensities.

6.2.2 Transition from Strong to Weak Coupling

As mentioned in Sec. 2.5, non-resonant excitation may lead to polariton condensation, which is a state of spontaneous coherence that is associated with the massive occupation of the ground state. In the following, the present sample will be examined for the possibility to create such a condensate. For this purpose, the non-resonant power of the pulsed laser is successively increased, while the far field of the sample emission is recorded by the spectrometer.

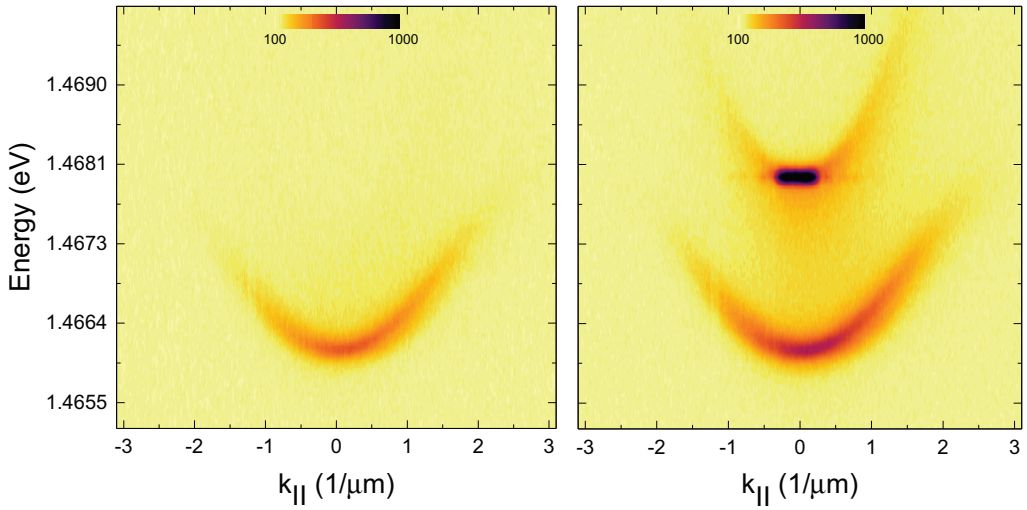

Figure 6.6: Far-field emission of the sample for two different non-resonant pumping powers. On the left side, the sample is pumped rather weakly with about 175 pJ/pulse. The PL from the LPB is clearly visible, indicating that the strong coupling regime is present. On the right side, the system is pumped with larger power of about 413 pJ/pulse. Here, an additional mode of high intensity appears close to the spectral position of the bare cavity mode. This indicates the loss of strong coupling and marks the transition into the weak coupling regime. Adapted from Ref. [74].

In Fig. 6.6, the far-field emission measurements for two different powers are shown. On the left side, the sample is pumped weakly with an energy of 175 pJ/pulse. Only the photoluminescence of the LPB can be seen, indicating that the system is still within the strong coupling regime. However, at this pumping power, there is no observable evidence of condensation. On the right side of Fig. 6.6, the sample is pumped with a much higher power of 413 pJ/pulse. Here, a clearly recognizable additional mode above the LPB appears, which can be identified as the bare cavity mode. This indicates that the system already transits into the weak coupling regime.

In Fig. 6.7 the full set of power dependent measurements is shown. During this set of measurements, no condensation of the polaritons is observed. Instead, a clear transition from the strong to the weak coupling regime is visible. A quantitative analysis of the region around the higher energy cavity mode around $k_{\parallel} = 0$ can be seen in Fig. 6.7. The intensity within the shaded area of the inset in this figure is integrated and plotted for all of the applied powers. The integrated intensity shows a clear nonlinear increase starting at a power

of about 350 pJ/pulse, which is referred to as the threshold power for the transition to the weak coupling regime.

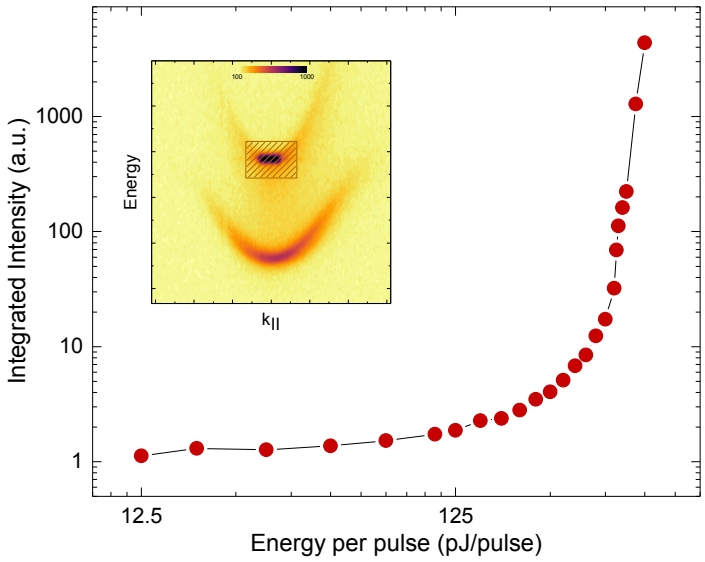

Figure 6.7: Double logarithmic plot of the integrated intensity of the cavity mode that corresponds to the highlighted shaded area of the inset in dependence of the applied non-resonant pumping power [74].

The transition from the strong to the weak coupling regime may occur when the linewidth of excitons at large k-vectors increases in the order of the normal mode splitting of the coupled exciton-photon mode [84]. However, the main reason for this transition is the loss of the polariton modes as eigenstates of the system. From Eq. (2.27) we conclude that the loss rate of cavity photons γ_{cav} and excitons γ_{exc} exceeds the energy exchange rate g_0 between them, giving rise to the weak coupling regime.

Since the exciton density is strongly associated with the applied non-resonant pumping power, the exciton-photon coupling strength $\hbar g_0$ is weakened by the interaction with the free carriers. At such high densities, the formation of excitons may also be completely suppressed, due to phase space filling [85]. This ultimately leads to the transition into the weak coupling regime of uncoupled bare cavity and bare exciton modes.

The purpose of this measurement is to ensure that the system is well within the strong coupling regime during non-resonant excitation. In the following

section, this information is considered in order to select the range of powers to be used in the follow-up experiments.

6.3 Adding the Dark Reservoir

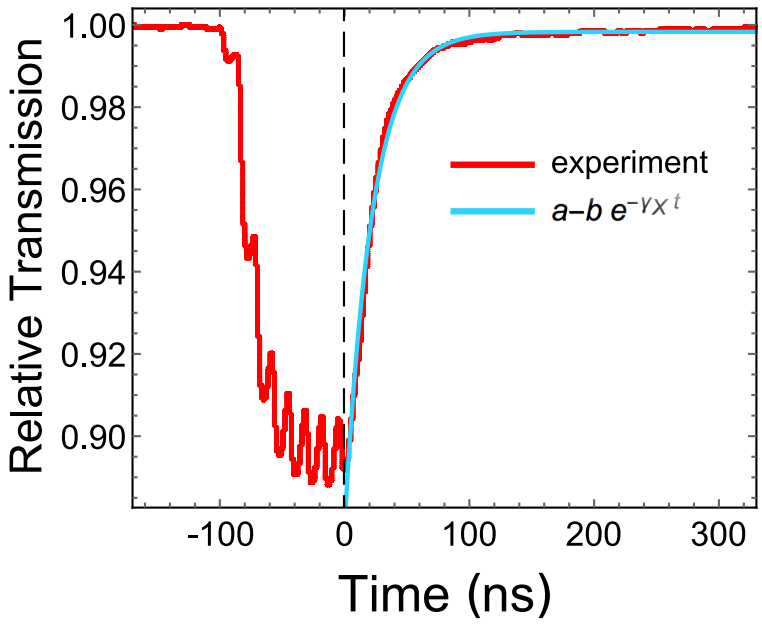

Figure 6.8: Typical shape of the relative transmission after the arrival of seven non-resonant pulses. The blue line corresponds to the exponential fit function given by Eq. (6.8). Adapted from the supplemental material of [74].

In Fig. 6.8, a typical result for the relative transmission after the non-resonant excitation of 7 consecutive 100 fs pulses is shown. The time axis can be divided into three sections. The first section begins at about -200 ns and goes up to -100 ns. This section marks the steady-state scenario without any additional carriers present. Moreover, the relative transmission in this section serves as a reference for the steady-state regime transmission. The second section begins at -100 ns and goes up to 0 ns, indicating duration of the opened gate. In this section, the train of non-resonant pulses excites additional carriers in the proximity of the polaritons already present. The last section begins at 0 ns which is marked by the dashed line which also corresponds to the time when the gate closes. This section is used to determine the lifetime of the long-lived

carriers present, for which a simple exponential fit following:

$$f(t) = a - be^{-\gamma_X t} \tag{6.8}$$

is used.

Starting in the second time period in Fig. 6.8, a clear accumulation of a reservoir n_R of optically inactive carriers is observable. This is characterized by the minimum of the relative transmission approaching a saturation value, while the gate is opened. The contribution of bright excitons and free electrons and holes to the dark reservoir are neglected. Thus an immediate pumping of the dark reservoir n_R can be assumed. After each pulse, the reservoir relaxes and a short increase of the relative transmission can be seen. This process is interrupted by each following pulse. The total relaxation of the reservoir can be observed after the arrival of the last pulse. The rather simple solution of rate Eq. (6.7) results in a mono-exponential decay of the reservoir

$$n_R = n_0 e^{\gamma_X t}, \tag{6.9}$$

for $\beta \to 0$. The increase of the relative transmission can be fitted to this solution. In Fig. 6.8 this fit is shown for t>0, i.e. after the closing of the gate. As input parameters for the model (6.8) $a \approx 0.998$ and $b \approx 0.12$ are assumed. The fit yields a decay rate of $\gamma_X = 45.16\,\mu\text{s}^{-1}$ for the dark reservoir which translates to a lifetime of $1/\gamma_X = \tau_X = 22.15\,\text{ns}$.

There are different possible explanations for the origin of such a long-lived reservoir of dark carriers and the associated blueshift of the polariton energy. In addition, the long time scale makes it possible to exclude many possibilities from the outset. These include parity-forbidden and spatially indirect excitons, which have a significantly shorter lifetime due to their weak interaction with bright states [86]. In microcavities containing more than one quantum well, it is also possible to form antisymmetric polariton states with a spin of $J_z = \pm 1$. The coupling of these states to leaky cavity modes leads to a drastic reduction of their lifetime below values of 1 ns, which is essentially shorter than the observed 22 ns [87]. Also, biexcitons can be excluded as their lifetime is expected to be one order of magnitude shorter [82].

By simply looking at the time scales on which these processes occur, some typical decay channels can already be excluded. Taking into account further possible decay channels, which are considered to be responsible for the long-lived dark reservoir, only two possible candidates remain. In the following, these candidates will be discussed in detail.

6.4 The Origin of the Dark Reservoir

In order to clarify the origin of the long-lived dark reservoir, two different species of dark excitons, which may occur during non-resonant pulsed excitation, are analyzed. On the one hand, dark dipole-transition forbidden spin $J_z = \pm 2$ excitons may occur during non-resonant excitation, which have already been introduced in Sec. 2.2. For a radiative decay of these excitons, the spin must be changed first by non-radiative interactions such as exciton-phonon scattering or spin dephasing. On the other hand, dipole-transition allowed spin $J_z = \pm 1$ excitons may be generated at a large wave vector that can not couple to the light field inside of the cavity, because these wave vectors lie outside of the light cone. This applies to all wave vectors that satisfy the equation

$$|\vec{k}_{\parallel}| > \frac{2\pi}{\lambda} n_c \tag{6.10}$$

and therefore, have a larger wave vector than that of the light inside the cavity. It can be assumed that both species of dark excitons exist after non-resonant excitation. However, the relaxation of the two exciton species is based on different effects, that are supposed to strongly depend on the exciton density present. By further experiments that include the exciton density dependence, the true nature of the dark reservoir might be found.

After the arrival of a short non-resonant pulse, electrons and holes form large momentum ($\vec{k}_{\parallel} > 0$) bright and dark exciton states on the picosecond time scale via interactions with phonons. At large momentum, theses excitons are completely decoupled from the cavity field, leading to a more or less flat dispersion at large k. This results in a dispersion of the bright and dark exciton states that is rather similar to the dispersion of these states in bare quantum wells. Moreover, due to the exciton exchange interaction energy ζ, the bare bright and dark exciton states are split by an energy of approximately $\zeta = 80\,\mu$eV [88], with the dark state being the lower energy state. The rather small energetic splitting causes a mixing of these states, leading to a fast spin relaxation time of about 80 ps for bare quantum wells.

Spin relaxation mechanisms of charge carriers in semiconductors are well known to occur for different causes such as the intrinsic symmetry properties of the crystal, the spin-orbit, or the exchange interaction [89–91]. However, due to momentum relaxation towards the ground state $\vec{k}_{\parallel} = 0$, the Maialle mechanism usually becomes the dominant spin relaxation mechanism [92]. It

arises because of an additional longitudinal-transverse splitting of the bright exciton states having non-zero in-plane and out-of-plane wave vectors [46].

The strong coupling shifts the bright exciton state to lower energies by half of the Rabi energy at $\vec{k}_{\parallel} = 0$. Since the spin relaxation time strongly depends on the value of the splitting between the bright and dark states, it is expected to be drastically increased. Moreover, because of the large value of the Rabi splitting, the lifetime of dark excitons at $\vec{k}_{\parallel} = 0$ should also be largely enhanced. The relaxation of these states will be mostly phonon mediated towards the bottleneck region at higher k. There, these states are able to mix with the bright states again which enables the coupling to cavity photons, form polaritons and decay radiatively. However, as this relaxation channel only occurs due to phonon interaction, no significant exciton density dependence is expected. This is in stark contrast to the dominant relaxation channel of the nominal bright polaritons at large wave vectors. For them, the most important relaxation channel is exciton-exciton scattering, due to momentum relaxation into the light cone towards the low momentum regime. Therefore, a strong dependence of the lifetime of these excitons on the density of excitons is anticipated.

The density of excitons strongly depends on the applied non-resonant pulsed excitation power. In order to investigate the influence of the exciton density, the temporal response of the relative transmission is analyzed after the arrival of a train of non-resonant pulses for various pumping powers. We focus on the temporal response on the one hand and the maximum magnitude of the suppression of the relative transmission on the other hand. This series of measurements is shown in Fig. 6.9.

While the gate (indicated by the two vertical lines) is opened, the train of non-resonant pulses generates the typical decrease of the relative transmission, that has already been observed in Fig. 6.8. However, a clear connection between the applied power and the decrease of the relative transmission is identified. A decrease of the relative transmission of up to 85% of its initial value is observed. A quantitative analysis of the suppression of the relative transmission as a function of power is plotted in the inset of Fig. 6.9. The suppression of the relative transmission approaches saturation for high powers, which has been already observed.

This saturation behavior is primarily related to the renormalization of the exciton resonance. As the pulse power increases, the resonance of the exciton

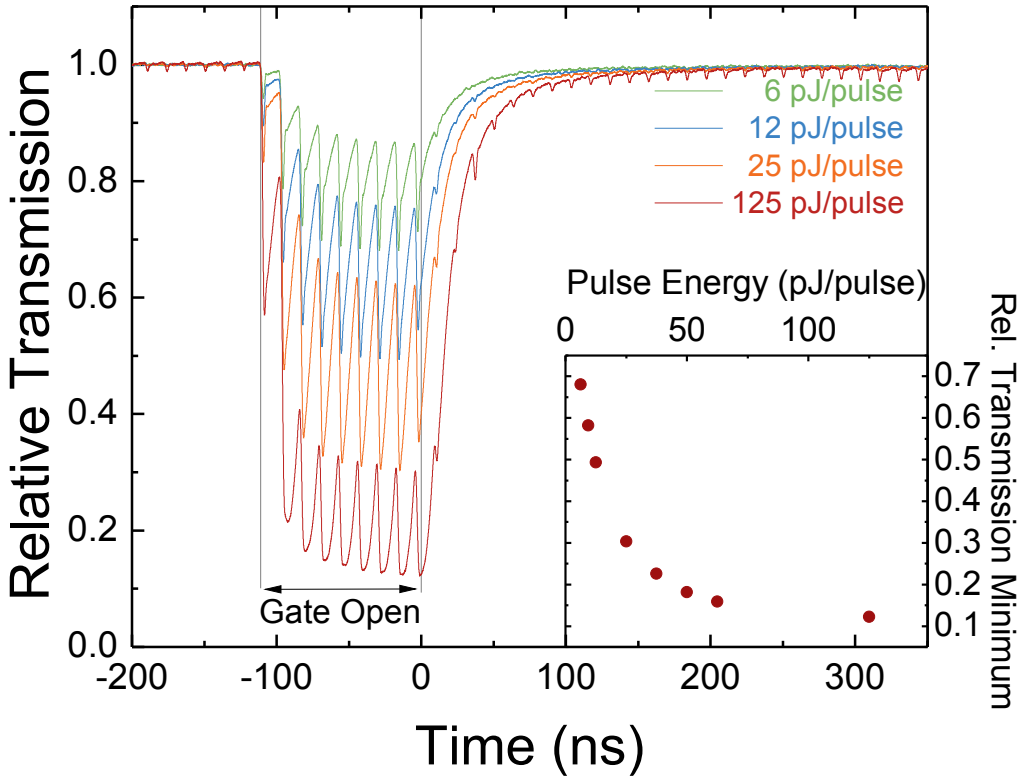

Figure 6.9: Investigation of the temporal response after the arrival of a train of pulses for various non-resonant pumping powers. The time of the gate opening is indicated by the two vertical lines. In the inset, the value for the maximum suppression of the transmission is plotted against the applied non-resonant pumping power [74]

and thus the entire lower polariton branch is shifted to higher energies. This reduces the overlap between the CW and polariton mode with increasing pulse power. The shape of the curve in the inset in Fig. 6.9 can thus be explained by the line shape of the polariton mode.

As evidence for the repulsive nature of the interaction, which provides the blueshift of the polariton mode, the relative transmission for different CW pumping powers along the hysteresis curve is investigated. Figure 6.10 shows that for a CW pumping power below the upper bistability threshold, the repulsive nature of the dark reservoir is blueshifting the polariton dispersion by which the relative transmission can be significantly increased. Interestingly, after the arrival of the last pulse, on overall enhancement of the relative

transmission occurs. This can be attributed to the very slow relaxation of the dark reservoir and the associated slow redshift of the polariton mode towards the CW pump resonance. For CW pumping powers above the upper bistability threshold, the system can be switched on by the train of non-resonant pulses. Moreover, the typical response of the relative transmission as well the typical time scale of the relaxation is observed.

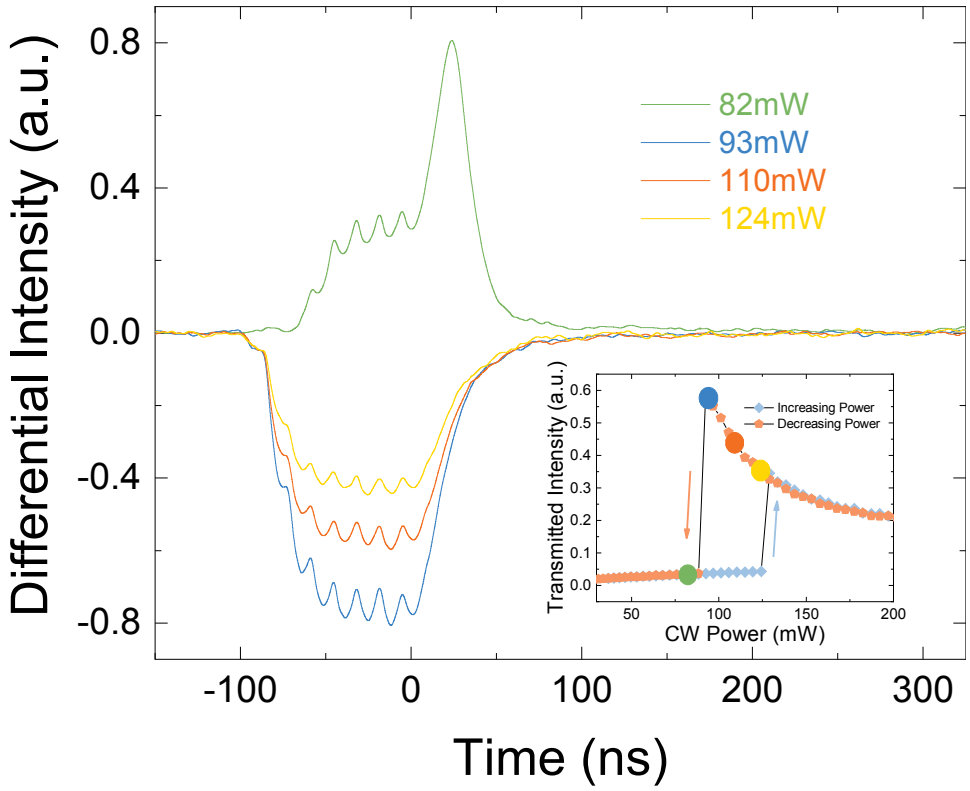

Figure 6.10: Time-resolved measurements of the relative transmission for different CW pumping powers along the hysteresis power loop. This loop is shown in the inset, in which the color for any of the applied powers correspond to the color of the transmission curve. The pulsed excitation power is remained constant and below the threshold power for the transition into the weak coupling regime. Adapted from the supplemental material of Ref. [74].

Since the non-resonant pumping power does not have an influence on the time scale of the relative transmission response behavior, the dependence of the lifetime of the dark reservoir on the exciton density can be excluded. Consequently, it is reasonable to assume that the reservoir consists essentially

of optically inactive excitons with a spin of $J_z = \pm 2$ close to $k_{\parallel} = 0$.

6.5 Conclusion

In conclusion, it could be shown that the system can be brought into an optically bistable state and kept stable using an ultra-narrow CW laser. In addition, the bistability condition from equation (6.2) could be confirmed. The system is driven in the upper state of the bistability region and used as a sensitive probe for the presence of a dark reservoir that is introduced using a train of non-resonant pulses. By performing power dependent measurements of the non-resonant pump, the threshold intensity of the transition from the strong to the weak coupling regime has been determined. This ensures that the system is driven in the strong coupling regime.

The methodology presented provides an insight into the otherwise hidden nature of the dynamics of dark excitons. Time-resolved measurements of the relative transmission confirm a surprisingly long lifetime of a dark reservoir of more than 22 ns. In the search for the composition of the dark reservoir, some constituents could be excluded by the fact that their lifetime must be well below the observed very long lifetime. Further investigations allow the conclusion that the dark reservoir most likely consists of spin-prohibited low-momentum dark excitons around $\vec{k}_{\parallel} = 0$. Additional experiments also confirm that the interaction between the dark reservoir and polaritons is of repulsive nature. This discovery contains interesting implications that could potentially be used for further experiments.

Due to their repulsive nature, dark excitons can be utilized and optically imprinted as a long-lived potential landscape for polaritons. Optically imprinting potential landscapes requires two photon absorption processes to overcome the selection rules in single photon experiments that normally prevent the resonant injection of dark carriers [93–95]. Using these processes, it is possible to resonantly excite the dark exciton reservoir without influencing the relaxation dynamics of polaritons.

Finally, it can be shown that when conventional laser systems with a pulse separation of 13 ns are used, the dark reservoir accumulates over several pulses. This discovery is in complete contrast to the current assumption that the system is completely empty before the next pulse arrives. This is of specific

importance for the condensation dynamics of polaritons, because of the non-negligible influence of the dark exciton reservoir.

Chapter 7

Summary

In summary, the main results presented in this thesis provide further insights into certain properties of polaritons in microcavities. These include the dynamics of the polariton pseudospin coupled to an effective magnetic field within a microcavity, the polariton condensation process within an annular optical trap potential, and the interaction of a polariton condensate with a reservoir of charge carriers. Furthermore, the interaction between polaritons and the reservoir can also be used to obtain information about the dynamics of the reservoir and thus to estimate the lifetime of the reservoir. The results presented in Chapters 4-6 provide a deeper understanding of the above processes and mechanisms that can ultimately be considered in the design of an analogue Hamilton simulator by taking into account the actual properties of the elements and the interactions between them.

The results from Chapter 4 show that the pseudospin of propagating polaritons within a microcavity couples to an effective magnetic field arising due to the polarization properties of the structure through which the polaritons move, as well as by the mutual interactions of the polaritons themselves. The coupling of the pseudospin to the effective magnetic field leads to a spatial separation of the polaritons depending on their spin, in other words to a spin polarization of the polaritons depending on the direction of their momenta. The theoretically predicted oscillation of the degree of circular polarization can not only be confirmed, but also the model for the description of the effective magnetic field and thus the pseudospin dynamics could be extended with the help of the experimental results.

Since this result is important for polaritons with finite momenta, in Chapter 5 the influence of a reservoir of background charge carriers on a polariton condensate is examined. The polariton condensate is formed spatially separated

from the excitation laser by an annular excitation potential. Subsequently, non-resonantly pumped charge carriers were generated by pulsed optical excitation within the trap. The added carriers disable the trap mechanism and above the condensation threshold of the pulsed excitation laser, stimulated polariton scattering is reduced by a spatial redistribution of the polariton condensate within the trap. As the reservoir decays, the trap mechanism as well as stimulated scattering becomes effective again and slow relaxation processes lead to renewed polariton condensation within the optical trap. Time-resolved measurements allow us to make quantitative statements about the temporal scales on which this process takes place and to make qualitative statements about the repulsive interaction between a reservoir of background charge carriers and an optically trapped polariton condensate. Ultimately, however, only the passive effect of the reservoir from background charge carriers can be observed in this experiment, so the exact lifetime of the reservoir cannot be determined.

For this reason, the lifetime of a reservoir of non-resonantly pumped charge carriers is systematically examined in Chapter 6. The polariton fluid is first brought into a bistable state, which is then perturbed by the injection of a non-resonantly pumped reservoir. Observing the modified transmission through the sample in the presence of the reservoir, allows us to estimate the lifetime of the most long-lived of the particles that form the reservoir to more than 20 ns. By considering additional assumptions and further experiments, the range of possible candidates for the origin of this long-lived reservoir component can be limited to spin forbidden low momentum dark excitons close to $k_{\parallel} = 0$. This opens up the possibility to create optically generated very long-lived potential landscapes, whose components remain stationary as a consequence of their very low momentum states.

Appendix A

List of Abbrevations

BEC	Bose-Einstein condensate
BRF	birefringent filter
CCD	charge-coupled device
CMOS	complementary metal–oxide–semiconductor
CW	continuous wave
DBR	distributed Bragg reflector
DCP	degree of circular polarization
EOM	electro-optical modulator
fs	femtosecond
FWHM	full width at half maximum
GTI	Gires-Tournois interferometer
IO	input-output
LASER	light amplification by stimulated emission of radiation
LCOS	liquid crystal on silicon
LP	lower polariton
LP-LP	lower polariton-lower polariton (scattering)
LP-Ph	lower polariton-phonon (scattering)
LPB	lower polariton branch
LT	longitudinal-transversal

MCP	micro channel plate
NA	numerical aperture
OSHE	optical spin Hall effect
PD	photodiode
PL	photoluminescence
ps	picosecond
Q-factor	quality factor
QW	quantum well
SHE	spin Hall effect
SLM	spatial light modulator
TE	transversal electric
THR	threshold
Ti:Sa	titanium sapphire
TM	transversal magnetic
UP	upper polariton

Bibliography

[1] S. A. Cook in Proceedings of the third annual ACM symposium on Theory of computing - STOC '71, the third annual ACM symposium, ACM Press, Shaker Heights, Ohio, United States, **1971**, pp. 151–158.

[2] S. Kirkpatrick, C. D. Gelatt, M. P. Vecchi, *Science* **1983**, *220*, 671–680.

[3] R. J. Baxter, *Exactly solved models in statistical mechanics*, Academic Press, London ; New York, **1982**, 486 pp.

[4] A. Lucas, *Frontiers in Physics* **2014**, *2*, DOI 10.3389/fphy.2014.00005.

[5] F. Barahona, *Journal of Physics A: Mathematical and General* **1982**, *15*, 3241–3253.

[6] I. Bloch, J. Dalibard, S. Nascimbène, *Nature Physics* **2012**, *8*, 267–276.

[7] T. Esslinger, *Annual Review of Condensed Matter Physics* **2010**, *1*, 129–152.

[8] M. Lewenstein, A. Sanpera, V. Ahufinger, B. Damski, A. Sen(De), U. Sen, *Advances in Physics* **2007**, *56*, 243–379.

[9] M. Saffman, T. G. Walker, K. Mølmer, *Reviews of Modern Physics* **2010**, *82*, 2313–2363.

[10] J. Simon, W. S. Bakr, R. Ma, M. E. Tai, P. M. Preiss, M. Greiner, *Nature* **2011**, *472*, 307–312.

[11] A. Córcoles, E. Magesan, S. J. Srinivasan, A. W. Cross, M. Steffen, J. M. Gambetta, J. M. Chow, *Nature Communications* **2015**, *6*, DOI 10.1038/ncomms7979.

[12] B. P. Lanyon, C. Hempel, D. Nigg, M. Muller, R. Gerritsma, F. Zahringer, P. Schindler, J. T. Barreiro, M. Rambach, G. Kirchmair, M. Hennrich, P. Zoller, R. Blatt, C. F. Roos, *Science* **2011**, *334*, 57–61.

[13] K. Kim, M.-S. Chang, S. Korenblit, R. Islam, E. E. Edwards, J. K. Freericks, G.-D. Lin, L.-M. Duan, C. Monroe, *Nature* **2010**, *465*, 590–593.

[14] A. Marandi, Z. Wang, K. Takata, R. L. Byer, Y. Yamamoto, *Nature Photonics* **2014**, *8*, 937–942.

[15] T. Inagaki, K. Inaba, R. Hamerly, K. Inoue, Y. Yamamoto, H. Takesue, *Nature Photonics* **2016**, *10*, 415–419.

[16] J. Kasprzak, M. Richard, S. Kundermann, A. Baas, P. Jeambrun, J. M. J. Keeling, F. M. Marchetti, M. H. Szymańska, R. André, J. L. Staehli, V. Savona, P. B. Littlewood, B. Deveaud, L. S. Dang, *Nature* **2006**, *443*, 409–414.

[17] R. Balili, V. Hartwell, D. Snoke, L. Pfeiffer, K. West, *Science* **2007**, *316*, 1007–1010.

[18] J. J. Baumberg, A. V. Kavokin, S. Christopoulos, A. J. D. Grundy, R. Butté, G. Christmann, D. D. Solnyshkov, G. Malpuech, G. Baldassarri Höger von Högersthal, E. Feltin, J.-F. Carlin, N. Grandjean, *Physical Review Letters* **2008**, *101*, DOI 10.1103/PhysRevLett.101.136409.

[19] H. Deng, G. Weihs, C. Santori, J. Bloch, Y. Yamamoto, *Science* **2002**, *298*, 199–202.

[20] G. Tosi, G. Christmann, N. G. Berloff, P. Tsotsis, T. Gao, Z. Hatzopoulos, P. G. Savvidis, J. J. Baumberg, *Nature Physics* **2012**, *8*, 190–194.

[21] N. G. Berloff, M. Silva, K. Kalinin, A. Askitopoulos, J. D. Töpfer, P. Cilibrizzi, W. Langbein, P. G. Lagoudakis, *Nature Materials* **2017**, *16*, 1120–1126.

[22] P. G. Lagoudakis, N. G. Berloff, *New Journal of Physics* **2017**, *19*, 125008.

[23] H. Ohadi, A. J. Ramsay, H. Sigurdsson, Y. del Valle-Inclan Redondo, S. I. Tsintzos, Z. Hatzopoulos, T. C. H. Liew, I. A. Shelykh, Y. G. Rubo, P. G. Savvidis, J. J. Baumberg, *Physical Review Letters* **2017**, *119*, DOI 10.1103/PhysRevLett.119.067401.

[24] M. Grundmann, *The Physics of Semiconductors*, Springer International Publishing, Cham, **2016**.

[25] A. Kavokin, J. J. Baumberg, G. Malpuech, F. P. Laussy, *Microcavities*, Oxford University Press, **2007**.

[26] I. Institute, Basic Parameters of Gallium Arsenide (GaAs), Basic Parameters of Gallium Arsenide (GaAs), http://www.ioffe.ru/SVA/NSM/Semicond/GaAs/basic.html.

[27] H. Deng, H. Haug, Y. Yamamoto, *Reviews of Modern Physics* **2010**, *82*, 1489–1537.

[28] V. Savona, L. Andreani, P. Schwendimann, A. Quattropani, *Solid State Communications* **1995**, *93*, 733–739.

[29] G. Panzarini, L. C. Andreani, A. Armitage, D. Baxter, M. S. Skolnick, V. N. Astratov, J. S. Roberts, A. V. Kavokin, M. R. Vladimirova, M. A. Kaliteevski, *Physical Review B* **1999**, *59*, 5082–5089.

[30] C. F. Klingshirn, *Semiconductor Optics*, Springer Berlin Heidelberg, Berlin, Heidelberg, **2012**.

[31] I. I. Rabi, *Physical Review* **1936**, *49*, 324–328.

[32] J. J. Hopfield, *Physical Review* **1958**, *112*, 1555–1567.

[33] V. Savona, F. Tassone, C. Piermarocchi, A. Quattropani, P. Schwendimann, *Physical Review B* **1996**, *53*, 13051–13062.

[34] T. Fließbach, *Statistische Physik: Lehrbuch zur Theoretischen Physik IV*, Springer Berlin Heidelberg, Berlin, Heidelberg, **2018**.

[35] S. Christopoulos, G. B. H. von Högersthal, A. J. D. Grundy, P. G. Lagoudakis, A. V. Kavokin, J. J. Baumberg, G. Christmann, R. Butté, E. Feltin, J.-F. Carlin, N. Grandjean, *Physical Review Letters* **2007**, *98*, DOI 10.1103/PhysRevLett.98.126405.

[36] D. G. Lidzey, D. D. C. Bradley, M. S. Skolnick, T. Virgili, S. Walker, D. M. Whittaker, *Nature* **1998**, *395*, 53–55.

[37] K. B. Davis, M. .-.-O. Mewes, M. R. Andrews, N. J. van Druten, D. S. Durfee, D. M. Kurn, W. Ketterle, *Physical Review Letters* **1995**, *75*, 3969–3973.

[38] A. Imamog¯lu, R. J. Ram, S. Pau, Y. Yamamoto, *Physical Review A* **1996**, *53*, 4250–4253.

[39] D. Bajoni, *Journal of Physics D: Applied Physics* **2012**, *45*, 409501.

[40] W. Nolting, *Grundkurs Theoretische Physik 6*, Springer Berlin Heidelberg, Berlin, Heidelberg, **2014**.

[41] M. Klein, T. E. Furtak, *Optik*, OCLC: 863805678, Springer Berlin Heidelberg, Berlin, Heidelberg, **1988**.

[42] M. Onoda, S. Murakami, N. Nagaosa, *Physical Review Letters* **2004**, *93*, DOI 10.1103/PhysRevLett.93.083901.

[43] A. Kavokin, G. Malpuech, M. Glazov, *Physical Review Letters* **2005**, *95*, DOI 10.1103/PhysRevLett.95.136601.

[44] C. Leyder, M. Romanelli, J. P. Karr, E. Giacobino, T. C. H. Liew, M. M. Glazov, A. V. Kavokin, G. Malpuech, A. Bramati, *Nature Physics* **2007**, *3*, 628–631.

[45] M. I. Dyakonov, V. I. Perel', *Physics Letters A* **1971**, *35A*.

[46] K. V. Kavokin, I. A. Shelykh, A. V. Kavokin, G. Malpuech, P. Bigenwald, *Physical Review Letters* **2004**, *92*, DOI 10.1103/PhysRevLett.92.017401.

[47] D. Schmidt, B. Berger, M. Bayer, C. Schneider, M. Kamp, S. Höfling, E. Sedov, A. Kavokin, M. Aßmann, *Physical Review B* **2017**, *96*, DOI 10.1103/PhysRevB.96.075309.

[48] D. Schmidt, B. Berger, M. Bayer, C. Schneider, S. Höfling, E. Sedov, A. Kavokin, M. Aßmann, *Physics of the Solid State* **2018**, *60*, 1606–1610.

[49] B. Berger, Master Thesis, TU Dortmund, **2016**.

[50] R. I. Dzhioev, H. M. Gibbs, E. L. Ivchenko, G. Khitrova, V. L. Korenev, M. N. Tkachuk, B. P. Zakharchenya, *Physical Review B* **1997**, *56*, 13405–13413.

[51] M. D. Martín, G. Aichmayr, L. Viña, R. André, *Physical Review Letters* **2002**, *89*, DOI 10.1103/PhysRevLett.89.077402.

[52] I. Shelykh, K. V. Kavokin, A. V. Kavokin, G. Malpuech, P. Bigenwald, H. Deng, G. Weihs, Y. Yamamoto, *Physical Review B* **2004**, *70*, DOI 10.1103/PhysRevB.70.035320.

[53] M. M. Glazov, L. E. Golub, *Physical Review B* **2008**, *77*, DOI 10.1103/PhysRevB.77.165341.

[54] F. Tassone, F. Bassani, L. C. Andreani, *Physical Review B* **1992**, *45*, 6023–6030.

[55] M. M. Glazov, I. A. Shelykh, G. Malpuech, F. Laussy, K. V. Kavokin, A. V. Kavokin, *physica status solidi (c)* **2007**, *4*, 638–640.

[56] A. Amo, T. C. H. Liew, C. Adrados, E. Giacobino, A. V. Kavokin, A. Bramati, *Physical Review B* **2009**, *80*, DOI 10.1103/PhysRevB.80.165325.

[57] I. Shelykh, G. Malpuech, K. V. Kavokin, A. V. Kavokin, P. Bigenwald, *Physical Review B* **2004**, *70*, DOI 10.1103/PhysRevB.70.115301.

[58] D. N. Krizhanovskii, D. Sanvitto, I. A. Shelykh, M. M. Glazov, G. Malpuech, D. D. Solnyshkov, A. Kavokin, S. Ceccarelli, M. S. Skolnick, J. S. Roberts, *Physical Review B* **2006**, *73*, DOI 10.1103/PhysRevB.73.073303.

[59] H. Flayac, D. D. Solnyshkov, G. Malpuech, *New Journal of Physics* **2012**, *14*, 085018.

[60] G. Nardin, T. K. Paraïso, R. Cerna, B. Pietka, Y. Léger, O. El Daif, F. Morier-Genoud, B. Deveaud-Plédran, *Applied Physics Letters* **2009**, *94*, 181103.

[61] P. Cilibrizzi, A. Askitopoulos, M. Silva, F. Bastiman, E. Clarke, J. M. Zajac, W. Langbein, P. G. Lagoudakis, *Applied Physics Letters* **2014**, *105*, 191118.

[62] A. M. Andrews, R. LeSar, M. A. Kerner, J. S. Speck, A. E. Romanov, A. L. Kolesnikova, M. Bobeth, W. Pompe, *Journal of Applied Physics* **2004**, *95*, 6032–6047.

[63] J. M. Zajac, E. Clarke, W. Langbein, *Applied Physics Letters* **2012**, *101*, 041114.

[64] M. Abbarchi, C. Diederichs, L. Largeau, V. Ardizzone, O. Mauguin, T. Lecomte, A. Lemaitre, J. Bloch, P. Roussignol, J. Tignon, *Physical Review B* **2012**, *85*, DOI 10.1103/PhysRevB.85.045316.

[65] W. Langbein, J. M. Hvam, *Physical Review Letters* **2002**, *88*, DOI 10.1103/PhysRevLett.88.047401.

[66] M. Gurioli, F. Bogani, D. S. Wiersma, P. Roussignol, G. Cassabois, G. Khitrova, H. Gibbs, *Physical Review B* **2001**, *64*, DOI 10.1103/PhysRevB.64.165309.

[67] A. Askitopoulos, H. Ohadi, A. V. Kavokin, Z. Hatzopoulos, P. G. Savvidis, P. G. Lagoudakis, *Physical Review B* **2013**, *88*, DOI 10.1103/PhysRevB.88.041308.

[68] O. L. Berman, Y. E. Lozovik, D. W. Snoke, *Physical Review B* **2008**, *77*, DOI 10.1103/PhysRevB.77.155317.

[69] T. Byrnes, N. Y. Kim, Y. Yamamoto, *Nature Physics* **2014**, *10*, 803–813.

[70] A. Amo, J. Lefrère, S. Pigeon, C. Adrados, C. Ciuti, I. Carusotto, R. Houdré, E. Giacobino, A. Bramati, *Nature Physics* **2009**, *5*, 805–810.

[71] P. Cristofolini, A. Dreismann, G. Christmann, G. Franchetti, N. G. Berloff, P. Tsotsis, Z. Hatzopoulos, P. G. Savvidis, J. J. Baumberg, *Physical Review Letters* **2013**, *110*, DOI 10.1103/PhysRevLett.110.186403.

[72] A. Amo, D. Sanvitto, F. P. Laussy, D. Ballarini, E. d. Valle, M. D. Martin, A. Lemaître, J. Bloch, D. N. Krizhanovskii, M. S. Skolnick, C. Tejedor, L. Viña, *Nature* **2009**, *457*, 291–295.

[73] G. Liu, D. W. Snoke, A. Daley, L. N. Pfeiffer, K. West, *Proceedings of the National Academy of Sciences* **2015**, *112*, 2676–2681.

[74] D. Schmidt, B. Berger, M. Kahlert, M. Bayer, C. Schneider, S. Höfling, E. S. Sedov, A. V. Kavokin, M. Aßmann, *Physical Review Letters* **2019**, *122*, DOI 10.1103/PhysRevLett.122.047403.

[75] P. G. Savvidis, J. J. Baumberg, R. M. Stevenson, M. S. Skolnick, D. M. Whittaker, J. S. Roberts, *Physical Review Letters* **2000**, *84*, 1547–1550.

[76] D. Sarkar, S. S. Gavrilov, M. Sich, J. H. Quilter, R. A. Bradley, N. A. Gippius, K. Guda, V. D. Kulakovskii, M. S. Skolnick, D. N. Krizhanovskii, *Physical Review Letters* **2010**, *105*, DOI 10.1103/PhysRevLett.105.216402.

[77] M. Vladimirova, S. Cronenberger, D. Scalbert, K. V. Kavokin, A. Miard, A. Lemaître, J. Bloch, D. Solnyshkov, G. Malpuech, A. V. Kavokin, *Physical Review B* **2010**, *82*, DOI 10.1103/PhysRevB.82.075301.

[78] A. Baas, J. P. Karr, H. Eleuch, E. Giacobino, *Physical Review A* **2004**, *69*, DOI 10.1103/PhysRevA.69.023809.

[79] H. Abbaspour, G. Sallen, S. Trebaol, F. Morier-Genoud, M. T. Portella-Oberli, B. Deveaud, *Physical Review B* **2015**, *92*, DOI 10.1103/PhysRevB.92.165303.

[80] M. Amthor, T. C. H. Liew, C. Metzger, S. Brodbeck, L. Worschech, M. Kamp, I. A. Shelykh, A. V. Kavokin, C. Schneider, S. Höfling, *Physical Review B* **2015**, *91*, DOI 10.1103/PhysRevB.91.081404.

[81] C. Ouellet-Plamondon, G. Sallen, F. Morier-Genoud, D. Y. Oberli, M. T. Portella-Oberli, B. Deveaud, *Physical Review B* **2017**, *95*, DOI 10.1103/PhysRevB.95.085302.

[82] M. Wouters, T. K. Paraïso, Y. Léger, R. Cerna, F. Morier-Genoud, M. T. Portella-Oberli, B. Deveaud-Plédran, *Physical Review B* **2013**, *87*, DOI 10.1103/PhysRevB.87.045303.

[83] J. Schmutzler, T. Kazimierczuk, Ö. Bayraktar, M. Aßmann, M. Bayer, S. Brodbeck, M. Kamp, C. Schneider, S. Höfling, *Physical Review B* **2014**, *89*, DOI 10.1103/PhysRevB.89.115119.

[84] R. Butté, G. Delalleau, A. I. Tartakovskii, M. S. Skolnick, V. N. Astratov, J. J. Baumberg, G. Malpuech, A. Di Carlo, A. V. Kavokin, J. S. Roberts, *Physical Review B* **2002**, *65*, DOI 10.1103/PhysRevB.65.205310.

[85] S. Hunsche, K. Leo, H. Kurz, K. Köhler, *Physical Review B* **1994**, *49*, 16565–16568.

[86] J. O. Tollerud, S. T. Cundiff, J. A. Davis, *Physical Review Letters* **2016**, *117*, DOI 10.1103/PhysRevLett.117.097401.

[87] M. Richard, R. Romestain, R. André, L. S. Dang, *Applied Physics Letters* **2005**, *86*, 071916.

[88] L. Viña, *Journal of Physics: Condensed Matter* **1999**, *11*, 5929–5952.

[89] M. I. D'yakonov, V. A. Marushchak, V. I. Perel', A. N. Titkov, *JETP* **1986**, *63*, 655.

[90] G. E. Pikus, G. L. Bir, *JETP* **1971**, *33*, 108.

[91] Y. Yafet in *Solid State Physics*, *Vol. 14*, Elsevier, **1963**, pp. 1–98.

[92] M. Z. Maialle, E. A. de Andrada e Silva, L. J. Sham, *Physical Review B* **1993**, *47*, 15776–15788.

[93] G. Leménager, F. Pisanello, J. Bloch, A. Kavokin, A. Amo, A. Lemaitre, E. Galopin, I. Sagnes, M. De Vittorio, E. Giacobino, A. Bramati, *Optics Letters* **2014**, *39*, 307.

[94] J. Schmutzler, M. Aßmann, T. Czerniuk, M. Kamp, C. Schneider, S. Höfling, M. Bayer, *Physical Review B* **2014**, *90*, DOI 10.1103/PhysRevB.90.075103.

[95] C. Gautham, M. Steger, D. Snoke, K. West, L. Pfeiffer, *Optica* **2017**, *4*, 118.